ON MODIFICATIONS OF FLUID INCLUSIONS IN QUARTZ

RE-EQUILIBRATION EXPERIMENTS AND THERMODYNAMICAL CALCULATIONS ON FLUIDS IN NATURAL QUARTZ

RONALD J. BAKKER

ON MODIFICATIONS OF FLUID INCLUSIONS IN QUARTZ

RE-EQUILIBRATION EXPERIMENTS AND THERMODYNAMICAL CALCULATIONS ON FLUIDS IN NATURAL QUARTZ

OVER VERANDERINGEN VAN VLOEISTOF INSLUITSELS IN KWARTS

REËKWILIBRATIE EXPERIMENTEN EN THERMODYNAMISCHE BEREKENINGEN AAN VLOEISTOFFEN IN NATUURLIJKE KWARTS

(Met een samenvatting in het nederlands)

PROEFSCHRIFT

TER VERKRIJGING VAN DE GRAAD VAN DOCTOR AAN DE RIJKSUNIVERSITEIT TE UTRECHT, OP GEZAG VAN DE RECTOR MAGNIFICUS PROF. DR. J.A. VAN GINKEL, INGEVOLGE HET BESLUIT VAN HET COLLEGE VAN DEKANEN IN HET OPENBAAR TE VERDEDIGEN OP MAANDAG 26 OKTOBER 1992 DES NAMIDDAGS TE 12.45 UUR.

DOOR

RONALD JACK BAKKER

GEBOREN OP 1 DECEMBER 1962 TE GRONINGEN

aan mevrouw W.ToeLaer (1911-1988)

.

VOORWOORD

Voor het kritisch doorlezen van gedeelten van dit proefschrift en voor hulp in verscheidene laboratoria zou ik de volgende personen willen bedanken :

Bob Bodnar, A.J. Boer, Luc Bol, J. Brenan, Bas den Brok, M.R. Drury,
J. Dubessy, Ad van der Eerden, Juriaan Gerretsen, L.S. Hollister,
E.L. Johnson, Fons van den Kerkhof, Cheryl Knight, Robert McDonnell,
S.N. Olsen, Colin Peach, J. Pieters, F. Postma, D. Robinson, E. Roedder,
Herman van Roermond, R.D. Schuiling, Tony Senior, Chris Spiers,
Bob Strookappe, J.L.R. Touret, Janos Urai, Rian Visser, B.W.D. Yardley, en
drie anonieme recensenten.

In het bijzonder bedank ik Ben Jansen, voor zijn onuitputtelijke energie ieder manuscript te bekleden met vele kritische opmerkingen.

Cees van den Ende bedank ik voor mijn opname in zijn Italië veldwerk begeleidings groep, waardoor het belang van veld-geologie mij is bij gebleven.

En, hoe kan ik nu eindigen zonder Pauline te bedanken ....

Pauline, ... bedankt!
(prafschroeft)
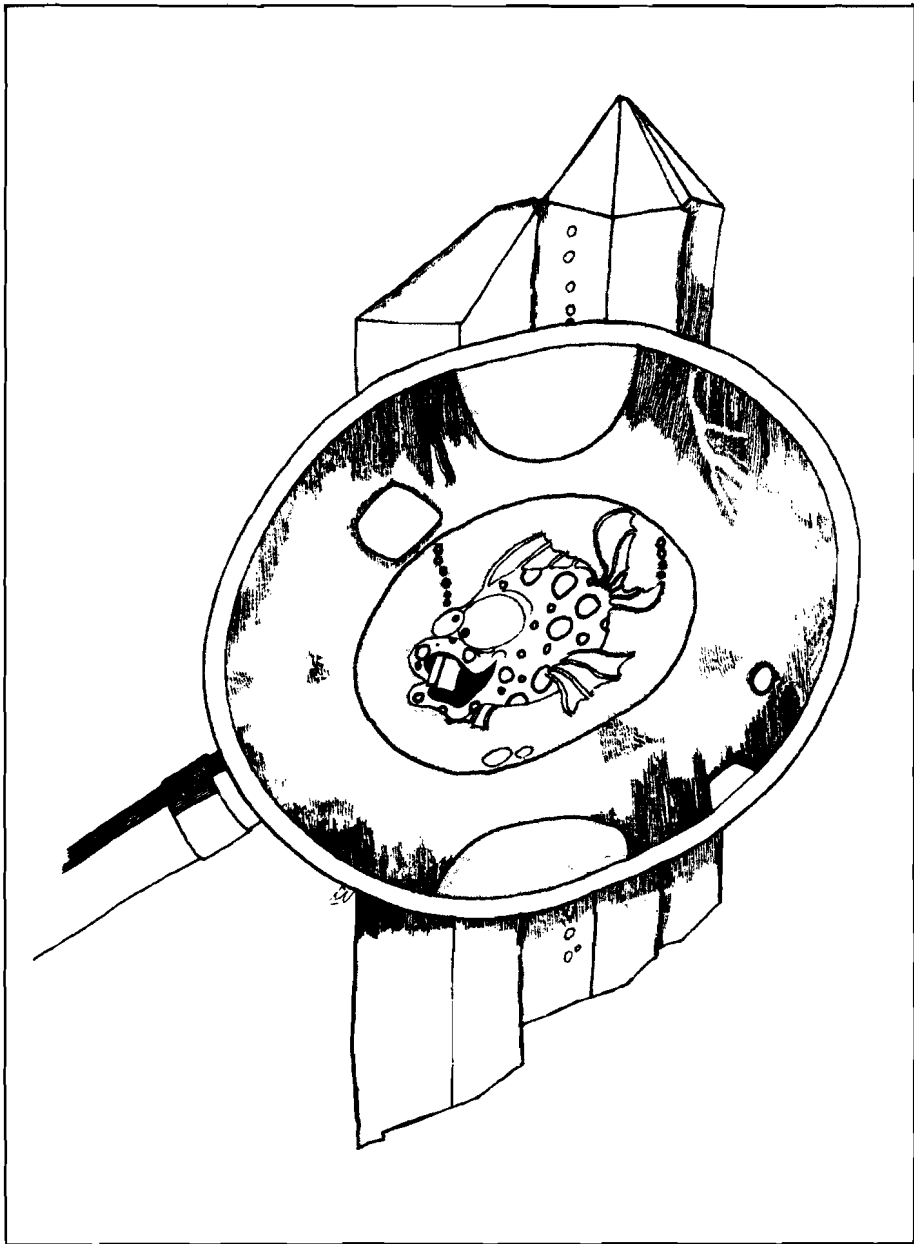
from ECROFI XI, Florence

CONTENTS

Chapter 4

A MECHANISM FOR PREFERENTIAL H_2O LEAKAGE FROM FLUID INCLUSIONS IN QUARTZ, BASED ON TEM OBSERVATIONS 61

Chapter 7

CONCLUDING REMARKS **165**

ABSTRACT

Fluids in rocks can be traced to great depths, and are found in crustal rocks as well as in mantle rocks. Information about the deep fluid which is obtained from fluid inclusions must be handled with care, for the way up after entrapment in a crystal is long and full of interferences at different pressures and temperatures. The fluid system may be a very complex mixture (H_2O, CO_2, CH_4, N_2, CO, NH_3, and H_2) with distinct physical and chemical proporties.

Chapter 1 indicates that many types of fluids have been recognized in rocks, and that each type may be related to a distinct grade of metamorphism (eg. Sorby 1858). For example, the type of fluid recognized in inclusions from very deep rocks, like granulites and upper mantle rocks is pure CO_2. Many interpretations of fluid inclusions are based on the assumption that fluid inclusions do not change in density and composition after entrapment. In recent years it was recognized that fluid densities may change during the long way up, and some voices were heard argueing compositional changes. In this study (Chapter 2 and Chapter 3) it is experimentally proven that CO_2-H_2O fluid inclusions, which are synthesized in Brazilian quartz at 835 K and 200 MPa, leak preferentially H_2O during re-equilibration at different conditions. The inclusions are submitted to an internal overpressure and underpressure. The remaining inclusions become relatively enriched in CO_2, and the H_2O must have diffused through the crystal, for there are no traces of cracks. Several underpressurized inclusions have "implosion halos" after re-equilibration, which consist of many small secondary inclusions.

Transmission electron microscopy (TEM) observations of the re-equilibrated Brazilian quartz and of quartz lenses from Naxos, Greece, (Chapter 4) indicate that dislocations adjacent to fluid inclusions account for the non-decrepitative preferential H_2O leakage. Ductile strain of the quartz neighbouring inclusions, which are overpressurized and underpressurized, is

1

expressed in the localized occurrence of many dislocations. Selective diffusion of H_2O along dislocations, which are assumed to be inaccessible for CO_2, results in the observed preferential H_2O leakage. Additionally, a solubility gradient of quartz in water between an underpressurized fluid inclusion and a dislocation cause the growth of small secondary bubbles at dislocations to optically visible "implosion halos" at the expense of the fluid inclusion.

The fluid which should occur at great depths can be indirectly obtained through thermodynamical calculations. The theoretical background of these calculations is described in **Chapter 5**. The well documented metamorphism from Rogaland (SW Norway) provides enough information to proceed these fluid calculations (**Chapter 6**). The calculated gaseous fluid inclusions are similar to the observed natural fluid inclusions. However, the calculated aqeous fluids are not recognized or registered by natural fluid inclusions. The absence of H_2O in low density metastable CO_2-CH_4-rich inclusions with graphite, and the occurrence of CH_4-N_2-rich inclusions are both proposed to result from preferential H_2O leakage.

The occurrence of CO_2 rich inclusions in granulites and mantle rocks may partly be caused by the fact that before exposure, these deep rocks have usually suffered more intensive recrystallization during uplift than shallow rocks. In future studies on fluid inclusions the effect of deformation on aqueous inclusions can not be ignored.

2

SAMENVATTING

Tot op grote diepte in de aardkorst en mantel komt een fluïde fase in gesteenten voor. Informatie over deze fase wordt verkregen uit insluitsels van deze vloeistof in mineralen. Echter, vanwege de extensieve opheffing en de vele mogelijke interacties met de omgeving, moet deze informatie kritisch worden verwerkt. Het fluïde systeem kan een complex mengsel zijn van H_2O, CO_2, CH_4, N_2, CO, NH_3 en H_2 met uitgesproken fysische en chemische eigenschappen.

In **Hoofdstuk 1** worden bekende typen fluïde fasen beschreven, die aan specifieke metamorfe omstandigheden gerelateerd kunnen worden (Sorby 1858). Bijvoorbeeld, in diepe gesteenten zoals granulieten en boven-mantel-gesteenten bestaat de fluïde fase uit pure CO_2. De huidige interpretatie van vloeistofinsluitsels is gebaseerd op de veronderstelling dat de dichtheid en samenstelling na insluiting niet veranderen. Echter, dichtheidsveranderingen zijn onlangs aangetoond en samenstellingsveranderingen worden ter discussie gesteld. In dit proefschrift (**Hoofdstuk 2** en **Hoofdstuk 3**) wordt experimenteel bewezen dat CO_2-H_2O vloeistofinsluitsels, die gemaakt zijn in Braziliaans kwarts bij 835 K en 200 MPa, preferent H_2O lekken tijdens reëkwilibratie onder andere omstandigheden. Het insluitsel wordt relatief verrijkt in CO_2. De H_2O moet door het kristal gediffundeerd zijn, daar er geen breukjes gevormd zijn. Vele onderdrukte insluitsels (dat zijn insluitsels met een interne druk die lager is dan de externe druk) hebben na reëkwilibratie "implosie-halo's", die bestaan uit vele kleine secundaire insluitsels.

Transmissie elektronen microskopische (TEM) waarnemingen van gereëkwilibreerd Braziliaans kwarts en van kwarts lenzen uit Naxos, Griekenland, (**Hoofdstuk 4**) laten zien dat dislocaties rondom vloeistofinsluitsels verantwoordelijk zijn voor de non-decrepitatieve preferente H_2O-lekkage. Ductiele vervorming van de kwarts naast insluitsels, die onderdrukt en overdrukt (dat zijn insluitsels met een interne druk die hoger is dan de externe druk) zijn, komt tot uiting in de vorming van vele dislocaties.

Selectieve diffusie van H_2O door dislocaties die niet toegankelijk zijn voor CO_2, resulteren in de waargenomen preferente H_2O-lekkage. De oplosbaarheidsgradiënt van kwarts in water tussen onderdrukte insluitsels en dislocaties doet kleine secundaire insluitsels ontstaan op dislocaties ten koste van de grotere onderdrukte insluitsels. Dit komt tot uitdrukking in de optisch zichtbare "implosie halo's".

De fluïde fase die op grote diepte voorkomt, kan thermodynamisch berekend worden. De theoretische achtergrond van deze berekeningen wordt beschreven in **Hoofdstuk 5**. De uitgebreid gedocumenteerde metamorfose van Rogaland (ZW Noorwegen) levert voldoende informatie om theoretische evolutie van de fluïde fase te berekenen (**Hoofdstuk 6**). De berekende gasrijke fasen komen overeen met waargenomen natuurlijke vloeistofinsluitsels. Echter, de berekende waterrijke fasen zijn niet geregistreerd door natuurlijke vloeistofinsluitsels. De afwezigheid van H_2O in metastabiele grafiet-CO_2-CH_4-rijke insluitsels met een lage dichtheid en het voorkomen van CH_4-N_2-rijke insluitsels zijn beiden het resultaat van preferente H_2O-lekkage.

Het voorkomen van CO_2-rijke insluitsels in granulieten en mantel gesteenten kan bijvoorbeeld gedeeltelijk verklaard worden door de intensievere rekristallisatie van deze gesteenten dan ondiepe gesteenten voordat de oppervlakte bereikt is. Het effect van deformatie op waterrijke insluitsels kan in verder onderzoek naar vloeistofinsluitsels niet verwaarloosd worden.

4

Chapter 1

INTRODUCTION

1.1 PREVIOUS STUDIES ON FLUID INCLUSIONS

Fluid inclusions in minerals are undoubtedly spotted a long time ago. Boyle (1672) mentioned several rarities in transparent crystals, which were large inclusions containing a liquid, visible with the bare eye. Motion of the liquid was easily observed when the crystal was made to change its posture. Boyle used this information to enforce his hypothesis that many gems either were once fluid bodies or in part made up of such substance as were once fluid. The role of water within the geology was emphasized by Werner (1749-1817) in his Neptunism theory, which suggests all crust materials to be initially in suspension or solution. Fluid inclusions were used as important arguments for this theory. At the end of the eighteenth century several scientists were able to distinguish different fluids in the cavities (e.g. Dolomieu, 1792, who describes petroleum). By this time, fluid inclusions were used against the Neptunism theory, mainly on the composition of fluid inclusion. A systematic analysis of fluid inclusion started a few decades later (Breislak, 1818; Deuchar, 1822; Davy, 1822; Brewster, 1823; Nicol, 1828).

The appearance of fluid inclusions in minerals raises many questions. What is in there, and what is the geological significance of their content? How and when are they formed? Can they change in shape, density and composition?

Many manuscripts have been published answering the first question, which were summarized by Smith (1953) and Roedder (1984). In the scope of this study, I wish to concentrate upon occurrence of nitrogen in fluid inclusions, which has been detected from the beginning of fluid inclusion analysis (Davy, 1822). Sorby (1858) was the first to describe a relation

between metamorphism and filling of fluid inclusions in quartz in schist samples approaching granite stocks in Cornwall. Strictly, the fluid in inclusions gives information about the fluid surrounding the crystal during entrapment. Data obtained from fluid inclusions and their applications were well summarized by Roedder (1984).

Misfits between growing sheets on a crystal face occurs, as a result of multiple nucleation on this face, which gives possibilities of fluid-entrapment. Sorby (1858) was the first to synthesize fluid inclusions in soluble salt, trapping a fluid during crystal growth on the faces. From the beginning of microscopic study of mineral inclusions (Nicol, 1828; Sorby, 1858; Van Hise, 1890) it has been recognized that cracks in crystals may heal by later crystallization, trapping some of the fluid which entered the opening. Lämmlein (1929) was the first to heal cracks artificially in saltpetre, halite and alum, producing planes of secondary type inclusions. The cracks were formed by cleaving the crystal partially with a razor blade. Lemmlein (1956) postulated that the mechanism of crack healing is based on capillary condensation and the tendency of the phase boundary to assume the form possessing the least free surface energy.

The subject was separated in two areas of research, involving the shape, density and composition of secondary fluid inclusions in healed cracks, and a study of the rate of crack-healing. Shelton & Orville (1980) cracked inclusion-free natural quartz by compression (Martin, 1972) and synthesized fluid inclusions at 873 K and 200 MPa water pressure. They concluded that the variation in fluid inclusion size and distribution can be directly related to former fracture-surface features. The density of supercritical water under experimental conditions was found to be in agreement with that inferred from homogenization temperature (the temperature at which liquid and vapor in an inclusion homogenize to one phase). Sterner & Bodnar (1984) evolved the applications of synthetic fluid inclusions to experimental geochemistry. They used a method described by Boyle (1672) to crack inclusion-free natural quartz, through heating the crystal and rapidly quenching it in cold water. Smith & Evans (1984) and Hickman & Evans (1987) concluded that the extent of healing was a function of time, temperature, the initial concentration of silica in the pore fluid, and

6

the initial crack dimension. Estimation of the rate of crack healing suggests that microcracks in quartz will have geologically short lifetimes at temperatures above 473 K (Smith & Evans, 1984).

Alterations of the shape, density and composition of fluid inclusions may occur through several mechanisms.

Lämmlein (1929) noticed the tendency of irregular shaped inclusions to recrystallize to negative crystals at constant room temperature, minimizing the amount of surface energy. Lemmlein (1956) performed the first experiments of crack healing in sodium nitrate under changing conditions (falling temperature), mimicking natural processes. He observed necking down of inclusions below the homogenization temperature, resulting in fluid inclusions with different densities. Within metallurgy and electrical material science, Nicols & Mullins (1965) explained sintering of spheres by capillarily induced surface diffusion, which was also thought to cause necking down of fluid inclusions. They summarized possible diffusion routes for necking-down which were through the inclusion fluid, through the surface (interface fluid-host mineral), and through the host mineral. Gratier & Jenatton (1984) measured and modelled the rate of change of inclusion shape, which occurred in synthetic quartz and synthetic calcite. In general, the internal recrystallization through solution-deposition processes causes most fluid inclusions to have different shapes from those originally trapped, although the densities remain unchanged.

Brewster (1835, 1848 and 1861) concluded that the pressure exerted by the fluid inclusions strained the crystal when it was in a soft state at elevated temperature. Crystals which were optically isotropic (like diamond) seemed to be anisotropic around fluid inclusions. The high internal pressure caused stretching (plastic deformation) of the fluid inclusion, resulting in a larger inclusion volume. More than a century later, Larson et al. (1973), Bodnar & Bethke (1984) and Pécher (1984) noticed the change in homogenization temperature in fluorite, sphalerite and synthetic quartz, due to stretching of inclusions. The deformation mechanism associated with stretching was poorly understood and thought to be plastic flow related to movement of dislocations. Stretching of an internally overpressurized spherical fluid inclusion in olivine was investigated by Wannamakers & Evans

7

(1989). The dislocation microstructure around the inclusion suggested that creep mechanisms operate.

Explosive leakage of fluid inclusions (decrepitation) was described by Brewster (1823), who by accident was attracted to this phenomena during decoloring experiments of topaz. At that time, decrepitation was used to confirm the presence of water and salt in fluid inclusions. Partial decrepitation, resulting in irreversible inclusion volume increase, was described by Lemmlein (1956). Pressure developed during heating in fluid inclusions caused the formation of fractures around the inclusion. A portion of the fluid was squeezed in the fractures, which began to heal and form extremely small inclusions. An aureole of minute inclusions occurred around the original inclusion with a lower density. The decrepitation clusters were also recognized in natural specimens by Swanenberg (1980) and experimentally by Gratier & Jenatton (1984).

Finally, fluid inclusions may change in density and composition by diffusion of material through the host mineral. The permeability of crystals to water was postulated and experimentally investigated by Deuchar (1822). Water passed through glass under high pressure, from observations after sinking stoppered bottles deep into the sea. Sorby (1858) stated that at very great pressure, water will not pass through solid crystal, expect by cracking it. Zirkel (1873) and Ward (1875) noted that the ratio of gas to liquid may vary greatly, even in neighbouring inclusions, which was ascribed to different degrees of leakage of fluid inclusions. Kennedy (1950) mentioned experiments of J. Grunig, who noticed diffusion of liquid into fluid inclusions in fluorite at 423 K, which were exposed to confining pressures higher than the internal fluid pressure. Stephenson (1952) concluded that fluid inclusions in sphalerite and calcite leak after the liquid phase fills the space available. Diffusion of water and water-related molecules through quartz became a major subject of research after the discovery of hydrolytic weakening of rocks (Griggs, 1967; Hobbs, 1968). The role of fluid inclusions during deformation experiments were investigated by Kerrich (1976), Wilkins & Barkas (1979) and McLaren et al. (1983). Kerrich (1976) noticed a relation between mineral texture and homogenization temperature. In vein quartz, undeformed quartz grains are more abundant and have fluid inclusions with

8

higher density than deformed grains. Wilkins & Barkas (1979) observed that the majority of small inclusions in quartz were associated with deformation band boundaries that have been introduced during ductile deformation. Fluid inclusions were suggested to resorb during recovery, introducing structural water in the quartz, which should promote dislocation propagation. McLaren et al. (1983) modelled the formation of bubbles in synthetic quartz using transmission electron microscopy (TEM). They proposed hydrogen to be incorporated by means if $(4H)_{Si}$ defects, which diffuse to form clusters, and they proposed bubbles to increase in size through pipe-diffusion of Si and O away from the bubble into linked dislocation loop. A similar phenomenon was already observed by Wolff (1845) after annealing experiments with natural quartz, in order to measure weight loss through decrepitation. Being unaware of possible growth of small bubbles in natural quartz, he observed a rose quartz to become milky-white after annealing. Ferguson (1914) noted that the milky white color of quartz is due to a great abundance of very small fluid inclusions. Gerretsen et al. (1989) suggest that all water in quartz is mainly in the form of molecular H_2O in inclusions. Such evidence associating water with dislocations structures leads to the conclusion that, in quartz, crystal plasticity enhances fluid mobility and points to fluid inclusions as an important source of chemically active fluids necessary for fluid assisted deformation (Spiers et al., 1990), and metamorphic processes (Carter et al., 1990).

1.2 AIMS AND INTENTIONS

The aim of this study is to investigate experimentally and theoretically the re-equilibration behaviour of synthetic fluid inclusions in natural quartz within the geological relevant C-O-H-N gas system, and to relate observed and reasoned phenomena with natural fluid inclusions in metamorphic rock.

Leakage of fluid inclusion in natural quartz and its mechanisms, which are related to deformation mechanisms, is experimentally studied in

CHAPTER 2 and CHAPTER 3. Synthetic CO_2-H_2O fluid inclusions in natural quartz are re-equilibrated under conditions different from the sythesis conditions. The inclusions are exposed to both internal underpressure (CHAPTER 2 and CHAPTER 3) and internal overpressure (CHAPTER 3). CHAPTER 4 includes TEM observations of quartz adjacent to both synthetic and natural fluid inclusions, in order to study possible routes for leakage. Theoretically, fluid calibrations in the C-O-H-N gas system are performed in CHAPTER 5 and CHAPTER 6. CHAPTER 5 includes the thermodynamical background of the calculations, which are executed with a computer program, written in Pascal. CHAPTER 6 presents the application of these calculations to metamorphic rock in Rogaland (SW Norway). Finally, CHAPTER 7 contains the main conclusions of this work.

1.3 EXPERIMENTAL METHOD

Several experiments are performed to synthesize fluid inclusions in natural quartz and to re-equilibrate these inclusions. The principles of the experimental method are described in this chapter. CHAPTER 2 and CHAPTER 3 describe in more detail the method for each individual experiment.

Gemstone quality natural quartz (Brazilian quartz) is used as host-mineral for synthetic fluid inclusions. The quartz is free of any primary or secondary inclusions. Orientated cores with 4 mm diameter are drilled out of single crystals. Micro-cracks are created in the cores (Fig.1.1) by sequentially heating the core to 673 K and quenching in cold distilled water. The cores are dried in a vacuum line at 383 K to remove all residual water in the cracks.

The source of the arbitrarily chosen fluid, which is meant to be included, are pure water and silver oxalate. The silver oxalate is made by a precipitation reaction (eq.1.1).

$$2AgNO_3 \ + \ H_2C_2O_4 \ \rightleftharpoons \ Ag_2C_2O_4 \ + \ 2HNO_3 \tag{1.1}$$
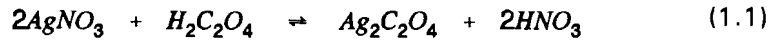
The silver oxalate is rinsed with destilled H_2O to remove the nitric acid, dried at 383 K in a vacuum line, and stored in a dry CO_2-environment. During experimentation, the silver oxalate decomposes at 413 K (eq.1.2), resulting in a pure CO_2 fluid and silver metal.

$$Ag_2C_2O_4 \ (s) \ \rightarrow \ 2Ag \ (s) \ + \ 2CO_2 \ (v) \tag{1.2}$$
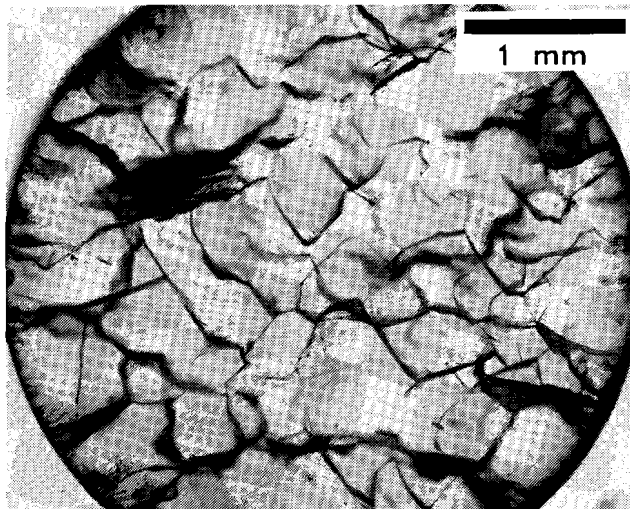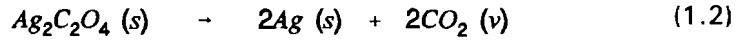
Figure 1.1
Quartz core (4 mm diameter) with various microcracks (dark parts).

A quartz core and a chosen amount of water and silver oxalate are put in a gold tube (5.8 mm and 9 mm diameter), which has been sealed at one end by arc welding. Subsequently, the gold tube is partly immersed in cold water, to prevent explosion of the silver oxalate and to prevent evaporation of the water during welding of the open side of the tube. After welding, the gold capsule is weighed and is then ready for experimentation at high temperature and pressure.

The fluid inclusion synthesis is preformed in an externally heated 7½ mm and 12½ mm diameter Tuttle-type pressure vessels (Edgar, 1973), with an argon pressure medium (Fig.1.2). The runs are first brought to the desired pressure at room temperature, the temperature is then increased, while the pressure is adjusted in several steps, until experimental conditions are reached. After the experiments the vessels are quenched to room temperature within 30 minutes with a compressed air flow, before the pressure is released.

After the experiment, the gold capsule is weighed again to check weightloss and immersed in hot water ($\pm$ 363 K) to check the welded edges for leaks, and to recognize possible diffusion through the gold. Capsules containing a mixture of H_2O and CO_2 are cooled to 255 K, punctured, and weighed again to measure the amount of released CO_2 gas. Subsequently, the capsule is dried in a furnace at 383 K, and weighed again to measure the amount of released H_2O. The quartz core with the partially healed cracks (Fig.1.3) are cut into 1 mm thick slices and polished on both sides.
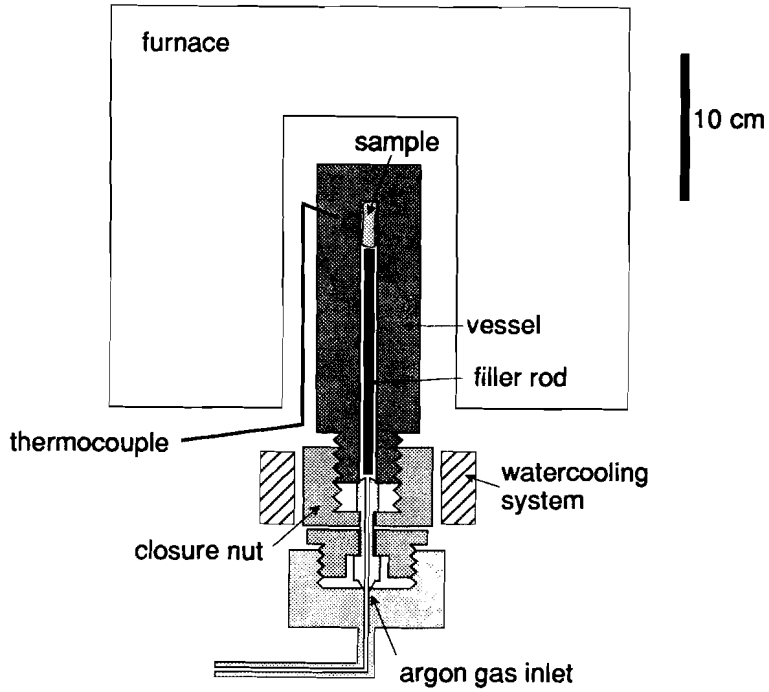
Figure 1.2
Tuttle-type pressure vessel. The hot spot of the furnace, which is shoved
over the vessel in vertical position, is at the place of the sample-capsule,
which is hold in position by a filler rod. The closure nut is cooled with
cold water during experimentation (watercooling system). The
temperature is measured with a thermocouple at the outside of the
vessel.
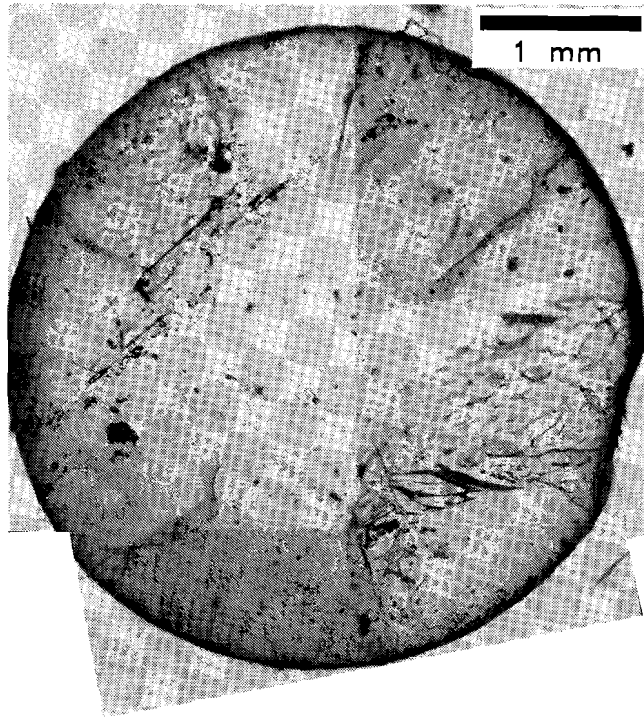
Figure 1.3
Quartz core after experimentation. Healed microcracks are marked with
numerous synthetic fi.s.

1.4 ANALYTICAL METHODS

A **Fluid Inc. adapted U.S.G.S.** gas flow heating-freezing stage with a **Doric 410A Trendicator** is used to measure melting and homogenization temperatures of the phases in fluid inclusions. The stage is calibrated with pure H_2O fluid inclusions (melting temperature H_2O at 273 K), mixed CO_2-H_2O fluid inclusions (melting temperature CO_2 at 216.6 K) and $NaNO_3$ crystals (melting temperature at 580 K).

The fluid inclusions are photographed with a **Leica CL camera** attached to a **Leitz SM LUX Pol. Microscope** to characterize their morphology and volume percentages of individual phases at room temperature. The best volume estimates are achieved in flat fluid inclusions.

Crystal defect structures in quartz with healed cracks are examined with **Transmission Electron Microscopy** (TEM). The specimen are prepared by ion bombardment from a 15 μm thin sections and examined in a **JEOL-200** electron microscope operating at 200 kV.

Surface morphologies of cracks, newly grown quartz in cracks, and fluid inclusion walls are photographed with **Scanning Electron Microscopy** (SEM). The specimens are subsequently coated with carbon and gold for examination with a **CAMPSCAN** electron microscope.

A **Microdil-28 Raman microspectometer (Dilor)** with a multichannel detector (Burke & Lustenhouwer, 1987) available at the Free University of Amsterdam, is used to check for presence of gas species other than CO_2 and H_2O.
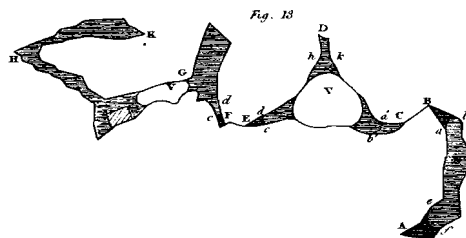
from Brewster (1823)

15

Chapter 2

PREFERENTIAL WATER LEAKAGE FROM FLUID INCLUSIONS BY MEANS OF MOBILE DISLOCATIONS

The fluid density, CO_2 content, and therefore the pressure-temperature conditions derived from fluid inclusions (fi.s) in metamorphic rocks are commonly inconsistent with coexisting mineral assemblages. Here we report hydrothermal experiments which mimic isobaric cooling, indicating changes in density and composition of H_2O-CO_2 inclusions in quartz without significant change in inclusion-volume. A simultaneous change to CO_2-rich compositions and lower densities indicates that water is leaking from the inclusions. We argue that preferential water leakage is made possible by microscopic unmixing of the H_2O-CO_2 mixture caused by physical and chemical interactions with the inclusion wall. Water transport then occurs by movement of water-saturated dislocations through the hydrothermally recrystallized quartz.

Significant discrepancies often exist both between the measured densities of gas-rich fluid inclusions and those calculated from the metamorphic pressure-temperature conditions as inferred from mineral assemblages, and between observed and calculated values of water content in fi.s for appropriate mineral stability fields, for example studies on Rogaland, SW Norway (Swanenberg, 1980; Jansen et al., 1985) and Naxos, Greece (Rye et al., 1976; Jansen & Schuiling, 1976; Kreulen, 1980; Jansen

et al., 1989). The discrepancies have led to suggestions concerning re-equilibration of fi.s, during post-peak deformation, for example by dynamic recrystallization (Kerrich, 1976; Wilkins & Barkas, 1979; Hollister, 1988). As such, re-equilibration during isobaric cooling for Rogaland (Jansen et al., 1985) or isothermal decompression by syn-metamorphic extension for Naxos (Urai et al., 1990) have been proposed.

Experimental re-equilibration of fi.s resulting only in density changes, has been achieved by (1) volume changes without significant diffusion of H_2O through quartz (Sterner & Bodnar, 1989); (2) decrepitation (Pécher, 1981; Gratier, 1982; Gratier & Jenaton, 1984; Pécher & Bouillier, 1984; Roedder, 1984); and (3) diffusion of H_2O through the quartz lattice (Gratier & Jenaton, 1984; Pécher & Bouillier, 1984) as point defects (interstitial molecules : Brunner et al., 1961; Hagon et al., 1987; and substitutes : Nutall & Weil, 1980; McLaren et al., 1983) or as water-related species through dislocation lines (Roedder, 1984; Blacic, 1975; Kekulawala et al., 1981; McLaren et al., 1989). Depending on temperature and crystallographic orientation with respect to deviatoric stress state, H_2O may diffuse through dislocation lines due to the activation of glide systems. Until now, no compositional change of H_2O-CO_2 rich fi.s has been experimentally studied by hydrothermal re-equilibration.

In this study, fi.s were synthesized at 200 MPa and 835 K for 38 days according to the method of Sterner & Bodnar (1984) in cores drilled out of optically clear Brazilian quartz. The fluid composition was 79 ± 3 mol% H_2O and 21 ± 3 mol% CO_2 with no addition of salt, hydroxide or acid in order to avoid rapid quartz recrystallization and incorporation of imperfections. Flat fi.s were selected from a three-dimensional inspection with a U-stage to characterize their morphology and volume percentages of the gas species (Fig.2.1A). A microthermometric study yielded an average homogenization temperature (T_H) of the CO_2 phases at 304.2 K and of the total H_2O-CO_2 content at 574.4 K (Table 2.1). Electron microscopy (TEM) was preformed identify defect structures in the healed crack. The thin foils were prepared from quartz cores from duplicate experiments in order to keep the core, intended for further re-equilibration, undamaged (see below).

18
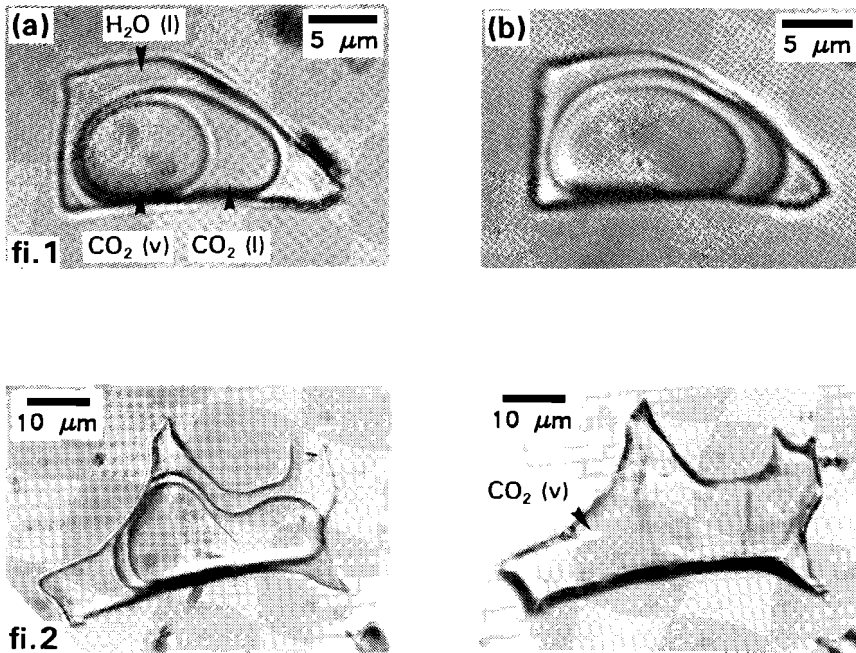
Figure 2.1

(A) Photomicrograph of three-phase fi.s generated in the original experiment, with 21 mol% CO_2. At 293 K, the volume percentages of $H_2O(l)$, $CO_2(l)$, and $CO_2(v)$ are 40, 39, and 21 respectively. Both inclusions homogenize at 304.3 K for the CO_2 phases and at 574.8 K for the CO_2-H_2O phases.

(B) Photomicrograph of the identical inclusions after the new experiment, simulating isobaric cooling. Only minor solution and precipitation is illustrated. At 293 K, the volume percentage of $H_2O(l)$, $CO_2(l)$, and $CO_2(v)$ have been changed to 31, 29, and 40 respectively for fluid inclusion 1 (fi.1) and to 10, 0, and 90 respectively for fluid inclusion 2 (fi.2). The $H_2O(l)$ phase of fi.2 is concentrated in the edges of the inclusion. The T_H of the CO_2 and the CO_2-H_2O phases for fi.1 have been changed to 303.6 K and 579.5 K, respectively, and for fi.2 to 269.8 K and 552.8 K. The calculated mol% CO_2 for fi.1 and fi.2 are 26 and 46, respectively.

19

	Duration (in days)	Homogenization CO_2 phases			Homogenization H_2O-CO_2 phases		
		T_{min}	T_{max}	T_{av}	T_{min}	T_{max}	T_{av}
Original experiment	38	303.5[#]	304.4[#]	304.2[#]	573.1	575.7	574.4
New experiment	21	266.0	304.1	-	541.0	595.4	-

Table 2.1
Duration of the experiment, range of T_H (in K) of CO_2 and CO_2-H_2O
mixtures of the original and new experiments. There were 57
measurements per experiment. # : Temperatures of fi.s that homogenize
to the liquid phase (others homogenize to the vapour phase). The original
fi.s yield a narrow range of both T_H, whereas the recrystallized fi.s in the
new experiment display a broad range.

Isobaric cooling was experimentally reproduced by a second anneal at 673 K
and 200 MPa for 21 days (Fig.2.2). A pure H_2O environment of the quartz
core was chosen to distinguish newly formed inclusions from the original
CO_2-bearing fi.s from the first run. The identical individual inclusions were
again photographed (Fig.2.1B) and T_H were remeasured (Table 2.1).
Comparison of morphologies of these flat inclusions assures that the volumes
changed less than 4 vol% and presumably, this may hold for all fluid
inclusions. The quartz was re-examined by TEM after microthermometry. The
foils were made of small, 0.5 mm thick slices of the same core used in both
synthesis and re-equilibration experiments. Direct comparison of the
dislocations before and after re-equilibration was impossible.

As a result of the second run, a few pure H_2O fi.s were synthesized
in cracks, which were not completely annealed after the first run. Their
average molar volume 0.0445 mol/cm^3 reflects the new conditions. The
identical CO_2-H_2O inclusions from the first run now contain lower densities
than after the first run as illustrated by volume increases of the vapour and
liquid CO_2 bubbles at the expense of H_2O volume (Fig.2.1A, B). The T_H of the

20

CO_2 phases is now in the range 266.0-304.1 K, whereas T_H of the total content is in the range 541.0-595.4 K (Table 2.1).
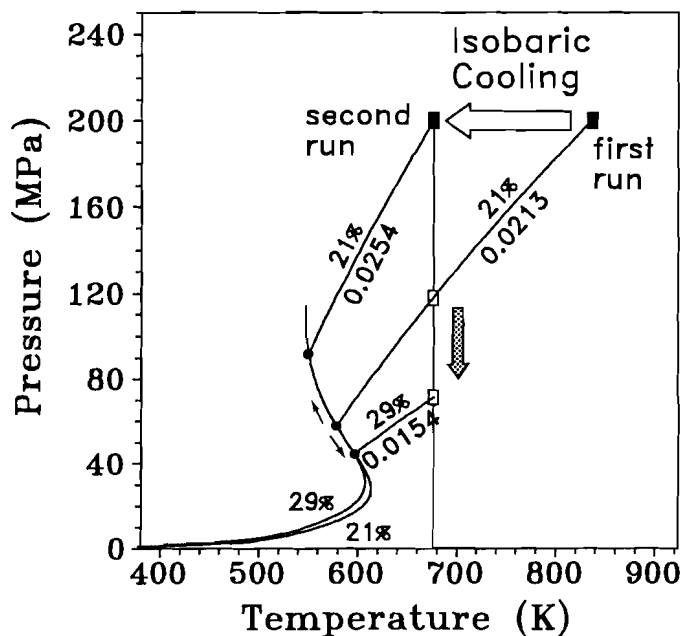
Figure 2.2

Pressure-Temperature diagram displays the experimental conditions (black squares). The curved lines are projections of the experimentally determined H_2O-CO_2 mixing areas (Takenouchi & Kennedy, 1964) for 21 and 29 mol% CO_2. The corresponding isochores and their densities (mol cm^{-3}) are calculated as nearly straight lines with the MRK equation of state (Christoforakis & Franck, 1986). Isobaric cooling is indicated with the large open arrow. The shaded arrow indicates the development of the underpressure in the fluid inclusions due to preferential leakage of H_2O at new experimental conditions (see text). The P_{INTERN} at the new conditions is indicated with open squares.

Water content was calculated by density measurements and volume estimations of the fluid species based on surface measurements. A few fi.s retained their original water content values, but most were lower than the

21

original values. Any inclusion-volume adjustments and infiltration of H_2O would result in lower T_H (Fig.2.2). Seemingly contradictory, preferential leakage of H_2O is responsible for instantaneously higher T_H and simultaneous internal pressure drop.

Fugacity-, chemical-, and pressure-gradients are considered as driving forces, resulting only in infiltration of H_2O. Water leaked out of the fi.s, so these gradients cannot be the direct driving force for outward H_2O diffusion and the diffusion cannot occur by channelized cracks or pores. The available data for point-defect diffusion in quartz (Kats, 1962; Dennis, 1984; Gilette & Yund, 1984; Kronenberg et al., 1986) prove that this mechanism is too slow to be effective within the time of experimentation. Dislocations in hydrothermal quartz were imaged with TEM (Fig.2.3). Most of the apparently isolated inclusions end in dislocation arrays (Burgers vector parallel to < a >) or larger channel-like imperfections. Dislocation arrays seem to be pinned on fi.s (Fig.2.3). The formation of bubbles on dislocation lines (Balderman, 1974; Paterson & Kekulawala, 1979; McLaren et al., 1983) after heat treatment and numerous secondary inclusions, implosion halos (Pécher, 1981; Pécher & Bouillier, 1984; Sterner & Bodnar, 1989) surrounding the central inclusion, which do not show signs of micro-cracking, argue for H_2O transport by dislocation lines or larger imperfections.

Over- and under-pressures of the fluid inclusions are proposed to constitute a driving force for the development of dislocations. mobile dislocations are activated by adeviatoric stress state around the fi.s due to the lattice discontinuity and their mobility may result in an episodic tapping of fi.s. The dislocations may become saturated with water from the fluid inclusions. The dislocation loops, which move from the interior of the crystal to the surface, can be considered as 'water buckets', able to operate in both internal over- and under-pressure conditions. Because of the high length/diameter ratio, the volume transported H_2O may be larger than the claimed volume decrease of fi.s by pore collapse. Also, fi.s are principally major imperfections and may act as sources of dislocation multiplication. The mechanism does not explain leakage of only H_2O from a single-phase CO_2-H_2O mixture in fi.s during experimentation

22
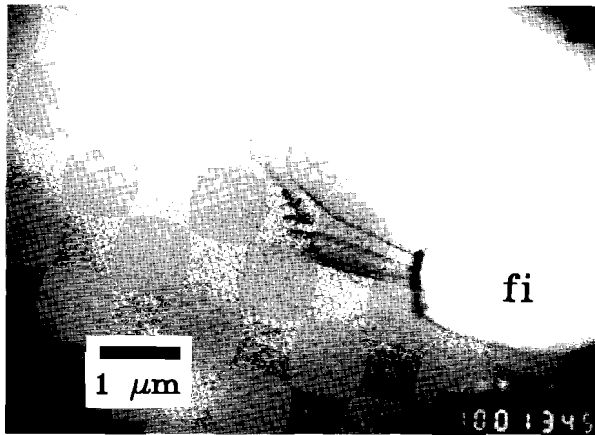
Figure 2.3
The bright-field elctron micrograph (TEM) of a synthetic fluid inclusion (white) produced in the original experiment illustrates a suite of six pinned dislocations.

Local unmixing on near-molecular scale must occur for the preferential leakage. this may be caused by the following:

(1) The physical and chemical interaction between hydrophile quartz and water dipoles. The surface of fi.s, the channel-like imperfections and the dislocation lines may be wetted by a molecular film of H_2O attached on interfacial silanol groups. On a larger scale, similar surface interactions, which may prevent CO_2 molecules from escaping through dislocations, have been proposed for fluid wetting of microcracks and grain boundaries in rocks (Watson & Brenan, 1987). Fluids with high CO_2 content ratios from isolated drops at grain corners, whereas at high H_2O contents a three-dimensional continuity of a fluid film exists.

(2) The restriction of the dislocation size (Hirth & Lothe, 1968; Yund et al.1981). The dislocations may be too small in diameter for effective molecular pipe-diffusion of CO_2 molecules, which are larger than H_2O molecules.

(3) The formation of H_2CO_3 molecules, by association of CO_2 and H_2O. These molecules influence the original fluid composition for small CO_2 contents. The dimensions of H_2CO_3 molecules are even larger than CO_2 molecules, enforcing argument (2).

23

We conclude that a wide range of inclusion compositions can be generated from one type of metamorphic fluid, by preferential H_2O leakage as a result of local variations in the degree of hydrothermal synmetamorphic recrystallization, even within a single trail. In experimental hydrothermal simulations of isobaric cooling (described here) and isothermal decompression (Bakker & Jansen, 1989) a decrease of density was caused by preferential leakage of water.

In theory, compositions of practically pure N_2-CH_4-CO_2 gaseous fi.s are thermodynamically forbidden at high-grade peak-metamorphic conditions (for Rogaland, Kerkhof, 1988). The argued H_2O leakage out of originally water-rich fi.s containing N_2, CH_4, and CO_2 may result in the observed extremely gas-rich fi.s. The density of CO_2-rich fi.s in metamorphic quartz lenses (for Naxos, Rye et al., 1976; Kreulen, 1980) are adjusted to post metamorphic conditions by preferential H_2O leakage and therefore, the CO_2 content is too high compared with the calculated CO_2 content derived from mineral equilibria.

Fig. 13.
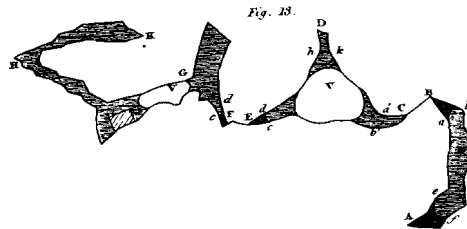
Chapter 3

EXPERIMENTAL POST-ENTRAPMENT WATER LOSS OF SYNTHETIC CO_2-H_2O INCLUSIONS IN NATURAL QUARTZ.

3.1 ABSTRACT

Artificial fluid inclusions were hydrothermally synthesized by crack healing in natural Brazilian quartz. Two original experiments E421 and E679 with a H_2O-CO_2 fluid were carried out at 835 K, 200 MPa over 38 days, and at 856 K, 211 MPa over 35 days, respectively. In both experiments homogeneous three phase (a vapour and two liquids) fluid inclusions of 22 and 20 mole% CO_2 respectively, were synthesized. The CO_2 phases homogenize to the vapour phase at 302.2 ± 0.1 K (E679, core 1 and 2), and to the liquid phase at 303.6 ± 0.3 K (E421, core 3), 303.9 ± 0.2 K (E421, core 4). The CO_2-H_2O phases homogenize to the vapour phase at 573.6 ± 0.4 K (E679, core 1 and 2), 575.6 ± 1.5 K (E421, core 3) and 576.1 ± 0.8 K (E421, core 4). Micro cracks and new hydrothermally precipitated quartz which directly surround the inclusions, were studied with TEM and SEM. The healed cracks have numerous growth imperfections that profided many possible routes for fluid transport. Dislocation arrays and small channels were observed and are often connected to the inclusions.

　　　Quartz core 3 and 4 were subsequently re-equilibrated 21 and 27 days respectively under hydrothermal conditions in pure H_2O at both a lower pressure of 100 MPa (E463), and a higher pressure of 365 MPa (E490) than

that of the original experiment E421. The temperatures of the re-equilibration experiments were equal to the original (835 K). In E463, the internal overpressured re-equilibration, only traces of solution and precipitation of quartz were evident with minor transformation of angular walls to more rounded formes. Volume increase for some inclusions resulted from decrepitation. The homogenization of the CO_2-H_2O phases to the vapour phase occurred at higher temperatures, up to 604 K. In E490, the internally underpressured re-equilibration, major solution and precipitation resulted in transformation to irregular shaped inclusion walls and formation of secondary inclusions halos. The homogenization of the CO_2-H_2O phases to the vapour phase at lower temperatures, down to 565 K. The fluids in inclusion from both re-equilibration experiments were found to have lower densities than the original fluids synthesised. This is quantified by the increased volumetric proportions of CO_2 vapor. The CO_2 fraction in inclusions was found to have increased, up to 54 mol%. The changing homogenization temperatures and the decrease in the proportions of H_2O in the original inclusions favours a model in which preferential transport of H_2O occurs along mobile dislocation lines, small intercrystalline nanocracks, or/and channels.

Results from experiment V1 and V4, using core 1 and 2, indicate that the changes observed in the re-equilibration experiments are not artifacts of the experimental method.

3.2 INTRODUCTION

Non-leakage behaviour of fluid inclusions (fi.s) may be expected if the post-metamorphic cooling path approximately follows the isochore of an enclosed fluid mixture. However, leakage may occur if pressure-gradients exist between the fi.s and the external pore fluid. Discrepancies exist between the density and composition of fluids observed from natural inclusions and theorical fluids calculated using metamorphic conditions deduced from geothermobarometry based on mineral equilibria.

Swanenberg (1980) questioned whether or not inclusions acted as closed systems in natural granulites from Rogaland, SW Norway, where an isobaric cooling succeeded the Proterozoic granulite facies metamorphism. Water leakage was assumed for amphibolite facies quartz lenses from Naxos, Greece (Jansen et al., 1989), where an isothermal decompression of about 300 MPa occurred as a result of rapid uplifts and associated deformation during Alpine metamorphism (Jansen et al., 1977; Andriessen, 1978; Buick & Holland, 1989).

The role of deformation on density- and compositional changes occurring in fi.s in quartz has been emphisized by Kerrich (1976), Wilkins & Barkas (1978), Urai et al. (1990) and Hollister (1989). Hollister (1988) has reviewed fi.s, found in greenschist-, amphibolite- and granulite-facies metamorphic rocks. He discusses fi.s which are assumed to have formed in the presence of a H_2O-rich phase and subsequently became CO_2-rich, due to preferential water leakage.

In the experimental work of Pécher (1981), Gratier (1982), Pécher & Bouillier (1984), Gratier & Jenaton (1984), Sterner & Bodnar (1989) and Boullier et al. (1989), models for density changes are presented. However, they do not consider compositional changes. Two mechanisms are recognized for density changes from internal over- and underpressure:

(1) volume changes by decrepitation of fi.s or plastic deformation of adjacent quartz;

(2) water-loss by diffusion of OH and by hydration of the adjacent rim of the host quartz, resulting in near-constant volume. Hall et al. (1989) reported compositional changes in synthetic H_2O-CO_2 fi.s, in which methane was formed after reduction of CO_2 by the inward diffusion of H_2. Compositional changes in synthetic H_2O-CO_2 inclusions, caused by the outward diffusion of H_2O, have been observed in both internal overpressure (Bakker & Jansen, 1989) and underpressure experiments (chapter 2, Bakker & Jansen, 1990).

In this paper we consider changes to both bulk density and composition of synthetic H_2O-CO_2 fi.s within natural Brazilian quartz during experiments simulating isothermal compression and isothermal decompression, in addition to isobaric cooling described by Bakker & Jansen

(1990, chapter 2). The morphology of the initial cracks as well as quartz growth in healed cracks were investigated with TEM and SEM techniques in order to discover routes of leakage.

3.3 EXPERIMENTAL METHOD

Six cylindrical cores (2mm length and 4 mm diameter) were drilled from an inclusion-free Brazilian quartz crystal, parallel to the c-axis. These were polished top and bottom. Cracks were created in these cores by rapid quenching in cold distilled water after heating to 623 K, according to the method of Sterner & Bodnar (1984). The cracks were dried as thoroughly as possible, in a vacuum line for 48 hours at 573 K. In experiment E679, quartz cores 1 and 2 were put in a gold tube, one end of which had been sealed by arc welding, with 31.0 mg silver-oxalate and 18.5 mg H_2O, yielding X_{CO_2} = 16.6 ± 0.1 mol%. In experiment E421, quartz cores 3,4,5 and 6 were put in another gold tube, also previously sealed at one end, with 26.8 mg silver-oxalate and 14.7 mg H_2O, yielding X_{CO_2} = 17.8 ± 0.2 mol%. Subsequently, the tops of the 30 mm long capsules were arc-welded. The fi.s synthesis was performed in 75 mm diameter Tuttle-type pressure vessels, with an argon pressure medium for experiments E421, E463, E490, E679 and with a water pressure medium for experiments V1 and V4. The original experiments E421 and E679 (Table 3.1 and Fig.3.1) were carried out at 200 MPa, 835 K and 211 MPa, 856 K respectively. The runs were first brought to the desired pressure at room temperature (Fig.3.1), the temperature was then increased, while the pressure was adjusted in several steps, until experimental conditions were reached. After the experiments the vessels were cooled to room temperature (293 K) within 30 minutes with an external air flow before the pressure was released.
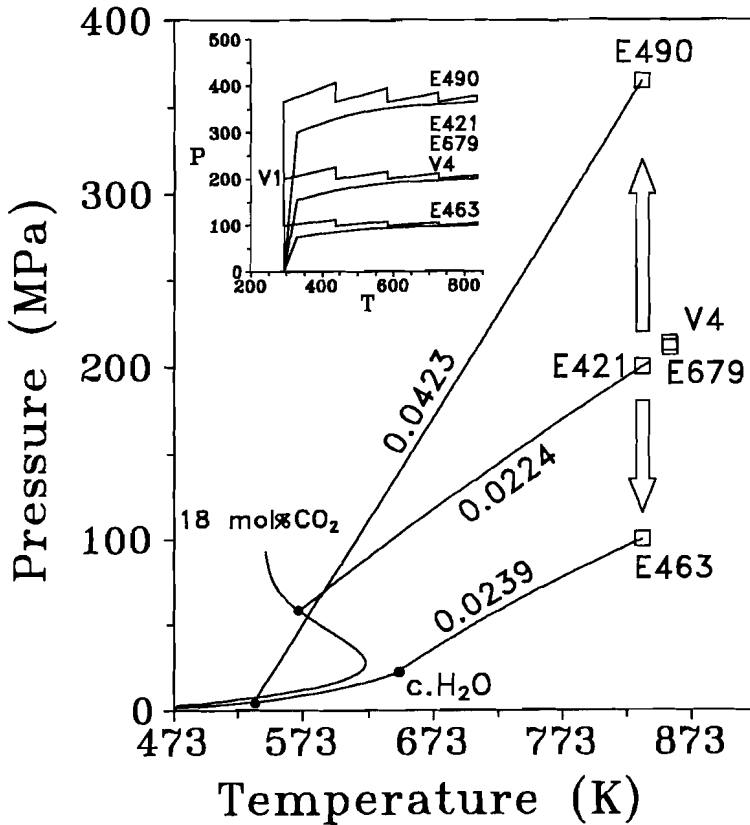
Figure 3.1

*P-T diagram for the fluids in the capsule surrounding the quartz core. The experimental conditions for E421, E679, E463, E490, and V4, and the corresponding isochores, calculated with the equation of state for CO_2-H_2O mixtures by Christoforakis & Franck (1986) and for pur H_2O by Kerrick & Jacobs (1981) are plotted. An 18 mol% CO_2 gas mixture isochore is indicated for E421 and E679. A pure H_2O fluid isochore is indicated for E463 and E490. The 18 mol% CO_2 miscibility gap and the boiling curve of pure H_2O are projected as curved lines. The critical point of H_2O is indicated by **c.H_2O**. The isothermal decompression and compression, which has a similar effect on fluid densities as isobaric cooling, are indicated with the large vertical arrows. The intersection of the isochores and the miscibility gap or the boiling curve predict the T_H of original fi.s in E421, E679, and of type 1 fi.s in E463, and E490. The schematic diagram in the upper left shows the starting and cooling PT-path followed by the experiments. The small arrows indicate the direction of the path.*

Experiment numbers		Quartz Core	Pressure (MPa)	Temperature (K)	mg of substances		Duration (days)
					silver-oxalate ($Ag_2C_2O_4$)	H_2O	
original experiments	E679	1, 2	211	856	31.0	18.5	35
	E421	3, 4, 5, 6	200	835	26.8	14.7	38
re-equilibration experiments	V1	1	196.5	293.2	-	40.0	0.083
	V4	2	213.5	855.8	-	60.0	23
	E463	3	100	835	-	10.0	27
	E490	4	365	835	-	10.0	21

Table 3.1

Experimental conditions, starting materials and duration of the original
and re-equilibration experiments.

A Fluid Inc. adapted USGS gas flow heating-freezing stage, calibrated using the fusion temperatures of pure H_2O, CO_2 and $NaNO_3$, was used to measure the homogenization temperatures (T_H) of the phases in the synthetic fi.s. Inclusions were optically photographed to characterize their morphology and volume percentages of the gas species (Table 3.2). Volume percentages were calculated by correcting the measured surface areas. The best volume estimates are achieved in flat inclusions. The mole fractions of the components (Table 3.2) were calculated by considering the density of each phase (H_2O liquid, CO_2 liquid and vapor) and their volume percentages. These were corrected using solubility data of CO_2 in H_2O (Dodds et al. 1956, Weast 1975). A Microdil-28 Raman microspectrometer with a multichannel detector (Burke & Lustenhouwer, 1987) was used to check for the presence of gas species other than CO_2 in selected fi.s from both the original and re-equilibration experiments.

The experimental technique was first tested, using core 1 and 2 from synthesis run E679. This was necessary to ensure that the observations from the re-equilibration experiments were not an artifact of the experimental technique. In re-equilibration experiment V1 (Table 3.1), core 1 was only pressurized to 196.5 MPa at room temperature for 2 hours. Experiment V4 (Table 3.1), using core 2, was run at 213.5 MPa and 856 K, approaching the original conditions.

			all fi.s		flat fi.s	
			range	average	range	average
Quartz core 3	vol%	$CO_2(v)$	11.2 - 19.5	17 ± 2	16.3 - 19.5	18 ± 1
		$CO_2(l)$	20.5 - 35.6	30 ± 5	29.7 - 35.6	33 ± 3
		$H_2O(l)$	44.9 - 68.3	53 ± 7	44.9 - 54.0	49 ± 4
	mol% CO_2		11.9 - 24.3	19 ± 3	18.7 - 24.3	22 ± 2
	T_H CO_2 phases (l)		303.2 - 304.1	303.6 ± 0.3		
	T_H CO_2-H_2O phases (v)		573.0 - 578.3	575.6 ± 1.5		
Quartz core 4	vol%	$CO_2(v)$	14.7 - 22.1	19 ± 2	16.9 - 19.7	18 ± 1
		$CO_2(l)$	23.8 - 35.8	32 ± 3	27.4 - 31.9	30 ± 2
		$H_2O(l)$	42.1 - 61.6	49 ± 5	48.4 - 55.7	52 ± 3
	mol% CO_2		16.2 - 25.8	21 ± 2	17.3 - 21.5	20 ± 2
	T_H CO_2 phases (l)		303.5 - 304.3	303.9 ± 0.2		
	T_H CO_2-H_2O phases (v)		574.2 - 577.6	576.1 ± 0.8		

Table 3.2

Ranges, averages and standard deviations of volume estimations and mol% calculations of all and flat fi.s in quartz cores 3 and 4 after the initial experiment E421, re-used for experiment E463 and E490. homogenization temperatures (in K) of CO_2, and CO_2-H_2O gas mixtures are indicated for all fi.s.

In the re-equilibration study, two experiments were performed (Table 3.1 and Fig.3.1) to simulate the effects of isothermal decompression (E463) at 100 MPa, 835 K and isothermal compression (E490) at 365 MPa, 835 K. Well-characterised cores 3 and 4 from synthesis experiment E421 were enclosed in capsules with 10 mg pure H_2O : (1) to prevent crushing or microcracking during further experimentation, due to the small non-hydrostatic pressure from the capsule walls on the cores; (2) to make a clear compositional distinction between the new (type 1 fi.s) and old generation (type 2 fi.s) inclusions. This amount of water is sufficient to maintain hydrostatic conditions in the capsules for the re-equilibration experiments, covering the total surface of the quartz cores, including any irregularities. The identical fi.s, photographed after the original experiment, were re-photographed and carefully investigated three-dimensionally using a U-stage. Their T_H values were also re-measured.

In core 5 from E421, defect structures of the quartz directly adjacent to the fi.s within the healed cracks were examined with TEM. The specimens were prepared by ion-bombardment from 15 μm thin sections and examined in a JEOL-200 electron microscope operating at 200 kV.

Before experiment E421, the surface morphologies of cracks in core 6, were investigated with SEM. After E421 newly grown quartz on cracks, and fi.s walls were photographed with SEM. The specimens were subsequently coated with carbon and gold for examination with a CAMPSCAN electron microscope.

3.4 RESULTS

3.4.1 Initial synthetic fluid inclusions from E421 and E679

Homogeneous generations of synthetic three-phase fi.s, containing CO_2-vapor, CO_2-liquid and H_2O-liquid, were created in the quartz cores of the synthesis experiments E421 and E679.

In E679, cores 1 and 2 homogenize to the vapour phase at the average temperature of 302.2 ± 0.1 K for vapour and liquid CO_2. The H_2O and CO_2 phases homogenize to the vapour phase at average temperature of 573.6 ± 0.4 K (Table 3.3).

In E421, vapour and liquid CO_2 homogenize to the liquid phase at the average value 303.6 ± 0.3 and 303.9 ± 0.2 K for core 3 and 4 respectively (Table 3.2 and Fig.3.2). The H_2O and CO_2 phases homogenize to the vapour phase at average temperatures of 575.6 ± 1.5 and 576.1 ± 0.8 K for core 3 and 4 respectively (Table 3.2 and Fig.3.3). The average mole-fractions CO_2 for all fi.s were calculated as 19 ± 3 % for core 3, later used for E463, and 21 ± 2 % for core 4, later used for E490 (Table 3.2).

	quartz core	T_H CO_2 phases (v)	T_H CO_2-H_2O phases (v)
E679	1, 2	302.2 ± 0.1	573.6 ± 0.4
V1	1	302.2 ± 0.1	573.3 ± 0.7
V4	2	302.0 ± 0.3	575.0 ± 0.8

Table 3.3

Averages and standard deviations of homogenization temperatures (in K) from CO_2 and CO_2-H_2O gas mixture of fi.s, before (E679) and after re-equilibration (V1 and V4).
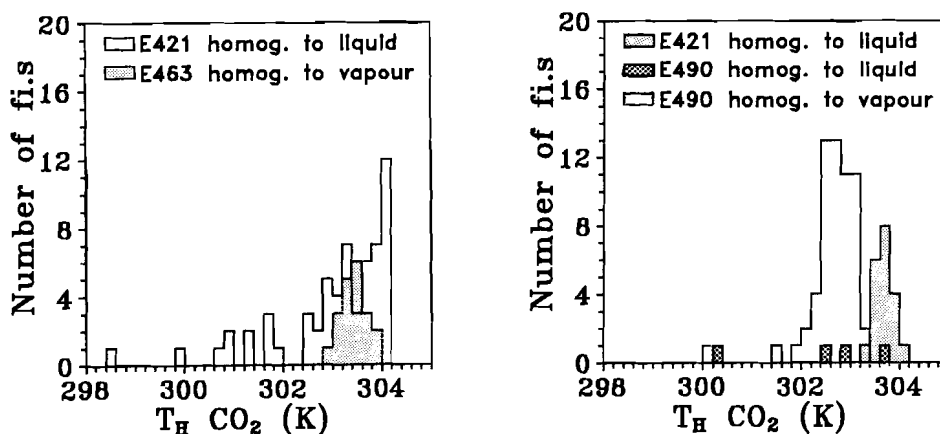
Figure 3.2

Histograms of CO_2 homogenization temperatures (T_H CO_2) of fi.s in quartz cores 3 and 4 used in the initial experiment E421 and the corresponding re-equilibration experiments E463 (A) and E490 (B). Only type 2 fi.s are considered (see text).

Figure 3.3

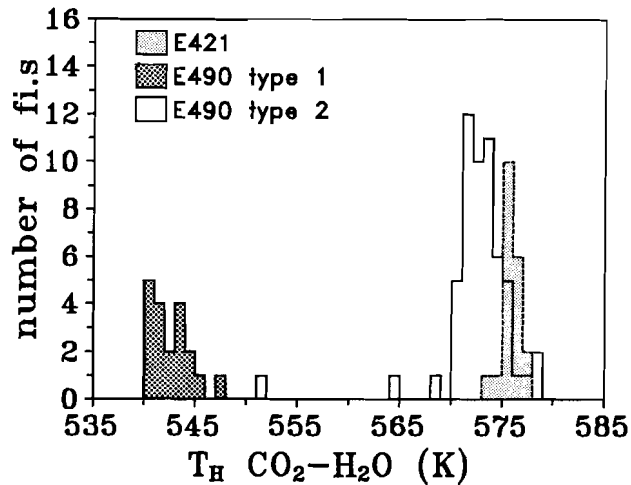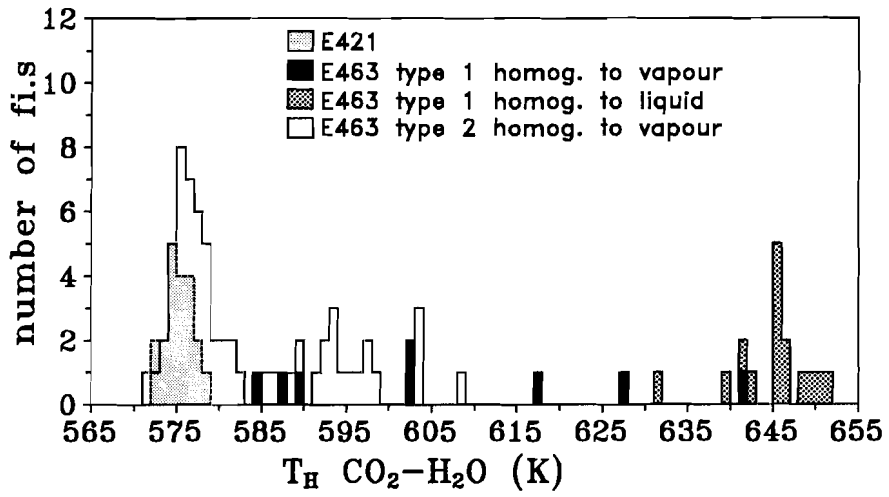*Histogram of CO_2-H_2O homogenization temperatures (T_H CO_2-H_2O) from fi.s in quartz cores 3 and 4 used in the initial experiment E421 and the corresponding re-equilibration experiments E463 (A) and E490 (B). All measured type 1 and type 2 fi.s are represented in the histograms.*

34

3.4.2 Transmission and scanning electron microscopy from E421

The newly grown quartz, directly adjacent to the synthetic fi.s in the healed crack of core 5 from E421, was examined with TEM. Most of the inclusions, which appear to be isolated by normal optical microscopy, end in long narrow channels with a maximum diameter of 0.1 μm (Fig.3.4). The channels are positioned oblique or parallel to the crack surface. Many growth imperfections exist along the healed crack (Fig.3.4), such as dislocation arrays and solid inclusions (presumably from silver oxalate). The dislocation arrays represent a stress field around the dislocation line with an established Burgers vector parallel to $<a>$. The dislocations may be connected to the inclusions as illustrated in Fig.2.3.

The initially introduced cracks in core 6 were investigated morphologically by the SEM before experimentation. Their shapes (Fig.3.5) vary from smooth curved planes without irregularities to planes with various steps, which are often arranged in feather-like patterns. After E421, observations were made of newly grown quartz in the cracks as shown in Fig.3.6A. The saw-tooth pattern on one side of the smooth curved crack represents the newly grown quartz. The orientation and regularity of the sides of the saw-tooth pattern indicate a crystallographically controlled overgrowth. Quartz overgrowth on a crack surface, oriented approximately parallel to the basal plane of quartz is illustrated in Fig.3.6B, revealing growth-hillocks consisting of flat regions between microsteps. Channels and inclusions are developed at irregularities on the surface of the quartz, at sites were no quartz growth has occurred. The channels are of the same order of magnitude as those determined by TEM (Fig.3.4), varying between 0.05 and 0.2 μm. The morphologies of the inclusion walls were examined. An opened inclusion of approximately 20 μm diameter is seen in Fig.3.7. Four pits (about 0.5 μm diameter) on the inclusion wall are shown at the bottom left, these are assumed to be openings of some channels.

Figure 3.4

36
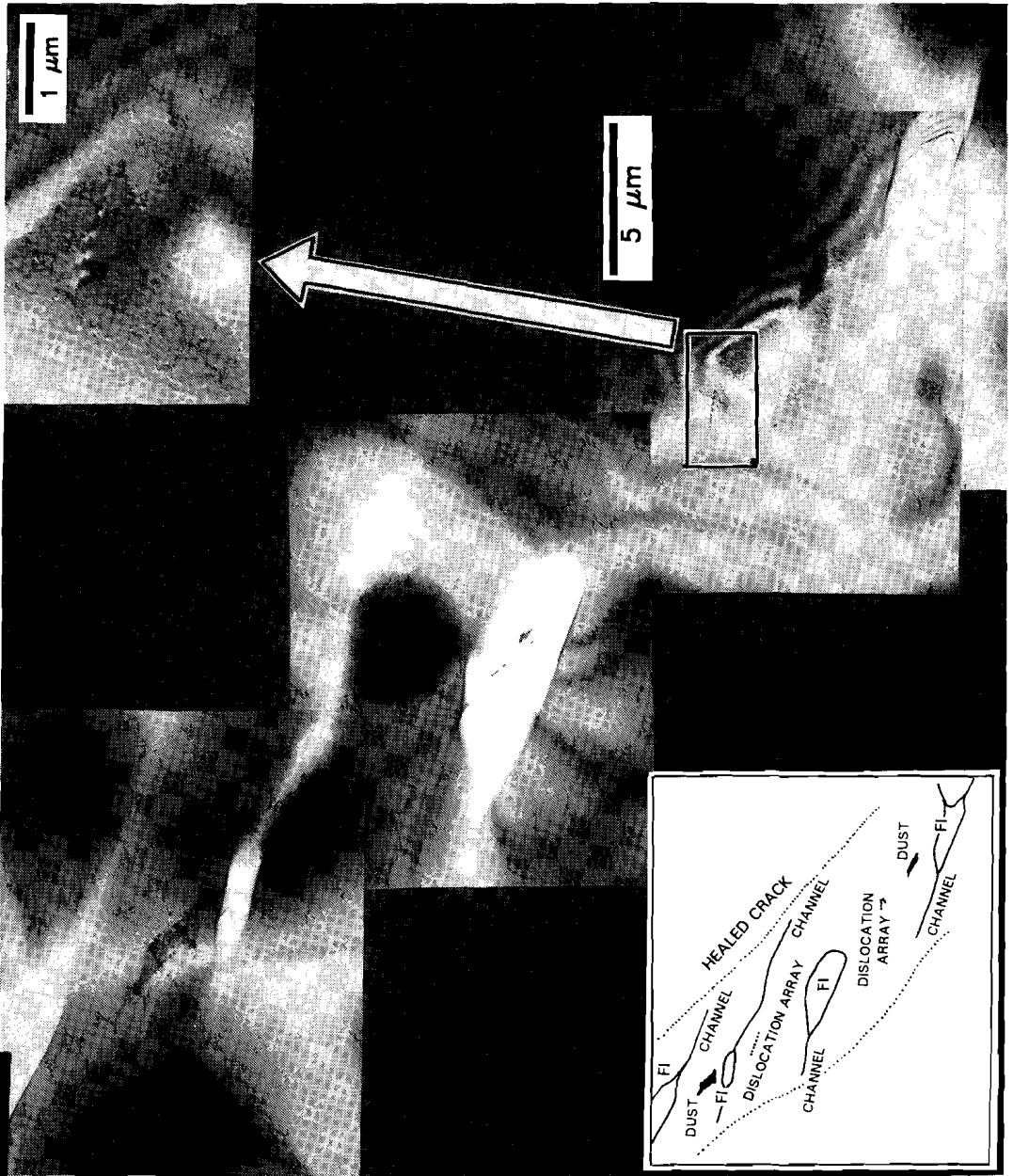
Figure 3.4
A composition of a series of bright field electron micrographs, revealing a healed microcrack of about 10 µm thickness in core 1 after E421. The synthetic fi.s (white spots) of around 1 to 2 µm radius, end in long (visible a maximum of 15 µm), narrow (about 0.1 µm diameter) channels (curved white lines). Between the fi.s incorporated particles and dislocation arrays (dark curved lines) are visible. The phenomena are sketched schematically, bottom-left side. The position of the healed crack is indicated by the stippled line. The white square is enlarged in the top-right corner, revealing dislocation arrays visible for more than 1 µm in length.
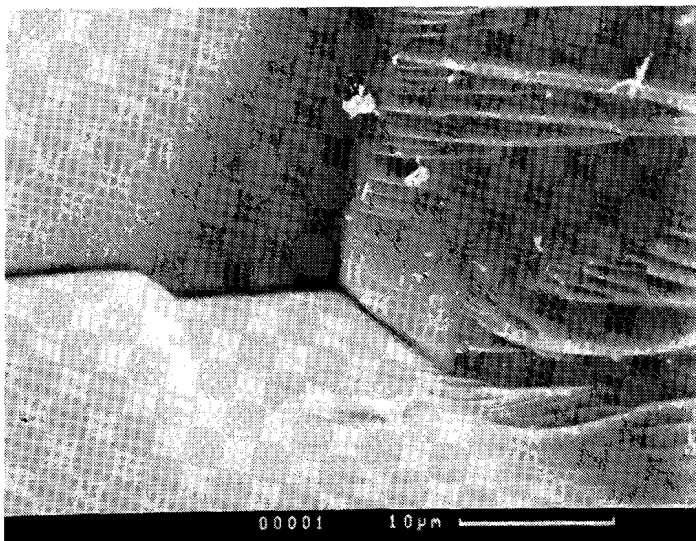
Figure 3.5
SEM photomicrograph of crack surfaces, created by quenching the quartz core 2 in water after heat treatment at 623 K before the original experiment E421. The morphology varies between smooth curved planes and a feather-like pattern of small steps.

37
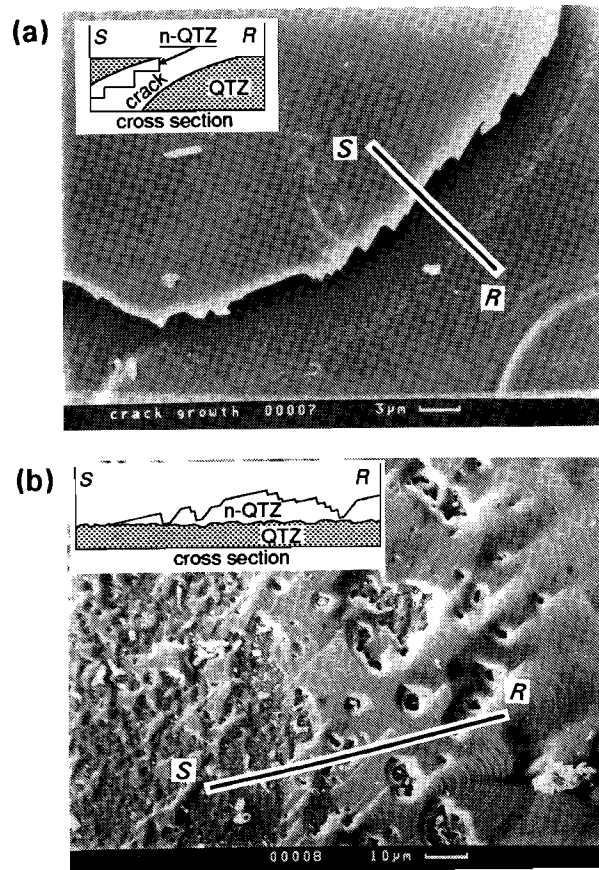
Figure 3.6

(A) SEM photomicrograph of crystal growth along a crack of about 2µm
thickness in core 2 after E421. The plane of projection is tilted 10
degrees from the basal plane, about a rotation axis approximately parallel
to the a-axis. Quartz overgrowth, only on the upper quartz surface below
the dashed line (marking the original crack surface), occurs in regular
patterns, defined by crystallographical orientations (see text).

(B) SEM photomicrograph of crystal growth on a crack surface in core 2,
showing growth-hillocks which are similarly defined by crystallographical
orientations, with flat regions between the macrosteps of about 1 µm.
Imperfections inherited from irregular growth, which is presumably
initiated on small quartz particles and or defects on the crack surface, are
the instigators for long, narrow channels, illustrated in Fig.3.4 (Qtz =
quartz, n-Qtz = newly grown quartz).
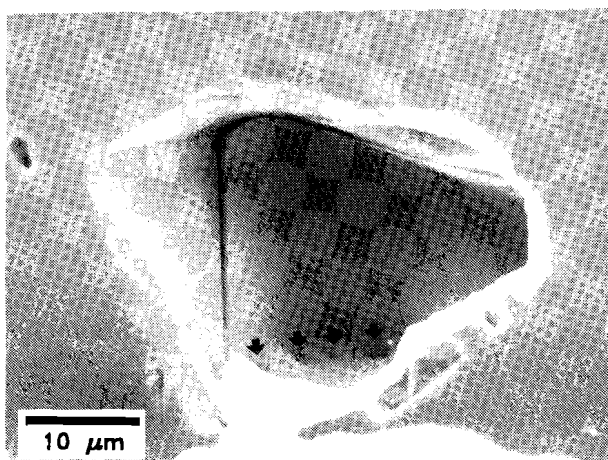
Figure 3.7
SEM photomicrograph of an opened inclusion (radius 10 μm) in core 2,
revealing a series of four small channels with radii of about 0.5 μm, on
the inclusion wall (arrows left down), as was visualized with TEM
(Fig.3.4).

3.4.3 Test experiments V1 and V4

Two extra runs were carried out to test the effectiveness of the experimental method. In both experiments (V1 and V4), no brittle failure in the quartz around the inclusions was observed after the runs. Only T_H was used as a measure of possible changes of density and compositions, as the errors in T_H measurements are smaller than those in volumetric determinations. The volumetric proportions of the phases did not change. For both experiments, no significant changes occurred in T_H (Table 3.3). This indicates that the observed changes in the re-equilibration experiments E463 and E490 did occur at the desired pressure and temperature.

3.4.4 Re-equilibration for isothermal decompression in E463

Quartz core 3 was pressurized at 100 MPa (Table 3.1). At 835 K, an overpressure of approximately 100 MPa was created in the original H_2O-CO_2 inclusions. Fig.3.3A gives all measured T_H. The T_H of the fi.s, illustrated in Fig.3.8, are listed in Table 3.4. Two distinctive types of inclusions were recognized in the core:

      1) **Type 1** fi.s start to form during renewed healing of cracks, which were only partly healed in initial experiment. Two-phase pure H_2O inclusions (Fig.3.8A) homogenize to the liquid phase at an average temperature of 646 K. The average volume percentage of the gas bubble is 55% of the total volume at 293 K. A minority of type 1 inclusions consist of water with variable low mole fractions CO_2, displaying two and three phase inclusions respectively. The H_2O and CO_2 phases homogenize to the liquid phase at high temperatures and to the gas phase at low temperatures between 584.8 and 651.4 K.

      2) **Type 2** fi.s are re-equilibrated original inclusions. This alteration is marked by major changes in composition and minor changes in inclusion shape. The solution and precipitation of the irregularly shaped inclusion walls may locally produce more rounded forms. The CO_2 phases homogenize to the vapour phase at temperatures ranging from 298.5 to 304.2 K (Fig.3.2A), which is evidently lower than for the initial inclusions of E421. The volume percentage CO_2 (liquid and vapour) values for examples given in Fig.3.8B, C, and D, correspond with Table 3.4. All measured values vary between 60 to 92, these present an increase with respect to those of E421. The H_2O and CO_2 phases homogenize to the vapour phase between 571.5 and 608.2 K (Fig.3.3A). At the edge of the quartz core, inclusions were observed containing only CO_2 with extremely low T_H (280 K, not represented in Fig.3.3A). The decrease in density of the CO_2, independent of the amount of decrease, corresponds to the increase in partial volume of CO_2, due to the loss of H_2O in the inclusions. Some inclusions show evidence of decrepitation (newly formed micro-cracks, Fig.3.8D), without loss of the included gas mixture. No CH_4 or CO was detected with Raman microscopy after the experiment.

40

Figure 3.8.

Photomicrograph of fluid inclusions before (E421) and after (E463) re-equilibration at 100 MPa and 835 K in core 3. The various phases, CO_2 (liquid and vapour) and H_2O (liquid and vapour) are indicated. (A) Type 1 fi.s containing pure H_2O which are representative of new hydrothermal conditions after E463. (B and C) Type 2 fi.s compared to original inclusions after E421, (D) Type 2 fi.s with newly grown microcracks (arrows) after E463.

41

(d)
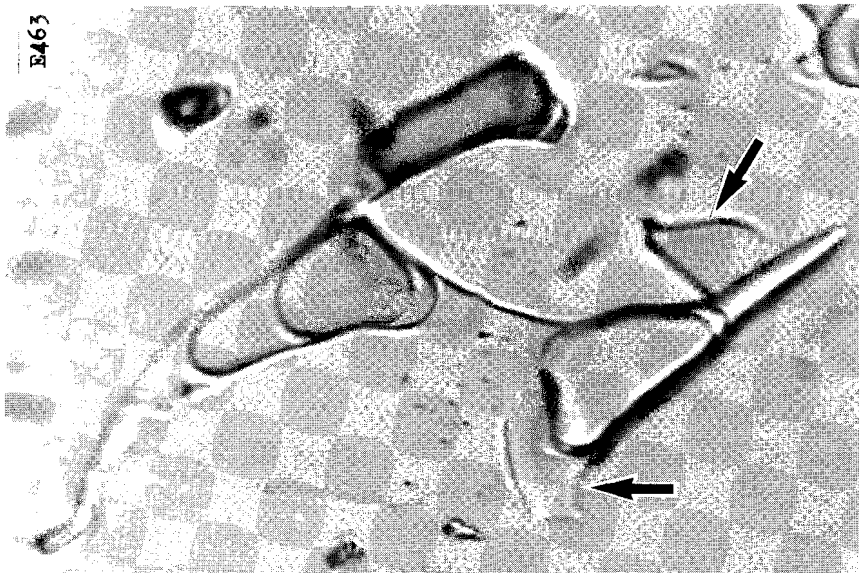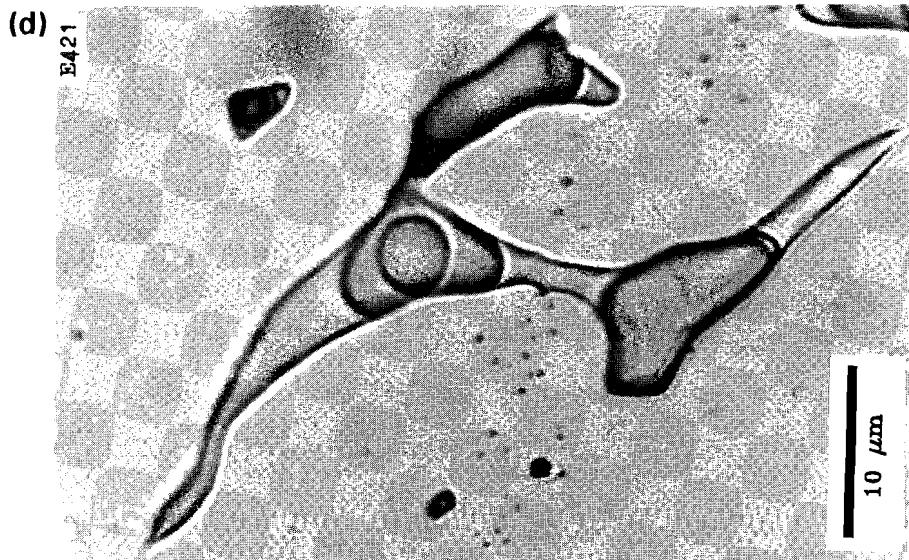
Figure 3.8. (Continued)

42

Fluid Inclusion			Volume Percentage				Mol% CO$_2$	Homogenization Temperature (K)		
Exp.	Fig.	Type	CO$_2$		H$_2$O			CO$_2$ (v)	CO$_2$-H$_2$O (v)	H$_2$O (l)
			vap.	liq.	vap.	liq.				
E463	3.8(A)	A: 1	-	-	49	51	-	-	-	650.0
		B: 1	-	-	52	48	-	-	-	650.3
		C: 1	-	-	55	45	-	-	-	650.8
	3.8(B)	2	48	24	.	28	33	304.0	591.8	-
	3.8(C)	2	56	24	-	20	38	303.5	579.4	-
	3.8(D)	2	48	22	.	30	28	304.1	593.5	-
E490	3.9(A)	1	-	-	23	77	-	-	-	546.2
	3.9(B)	2	50	18	-	32	23	302.5	571.1	-
	3.9(C)	2	58	20	-	22	26	301.8	572.8	-

Table 3.4

Optically estimated volumetric percentages of CO$_2$ and H$_2$O phases, mol% CO$_2$ and T$_H$ of CO$_2$, of CO$_2$-H$_2$O mixtures and of H$_2$O in few selected type 1 and 2 fi.s from the quartz cores after E463 and E490, corresponding to the illustrated re-equilibrated fi.s in photomicrographs in Fig.3.8 and Fig.3.9. Homogenization in liquid (l) or vapour (v) phase is indicated in the headings of the table.

3.4.5 Re-equilibration for isothermal compression in E490

The quartz core was repressurized to 365 MPa (Table 3.1). At 835 K an underpressure of about 165 MPa was created within the original fi.s. All measured T$_H$ are shown in Fig.3.3B. For example, the T$_H$ of inclusions in Fig.3.9 yields two values related to different types of fi.s (Table 3.4) :

1) **Type 1** fi.s (Fig.3.9A) are newly generated in E490. The average volume occupied by the vapour bubble is 24 % of the total volume at 293 K. The fi.s homogenize to the liquid phase at temperatures ranging from 540.7 to 548.0 K, with a frequency peak at 541 K (Fig.3.3B).

2) **Type 2** fi.s are re-equilibrated original fluid inclusions. No signs of decrepitation around the fi.s was observed. Solution and precipitation of quartz, which has occurred at the walls of the inclusions (Fig.3.9B and C),

was more pronounced than in E463. The vapour bubble volume increase is clearly illustrated in Fig.3.9B and C. The volume percentage CO_2 (liquid and vapour) in the re-equilibrated inclusions ranges from 38 to 80% of the total volume (some examples are given in Table 3.4). The CO_2 phases homogenize between 300.3 K to the liquid phase and 300.1 K to the vapour phase (Fig.3.2B). The CO_2 and H_2O phases homogenize to the vapour phase at temperatures ranging from 551.4 to 579.3 K, with a frequency peak at 572 K (Fig.3.3B). Again no CH_4 or CO was detected with Raman microscopy after the experiment.

(a)

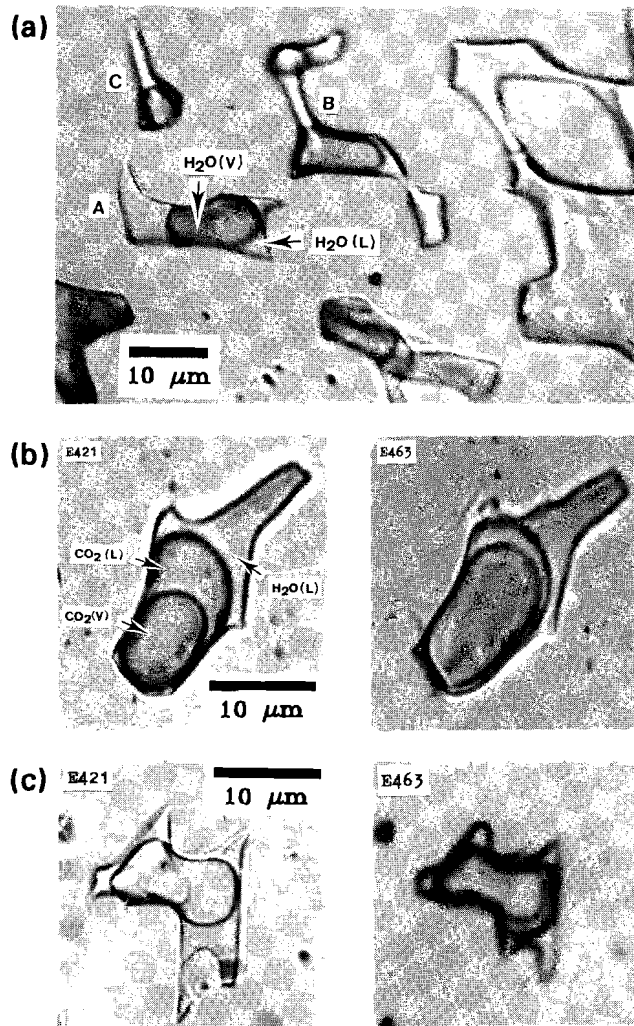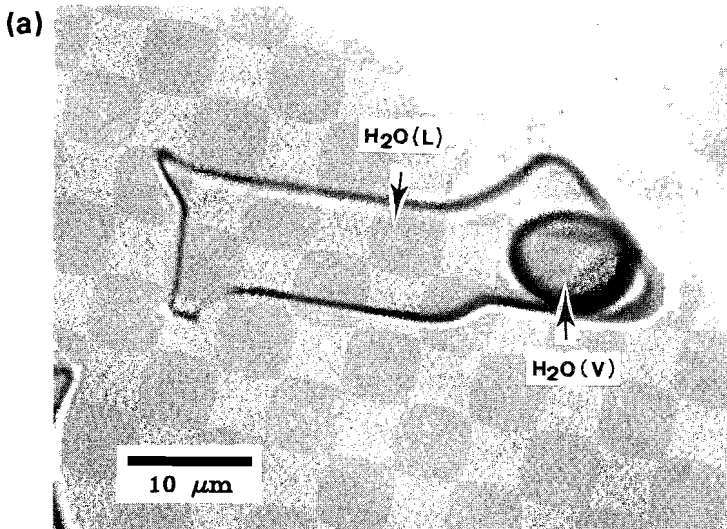*Figure 3.9.*
Photomicrograph of fluid inclusions before (E421) and after (E490) re-equilibration at 365 MPa and 835 K. The various phases, CO_2 (liquid and vapor) and H_2O (liquid and vapor) are indicated. (A) Type 1 fi.s containing pure H_2O which is representative of new hydrothermal conditions. (B and C) Type 2 fi.s compared to the original inclusions after E421. Solution and precipitation of quartz on the fi.s walls transformed the rim, creating irregularities.

(b)
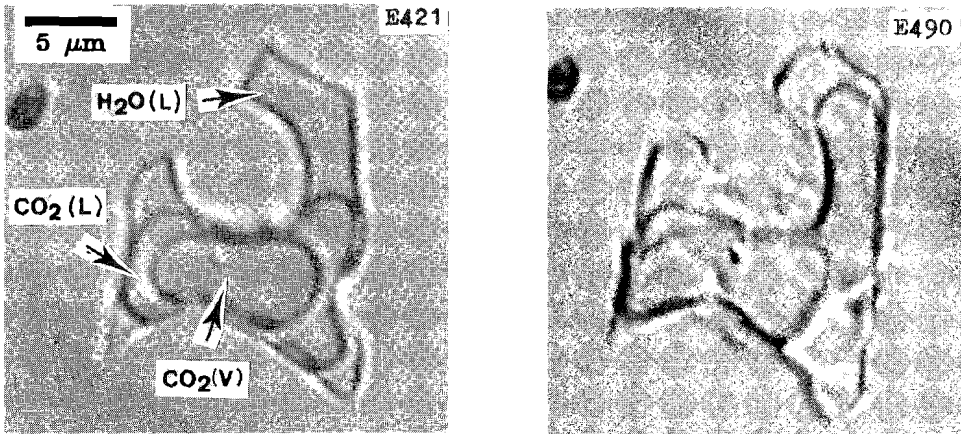
Figure 3.9. (Continued)

Summarizing, in both re-equilibration experiments the **type 2 fi.s** have reduced densities and increased mole fractions of CO_2. From these results we must assume H_2O-leakage. Any fluid leakage by decrepitation is reasonable for E463 as the fluid in the inclusions has an overpressure. However, the observed leakage of H_2O from E490 was unexpected, as it was presumed that the underpressure would lead to H_2O infiltration.

(c)
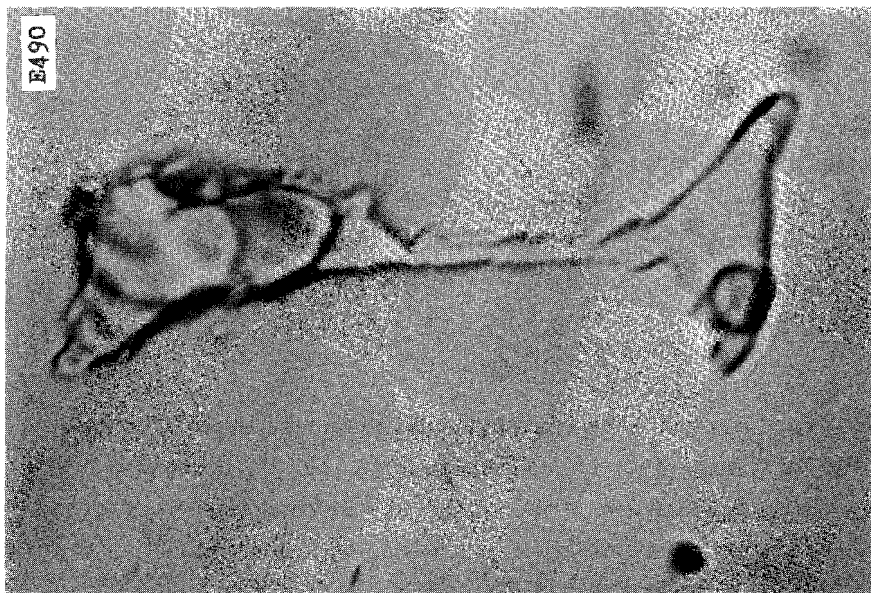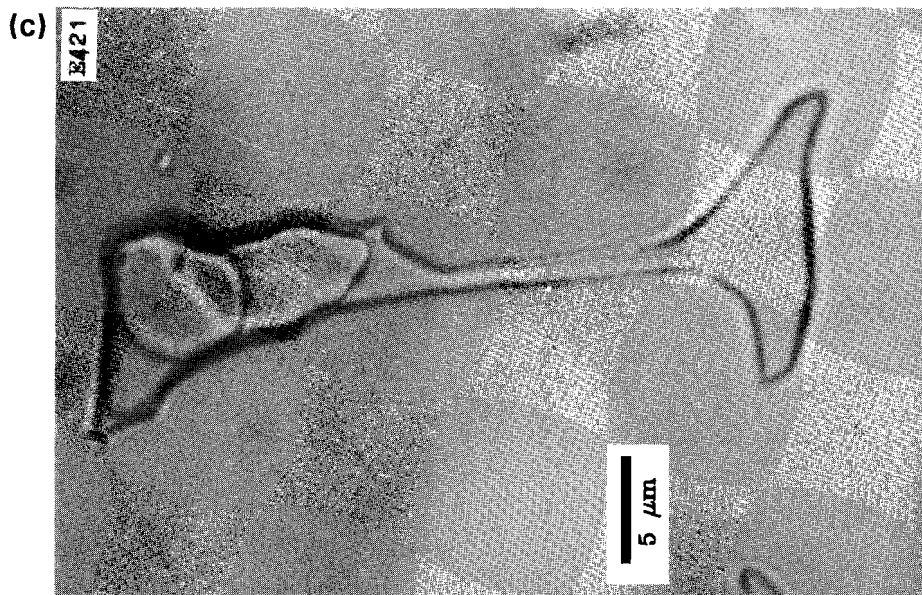
Figure 3.9. (Continued)

3.5 DISCUSSION

Sterner & Bodnar (1989) reported a density increase in fluid inclusions re-equilibrated at internal underpressure conditions, whereas Pecher (1981) described a density decrease. Bakker & Jansen (1990, chapter 2) observed an unexpected density decrease for experiments simulating isobaric cooling. Our new experiments argue for density decreases during re-equilibration with both internal under- and overpressure.

Using mechanisms for inclusion re-equilibration such as those suggested by Sterner & Bodnar (1989), we initially expected changes of volume without any significant leakage of H_2O or CO_2. We expected that the volume of individual inclusions in E463 and E490 should have been increased by 146% and reduced by 74% of the original volume, respectively. However, the microphotographs from both experiments (Fig.3.8 and 3.9) reveal only minor volume changes. The estimated X_{CO2} values (Table 3.4) indicate a loss of H_2O from the fluid inclusions after re-equilibration.

The calculated X_{CO2} from flat fi.s, after the initial experiment E421 is higher than the value calculated from the amounts silver-oxalate and water (Table 3.1). This discrepancy may result from impurities in the silver-oxalate or loss of substances during welding of the gold-tubes. The density calculated for the experimental conditions of E421 using the equation of state, described by Christoforakis & Franck, 1986 (CF-equation) is 21.6 mmol/cm³. The fluid density in the inclusions has been assumed to be equal to the density in the capsule, but the value is too low with respect to the densities, calculated from our volume estimations and solubility tables, of 34.7 and 32.9 mmol/cm³, respectively for cores 3 and 4. The theoretically calculated densities have been used to predict the $T_H(H_2O-CO_2)$, with data from Tödheide & Franck (1963), Takenouchi & Kennedy (1964), and Sterner & Bodnar (1991) on the miscibility gap in H_2O-CO_2 gas mixtures. The inaccuracy of the equation of state for H_2O-CO_2 mixtures in the vicinity of the miscibility gap does not permit exact prediction of T_H.

3.5.1 Type 1 fluid inclusions

Type 1 fi.s were expected to contain pure H_2O. The fluids have a density 23.9 $\pm$ 0.4 mmol/cm³ and 42.3 $\pm$ 0.5 mmol/cm³ (CF-equation) for E463 and E490 respectively. Homogenization should occur at 645 $\pm$ 1 and 528 $\pm$ 1 K to the liquid phase for E463 and E490 respectively (Fig.3.1).

The peak-frequency for T_H in E463 (Fig.3.3A) is in accordance with 645 K. The variations in volumetric proportions for E463 may also be attributed to the influx of some CO_2. This CO_2 must originate from original inclusions and is presumed to have migrated along fractures, resulting from the internal overpressure of approximately 100 MPa. The abundant presence of pure H_2O inclusions indicates that the CO_2 source was not available in the beginning of the experiment. The pure water inclusions were probably created in advance of decrepitation of the original CO_2 containing inclusions. By continued decrepitation, the free gas mixture in the capsule will be progressively enriched with small amounts of CO_2. Evidence for decrepitation in E463 was seen in the form of new microcracks around fi.s (Fig.3.8D).

The wide range of T_H in E490 (Fig.3.3B) indicates the existence of small amounts of CO_2 in the water phase. Although no signs of decrepitation or implosion are observed in E490, a similar process must have effected the T_H of type 1 inclusions, resulting in a range of elevated temperatures (Fig.3.3).

3.5.2 Type 2 fluid inclusions

When pressure-equilibrium is approached for the same H_2O-CO_2 gas-mixture in re-equilibration experiments as in the initial experiment, the theoratical fluid-density for E463 should decrease (15.7 mmol/cm³, CF-equation) and for E490 should increase (27.8 mmol/cm³, CF-equation). The T_H for E421 of 575 K, calculated using the CF-equation, is in accordance to the measured value of 576.1 and 575.6 K, respectively for cores 3 and 4. T_H, derived from our density calculation, is about 515 K.

48

Using available P-V-T-X data for the system CO_2-H_2O it is possible to predict T_H of re-equilibrated fi.s with constant volume assuming four different models of re-equilibration (Fig.3.10) :

1) Leakage of a H_2O-CO_2 gas mixture with composition 20 mol% CO_2 for E463 (Fig.3.10A) will keep the mole fractions constant. The position of the miscibility gap within the P-T field will then remain unchanged. Depending on the amount of leakage, T_H will lie between 575 K and a maximum of 613 K. Infiltration of the involved gas mixture for E490 was not possible as only H_2O was available outside the quartz core.

2) Preferential leakage of H_2O in E463 will produce an enrichment of CO_2 (Fig.3.10B) and will instantaneously lead to an increase of T_H to a maximum of 603 K, followed by a decrease until pressure-equilibrium is reached, at about 34 mol% CO_2 and 577 K.

3) Infiltration of H_2O for E490 will produce a low X_{CO2} (Fig.3.10C). T_H will vary between 575 and 539 K, depending on the amount of infiltration until pressure-equilibrium is reached at about 16 mol% CO_2.

4) As described by Bakker & Jansen (1990, chapter 2), leakage of fluid may occur under conditions of internal underpressure. Therefore, preferential leakage of H_2O and leakage of 20 mol% CO_2 gas mixture are considered for E490. The effects on T_H are similar to those described in 1) and 2).
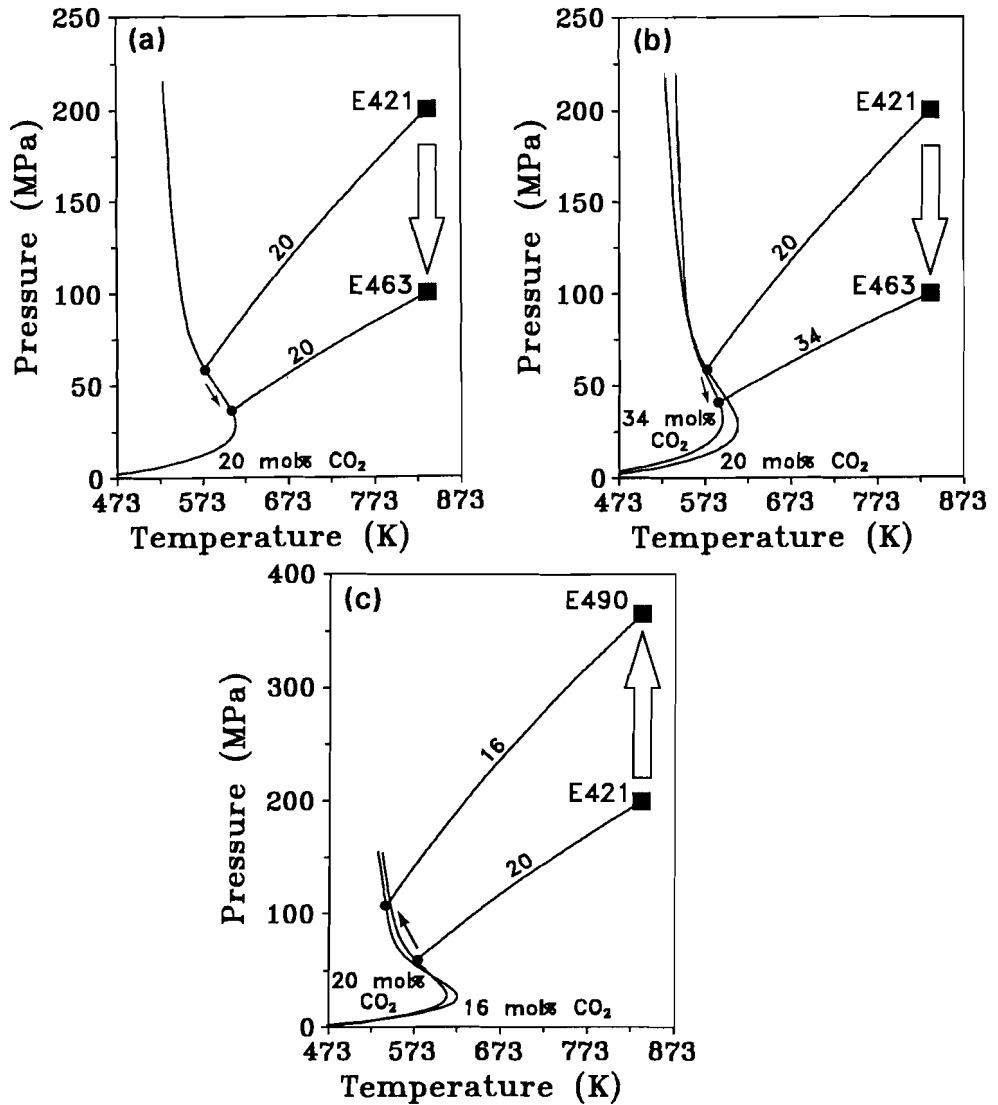
Figure 3.10

Models for the change in T_H in E463 and E490. Isothermal compression and decompression are indicated with large arrows. The small arrows indicate the corresponding PT-path of homogenization conditions. Miscibility gap of CO_2-H_2O mixtures is a compilation of data from Tödheide & Franck (1963), Takenouchi & Kennedy (1964), and Sterner & Bodnar (1991). (A) Leakage of 19 mol% CO_2 gas mixture in E463. (B) Preferential leakage of H_2O in E463. (C) Infiltration of H_2O in E490. The models are further explained in text.

50

Despite the large errors volume estimations indicate the leakage of H_2O from some inclusions (Table 3.4). The change in T_H due to leakage of gas mixtures or individual gas species is in accordance with the experimentally determined trend (Fig.3.11). The data from E490 (Fig.3.11B) suggest that model 3 is not operating.

A theoretical curve, using the CF-equation, for type 2 fi.s giving the relationship between T_H and mol% CO_2, based on preferential leakage of H_2O, is superimposed on Fig.3.11 (Curve 3). The derived best fit through our data (Fig.3.11, curves 1 and 2 for E463 and E490 respectively) does not match the theoretical curve 3. Theoretical curve 4 with initial lower densities (17 mmol/cm^3) and higher mole fractions CO_2 (35%), plots the nearest to our best-fit curves 1 and 2. Therefore, the large error possible in volume estimations, inaccuracy of the CF-equation or extreme non-ideal mixing behaviour of H_2O and CO_2 near the miscibility gap may result in deviations from the calculated theoretical curve.

The data from E463 (Fig.3.11A) having relatively high T_H and low mol% CO_2 values, can be explained by micro-cracking around fi.s due to the internal overpressure (Fig.3.8D). This volume increase causes data from curve 1 to shift to higher T_H, while the mol% CO_2 remains constant. Volume decrease for E490 (Fig.3.11B) at constant mol% CO_2 causes T_H to shift to lower values. It is suggested that the large amount of solution and precipitation at the walls of the fi.s in E490 (Fig.3.9B and C), is evidence of this volume decrease.

The amount of gas leakage, evident in most fi.s (Fig.3.8B, C and 3.9B, C), cannot be accounted for by optically observed features. Four mechanisms of fluid leakage during experimentation may be evaluated.

3.5.3 Point defects

Diffusion of H_2O via point defects through quartz may contribute to leakage from fluid inclusions. The mobility of water species through quartz was proved by the determination of water concentrations in bubbles in synthetic quartz after heating to 1173 K at 300 MPa (Balderman, 1974; Paterson &
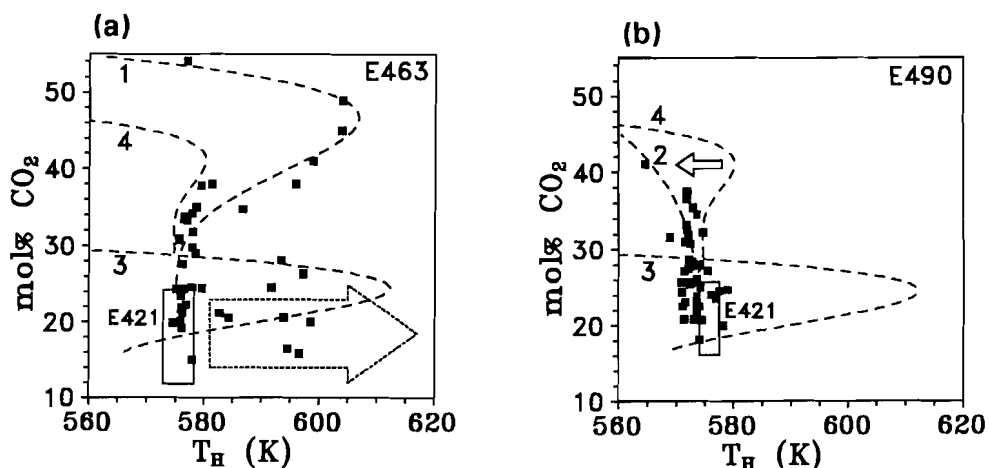
Figure 3.11.

T_H-X_{CO2} *diagrams for type 2 fi.s of E463 (A) and E490 (B). All data from
the original experiment E421 lie within the large rectangles. Data of the
re-equilibration experiments are indicated by small squares. Dashed
curves 1 and 2 are best-fits through the data from E463 and E490,
respectively. Dashed curve 3 is the theoretically H_2O leakage relation
between T_H and X_{CO2} based on the initial 17.8 mol% CO_2, the CF-
equation of state, and the experimentally derived miscibility gap for the
H_2O-CO_2 gas mixture (Tödheide & Franck, 1963; Takenouchi & Kennedy,
1964; Sterner & Bodnar, 1991). Dashed curve 4 is a curve based on the
same theory with an initial mol% CO_2 of 35, which seems to fall between
and fit best the main data points of both diagrams. The horizontal arrows
indicate the effect on T_H for E463 and E490 due to volume increase and
volume decrease, respectively. Notice the decrepitation in E463 (also
Fig.3.8D).*

Kekulawala, 1979; McLaren et al., 1983).

Estimations of the bulk-diffusion coefficient vary between 10^{-10} at 1273 K (Blacic, 1981; Kronenberg et al., 1986) and 10^{-23} m^2/s at 773 K (Dennis, 1984), depending on the diffusing species (O, H, OH or H_2O), direction of diffusion and experimental conditions.

Taking into account our experimental conditions, the diffusion coefficient is likely to be in the order of 10^{-23} m^2/s. The transport distance, roughly expressed by the term $(Dt)^{1/2}$ (Fletcher & Hofmann, 1974) is 1.5 nm during the experiment. Assuming the water solubility in quartz to be 100 H/10^6Si, an inclusion of radius 5μm would only lose 5×10^{-7} mol% H_2O. Therefore, diffusion by point defects is too slow to be effective in leakage of H_2O from the inclusions within the experimental time.

3.5.4 Dislocations

Diffusion of water species through dislocations in quartz was elucidated by Roedder & Skinner (1968), Griggs (1974), McLaren et al. (1983), Doukhan & Trepied (1985) and Hollister (1989). Dislocations should not be considered as open channels in the quartz crystal through which H_2O and CO_2 can leak or infiltrate by capillary flow, but as distortions of the crystal lattice on a nanometer scale. However, H_2O and CO_2 are likely to diffuse faster through the crystal along dislocation cores, where there is more space for movements, than through a system of point defects. The pipe diffusion coefficient (Yund et al.1981) can be five orders of magnitude larger than the bulk diffusion coefficient by point defects. Fi.s connected to dislocation loops, as described by McLaren et al.(1983) and Doukhan & Trepied (1985), are observed in our experiments (Fig.2.3). Mobile dislocations discontinuously tapping fi.s may become saturated with water and carry small amounts from the inclusions through the quartz crystal. Futhermore, fi.s are principally major imperfections and may act as sources for dislocation multiplication. Deviatoric stress states around fi.s, caused by the internal over- or underpressure may stimulate mobility of dislocations. Preferential H_2O

leakage may result from both physical and chemical interaction between the hydrophilic quartz surface and the water dipoles, causing local immiscibility at the inclusion walls and in dislocation cores. Even at experimental re-equilbration conditions, the inclusion walls may be coated by a molecular film of H_2O. This prevents CO_2 molecules from escaping from the fi.s through routes available at these walls. H_2O loss is a result of enhenced solution of H_2O with respect to CO_2 in and around the dislocation core. The exact process by which fractionation may occur could involve diffusion controlled fractionation due to different molecular sizes.

If a dislocation is saturated with H_2O, the stress potential cloud, visible using the TEM (Fig.2.3), contains 50-100 times as many H_2O molecules as are bound in the dislocation core (edge of the half plane, Griggs 1974). Assuming that dislocations have an average length of 1 mm and a core radius between 0.25 (Yund et al.1981) and 1 nm (Hirth & Lothe, 1968), and that they are connected with fi.s, under internal overpressure, they will become saturated with H_2O. We calculated that about 33 mobile dislocations have to pass a H_2O rich inclusion of radius 5 μm in order to lose 20 mol% of its contents.

3.5.5 Channels

In Fig.3.6A, crystal growth along the crack is irregular. This growth is dependent on the crack wall morphology and experimental conditions. As our photographs (Fig.3.4) reveal, crack healing processes do not restore the quartz to a perfect crystal. Besides many built-in defects small channels with a maximum diameter of 0.1 μm (Fig.3.4), which are optically invisible, are the only remaining portions of the crack. The observed fi.s are connected to a maximum of 10 channels (Fig.3.7 reveals only 4 channels). In E463, with an overpressure gradient of 100 MPa, capilary flow through these channels may be an effective mechanism for fluid transport. H_2O-CO_2 fluids in pores with diameters less than 2.5 nm differ in composition (richer in H_2O) from the bulk fluid in the inclusion (Belonoshko, 1989). Therefore, local immiscibility

54

of H_2O-CO_2 gas mixtures may occur even at P-T conditions outside those for the determined miscibility gap. Fluids in small channels may differ in composition from fluids in the larger inclusions. Capillary fluid separation (Watson & Brenan, 1987; Yardley & Bottrell, 1988) which is effective within the miscibility gap at low P-T conditions, may also cause preferential leakage of H_2O at conditions of presumable total miscibility. For E490 infiltration of H_2O was expected due to the existence of a reversed pressure gradient, this was not observed.

The internal pressure in fi.s at room conditions (293 K and 0.1 MPa) is about 4 MPa for both experiments E463 and E490. Therefore, cappilary flow of fluid out of fi.s is expected if the channels interconnect the surface of the quartz core and the fi.s. However, the fi.s do not seem to change in compositon or density after the experiments.

3.5.6 Cracks

The importance of cracks developed during experimentation was pointed out by several authors (Pècher, 1981; Griggs, 1974; Brok & Spiers, 1991; Kronenberg et al., 1986; Gerretsen et al., 1989). They emphasize the importance of extensive microcracking as a mechanism by which molecular water may enter quartz, in addition to a mechanism of dislocation slip during deformation experiments. We observed newly developed cracks only in experiment E463. Preferential leakage would occur, if the thickness of the cracks were less than 2.5 nm (Belonoskho 1989), in the same manner as previously described (3.5.5 Channels). These nanocracks were not observed with an optical microscope and SEM.

3.6 GEOLOGICAL APPLICATIONS OF OUR EXPERIMENTS

3.6.1. Natural fi.s in metamorphic quartz

The processes of cracking and crack-healing within quartz grains occur often during the deformation of metamorphic rocks and are witnessed by trails of fi.s. Assuming the natural crack-healing process to be principally similar to our experimental process, preferential leakage of H_2O out of initially H_2O-rich inclusions may occur during uplift and cooling. We expect the leakage mechanisms that have operated during our short experimental runs, and have already been discussed, to be more effective in real geological processes. TEM-photomicrographs of natural fi.s often reveal many dislocations connected to inclusions. Primary fi.s change in density and composition, the amount of change being dependent on the extend of deformation, due to H_2O transport by means of dislocations and imperfections or through channels and nano-cracks.

3.6.2 Isothermal decompression, as examplified by the rocks on Naxos (Greece)

The main part of the island of Naxos consists of a metamorphic complex of alternating schists and marbles surrounding a central migmatite dome. The peak-metamorphic grade generally increases towards the dome. Fi.s in quartz lenses from Naxos have been investigated extensively by Kreulen (1977, 1980) and he suggested that they are predominantly CO_2-rich with minor amounts of H_2O. The composition of the optically studied fi.s seemed to be independent of metamorphic grade and lithology, in contradiction to the mineral reaction path buffered by the siliceous dolomites (Jansen et al., 1978). Fi.s contain 60-90 mol% CO_2 from optical estimates (Kreulen, 1980). However, collecting gasses in a vacuum line after decrepitation of the fi.s,

resulted in 6-91 mol% CO_2 (Kreulen, 1977).

At the end of the main metamorphism, there was a considerable drop in P_{TOTAL} of at least 300 MPa (Jansen et al., 1977; Buick & Holland, 1989) accompanied by an extensional penetrative deformation (Lister et al., 1984; Urai et al., 1990) with corresponding folding (Papanikolaou, 1986) and the resetting of isogrades towards the center of the dome (Jansen et al., 1989). Of course, the final fluid densities in the fi.s are much lower than those expected for peak-metamorphic conditions, calculated from petrological and geothermometrical data. Practically all water-rich inclusions must have leaked selectively or decrepitated during the pressure-drop. Fi.s were exhumed, resulting in a more CO_2-rich composition, while small H_2O-rich fi.s developed in the newly grown micro-cracks caused by decrepitation. There exists a positive correlation between X_{CO2} and the size of the fi.s (F.Postma, pers. comm. 1990).

The optically established X_{CO2} in the inclusions (Kreulen, 1980) is much too high for various mineral assemblages. For example, the occurrence of epidote minerals requires that CO_2 content of the metamorphic fluid did not exceed 10 mol% (Jansen & Schuiling, 1976; Jansen et al., 1989; Baker et al., 1989). The post-peak metamorphic P-T path approaches an isothermal decompression. Therefore, the anomalous values for the densities and compositions of fi.s from Naxos can be explained by comparison with the observed changes in the isothermal decompression experiment E463.

3.6.3 Isobaric cooling, as examplified by the rocks on Rogaland (SW Norway)

Swanenberg (1980) conducted an extensive study of fi.s in rocks from Rogaland (Norway). Here are found anorthosite complexes, a lopolith of monzonoritic to noritic composition with its surrounding high grade metamorphic envelope. Jansen et al. (1985) and Maijer & Padget (1987) have recognized three Proterozoic metamorphic episodes : M1, old regional metamorphism; M2, peak granulite facies metamorphism resulting from the

thermal event associated with the intrusive masses; M3, the widespread introduction of fluid during regional cooling (decomposition of M2 minerals). The fi.s have wide ranging compositions (Swanenberg, 1980; Kerkhof et al., 1991) within the CO_2, CH_4 and N_2 triangle.

There are many discrepancies between the metamorphic P-T path derived from the mineral assemblages of Rogaland and the isochores of the measured densities and compositions of fi.s. Firstly there are metastable mixtures of CO_2 and CH_4, and secondly, both low and extremely high densities are observed.

The gas mixture CO_2-CH_4 is chemically unstable and should react to H_2O and graphite, until H_2O makes up approximately 80 mole% of the fluid. A metastable CO_2-CH_4 mixture may remain after preferential water leakage if the threshold energy for their reaction is too high.

Low densities cannot be explained by recrystallization of the quartz, which occurred at conditions of higher densities. However, these low densities can be explained by assuming partial leakage of gasses. This phenomena was observed in the experiment E490 and is also described previously by Bakker & Jansen (1990, **chapter 2**).

High density CO_2 inclusions result from the post entrapment re-equilibration of pre-existing inclusions towards the higher densities reached by near isobaric cooling (Swanenberg, 1980; Kerkhof et al., 1991). However, several high densities are out of range of the post metamorphic trajectory. We propose simultaneously operating mechanisms of post-peak metamorphic re-equilibration and volume adjustments, leading to the very high density inclusions.

3.7 CONCLUSIONS

1) In hydrothermal recrystallization experiments with quartz containing H_2O-CO_2 fi.s with 19 and 21 mol% CO_2 density decreases are obtained under near-constant volume conditions by both preferential leakage of H_2O and leakage of the gas-mixture.

2) Preferential leakage of H_2O occurred in experiments which simulated both isothermal decompression (E463) and isothermal compression (E490), despite the reversed pressure- and water fugacity gradient in E490.

3) Leakage of H_2O must have proceeded by diffusion along mobile dislocation lines, while point defect diffusion cannot be responsible for the amount of leakage involved. The high density of defects within the healed crack, as established by TEM work, may indicate that the former crack as a whole may have provided an important route for the leakage for gas species out of the inclusions.

4) We propose that re-equilibration as described in our experiment would be effective in metamorphic quartz, during cooling and uplift.

5) In natural rocks fi.s are often assigned to several generations of fluid with variable compositions, leading to the assumption of an extensive varity of metamorphic fluids, that may have passed through the vein. These experiments clarify that a wide compositional range of fi.s can be generated from one type fi.s by H_2O-leakage initiated by local recrystallization, which is not necessarily uniform, even in an individual healed crack.

6) Metamorphic conditions obtained by isochore-extrapolation and -intersection are non-realistic when information regarding quartz recrystallization, and from valid geothermometry and geobarometry on coeval mineral assemblages is lacking.

7) CO_2-rich fi.s which are claimed for most high-grade rocks have not necessarily always been CO_2 rich, but might have contained high quantities of H_2O.

8) The supposed trend that deep rocks, such as granulites and mantle rocks, contain more CO_2 than H_2O in fi.s may partly be caused by the fact that before exposure, these deep rocks have usually suffered more intensive recrystallization during uplift than shallow rocks.

Fig. 13.
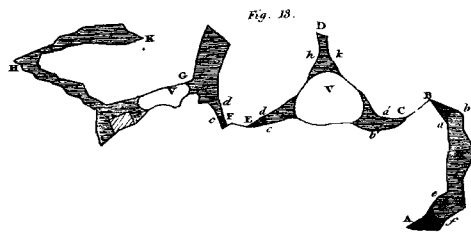
Chapter 4

A MECHANISM FOR PREFERENTIAL H_2O LEAKAGE FROM FLUID INCLUSIONS IN QUARTZ, BASED ON TEM OBSERVATIONS

4.1 INTRODUCTION

4.1.1 Naxos, a case study

Most natural aqueous fluid inclusions (fi.s) in metamorphic rock were considered to have leaked preferentially H_2O (Hollister, 1988, and 1990). Water leakage was assumed for metamorphic rocks which experienced PT conditions that were not corresponding to the specific isochore of the trapped fluid at peak metamorphic conditions, as exemplified by rocks from Naxos (Greece). The metamorphic and structural history of Naxos was extensively investigated by Jansen & Schuiling (1976), Andriessen et al. (1979), Kreulen (1980), Buick & Holland (1989, 1991), Urai et al. (1990). An early metamorphic event, M1 (Fig.4.1) was characterized by glaucophane-bearing assemblages. The main metamorphic phase, $M2_A$ and $M2_B$ (Fig.4.1) affecting Naxos formed a Barrovian facies series. The solid arrows in Fig.4.1 represent pressure decrease, caused by crustal extension towards $M2_C$, which promoted regional exhumation of the metamorphic complex (Buick, 1991). Kreulen (1980) described an abundance of peak metamorphic $M2_B$ CO_2-rich fi.s in unselective quartz lenses throughout the metamorphic complex, irrespectively of lithology, metamorphic grade, or event. However, many fluid densities were too low with respect to peak metamorphic $M2_B$ conditions, and they resembled typical values for the $M2_C$ re-equilibration. Mineral assemblages which were stable at $M2_B$ conditions

61

buffered volatile species to high X_{H2O} values in epidote/zoisite bearing schists, in amphibolites, and in vesuvianite bearing calcsilicates (Jansen & Schuiling, 1976; Buick & Holland, 1991). Locally, high X_{CO2} values were determined in siliceous dolomites (Jansen et al., 1978; Buick & Holland 1991). Although the observed mole fraction of CO_2 in fi.s was not related to lithology, the carbon-isotope ($\delta^{13}C$) data on experimentally decrepitated fi.s in quartz lenses (Rye et al., 1976; Kreulen 1980) seemed to be characteristic in siliceous dolomites and in graphite bearing quartzites. Therefore, compositional modification by selective leakage of H_2O during quartz recrystallization must have occurred, leaving behind CO_2 enriched fi.s.
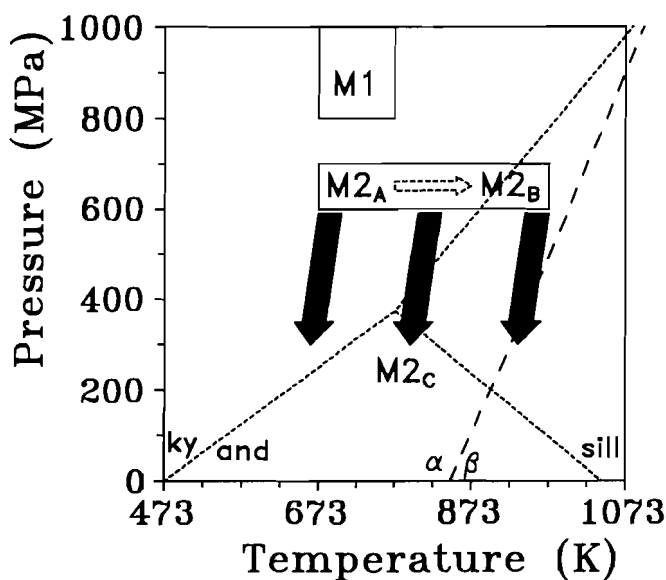
Figure 4.1.

Pressure-Temperature diagram. Three main metamorphic events are M1, blueschist facies; M2$_A$, regional greenschist facies which locally reached to M2$_B$ upper amphibolite facies; and M3$_C$, the metamorphism after uplift of the complex during extensional thinning of the crust (indicated with 3 black arrows). The short-dashed lines indicate the triple point of Al_2SiO_5 (Holdaway, 1971), and the large-dashed line indicate the transition of α-quartz to β-quartz (Hosieni et al., 1985).

62

4.1.2 Experiments

Synthetism of CO_2-H_2O fi.s in Brazilian quartz (Bakker & Jansen, 1990, 1991b in **Chapter 2** and **Chapter 3**) is performed to prove that non-decrepitative H_2O leakage may occur during re-equilibration, changing density and composition. Fi.s were synthesized through crack healing in Brazilian quartz. Several stages of the evolution of a re-equilibrated experimentally healed crack in Brazilian quartz with numerous synthetic fi.s are visualized with TEM, in order to explain preferential H_2O leakage. The experiments (Fig.4.2) mimic altering P-T conditions during the evolution of rock similar to the metamorphic evolution of syn- and pre-$M2_B$ quartz lenses from Naxos, during isothermal compression, and additionally, during the recorded pressure decrease towards $M2_C$ (Fig.4.1). Fi.s in quartz lenses from Naxos are compared to ensure that the experimental results are relevant for natural circumstances of pressure release.
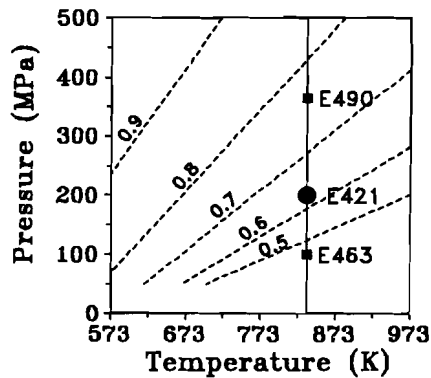
Figure 4.2.
Pressure-Temperature diagram indicating the conditions of the initial experiment (E421, black dot) and the re-equilibration experiments E463 and E490 (black squares), which have been extensively described in **Chapter 3**. *The initial experiment was performed at 835 K and 200 MPa. The isochores 0.5, 0.6, 0.7, 0.8, and 0.9 g/cm³ of pure H_2O (Fisher, 1974) are projected in the same diagram. The solid line indicates the temperature of 835 K which was used for all experiments.*

4.1.3 Review and intentions

Lämmlein (1929) was the first to relate experimentally crack healing processes with the occurrence of secondary fi.s. Capillary condensation and the tendency of the phase boundary to assume the form possing the least free surface energy were proposed by Lemmlein (1956) to be the mechanism of crack healing. A solution became supersaturated upon entering into a capillary fracture due to surface energies, and material was redeposited on the wall in the narrower part of the crack (Lemmlein, 1956). As lateral branches of two rows of growing dendrites joined, portions of the solution were isolated. Nicols & Mullins (1965) considered surface diffusion which was activated by surface tension, as a mechanism of effective material transport in capillary cracks. Carstens (1968, 1969) noticed that healed fractures in natural quartz were associated with an abundant amount of arrays of dislocations. Dislocations were formed during the healing process owing to the impingement of lattices with different orientation (opposite crack walls), and the perfect crystal structure could not be restored.

In this study, a mechanism for non-decrepitative preferential H_2O leakage is assumed to be strongly related to diffusion, solution and precipitation processes associated with crystal defects. Crystal defects in natural quartz have been visualized with transmission electron microscopy (TEM) since studies on deformation mechanism suggested plastic deformation to be associated with dislocation glide (McLaren & Phakey, 1965; Doukhan & Trepied, 1985; McLaren, 1991). To explain the hydrolytic weakening phenomenon in natural and synthetic quartz, water related point defect diffusion through the crystal and water enhanced mobility of dislocations were intensively studied. Water may be incorporated in quartz as H_2O related point defects including interstitials and substitutes (Brunner et al., 1961; Kats, 1962; Griggs, 1974; Paterson & Kekulawala, 1979; Nutall & Weil, 1980; McLaren et al., 1983; Dennis, 1981, and 1984; Hobbs, 1984; Kronenberg et al., 1986), as clusters of non-freezable water (Aines et al., 1984), as small bubbles (McLaren et al., 1983), and as larger optically visible fi.s. The solubility of the water related point defects in quartz was theoretically (Paterson, 1986) and experimentally (Aines et al., 1984;

64

Gerretsen et al., 1989) estimated to be less than 100 H/10⁶Si, even at high pressure and temperature, which was very low. The main argument for water related point defect diffusion in synthetic quartz and natural amethyst was the formation of small bubbles during annealing experiments (McLaren et al., 1983; Gerretsen et al., 1989). The measured diffusion of any water related point defect is too slow for significant penetration of single crystals. High penetration depth of molecular H_2O in quartz crystals was suggested by Kronenberg et al. (1986) to result from microcracking and crack healing, in addition to dislocation slip. In this study, dislocations and planar defects are assumed to play a major part in molecular H_2O diffusion through quartz crystals.

4.2 SAMPLE PREPARATION

Fluid inclusions are synthesized in a 4 mm diameter cylindrical quartz core, which is drilled from a crack- and inclusion-free natural Brazil quartz crystal. Micro-cracks are introduced by a thermal shock. The core and a mixture of 20 ± 2 mol% CO_2 and 80 ± 2 mol% H_2O are enclosed in a arc-welded gold capsule. Crack-healing is performed at 835 K and 200 MPa confining pressure (initial experiment E421 in Fig.4.2) in a externally heated 75 mm diameter Tuttle type pressure vessel with an argon pressure medium, analogue to the method of Sterner & Bodnar (1984) for fi.s synthesis. The density of the fluid in the inclusions reflects practically one homogenization temperature which is in accordance with the experimental conditions (Bakker & Jansen, 1991b in **Chapter 3**). Re-equilibration is performed in a H_2O rich fluid at 100 MPa and 835 K (E463 in Fig.4.2), and at 365 MPa and 835 K (E490 in Fig.4.2) causing overpressure and underpressure circumstances in synthetic fi.s.

Natural quartz lenses are collected by F. Postma in Naxos (Greece). The quartz lenses are cut into 2 mm thick slices, and further thinned to 30 μm by polishing, for characterization of the fi.s composition and density.

The natural quartz lenses and the experimentally treated Brazil quartz crystals are prepared by ion-bombardment from ± 15 μm thin-sections and examined in a JEOL 200 electron microscope, operating at 200 kV.

4.3 EXPERIMENTAL RESULTS

After the initial experiment at 835 K and 200 MPa and before re-equilibration, one quartz core with partly healed cracks is prepared for investigation with the TEM. In general, crystal defect density is very low within these TEM-samples. No crystal defects are detected in the original Brazilian quartz before the initial experiment E421. Elongated synthetic fi.s occur within healed cracks of ± 1.5 μm thickness. The length/wide ratio of fi.s is maximally 10. The long sides of the inclusions coincide with the direction of the original crack walls, and the short sides are defined by newly grown quartz in the crack. A few dislocations and other crystal defects are observed in the newly grown quartz between synthetic fi.s in the healed cracks. Only several straight dislocation lines (Fig.4.3) are observed, orientated parallel to a crystallographic $\bar{a}$ direction. The apices of the dislocations mark the position of the former crack wall. The dislocation lines are oblique to the former crack wall. A quartz crystal which has been continuously exposed to an electron beam for more than half an hour shows electron beam damage centres. In Fig.4.3 several electron beam damage centres are recognized, which are nucleate in the crystal and grow at a noticeable speed.

The amount and variety of crystal defects in re-equilibrated samples (E463, and E490) is much higher (Fig.4.4) for both types of experiments (under- and overpressurized fi.s) than for the initial experiment (Fig.4.3). The observed crystal defects are limited to the quartz in the healed cracks.
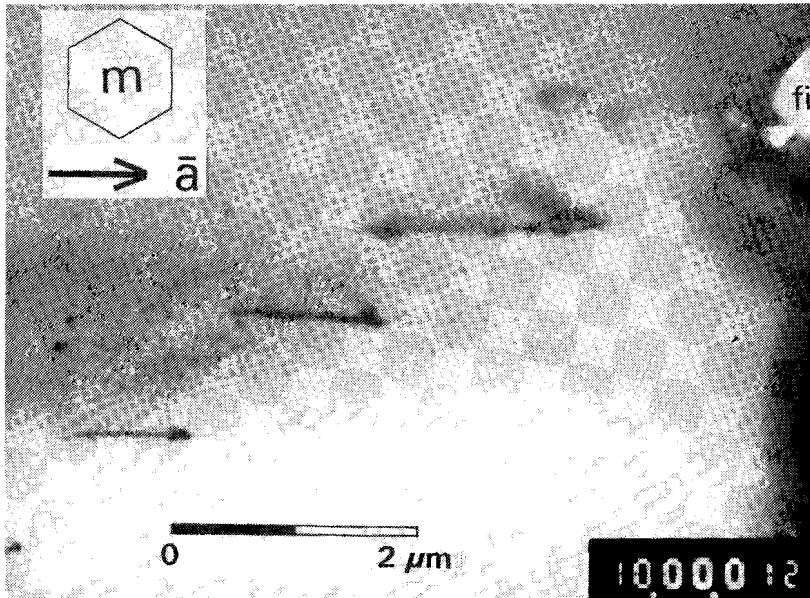
Figure 4.3.
Bright field electron micrograph (TEM) of a healed crack after the initial
experiment. The orientation of the micrograph is indicated with a
hexagon, representing the intersection of prismatic planes (m) of quartz
with the photographic plane of projection. The crystallographic direction
$\bar{a}$ is expressed with the arrow. Five parallel dislocations (straight black
lines) are present between fi.s (fi). The black spots between the
dislocations are radiation damage centres.

The occurrence of dislocations is associated with fi.s of variable sizes. A set
of seven straight semi-parallel dislocations are connected to an inclusion with
a diameter of 4 μm (Fig.4.4A), whose shape is arbitrarily related to a-quartz
crystallographic orientations. A similar configuration was described by Bakker
& Jansen (1990, **Chapter 2**) for underpressurized fi.s at lower temperature
(673 K).

67

Figure 4.4.

*Bright filed electron micrograph (TEM). In (A), (C), (D), and (F) the orientation of the micrograph (see Appendix) is indicated with a hexagon (intersection of prismatic planes **m** with the photographic plane of projection). The short dashed line in (A), (B), (C), (D), and (F) represent the intersection with the basal plane of quartz. The arrow in (B) is the crystallographic direction $\bar{c}$. (A) E463, a single inclusion (fi) connected to seven straight dislocation lines. (B) E490, a trail of fi.s (fi) with several dislocations and small bubbles. Foccussed on the left, some bubbles are positioned at dislocations, others are isolated between fi.s and dislocations. No electron beam damage centres are observed. (C) E463, a hexagonal network of dislocations, marking the former crack walls. Several bubbles occur at dislocations and others are located between dislocations. The network pass into a trail of small bubbles. (D) E490, a synthetic inclusion (fi) connected to about 8 irregularly shaped dislocations. In total 62 small bubbles are observed only at the dislocations. (E) E463, small features of strain contrast, which are disk-shaped in the center, and have equal shape halos on both sides. No electron beam damage centres are observed. (F) E463, Dauphiné twins connected to an inclusion (fi), which is out of focus on the right. (G) E490, Dauphiné twins marking the healed crack, and passing into a trail of small bubbles. (H) E463, a single isolated inclusion (fi) which occur in a trail of small bubbles. No crystal defects are observed.*

(a)
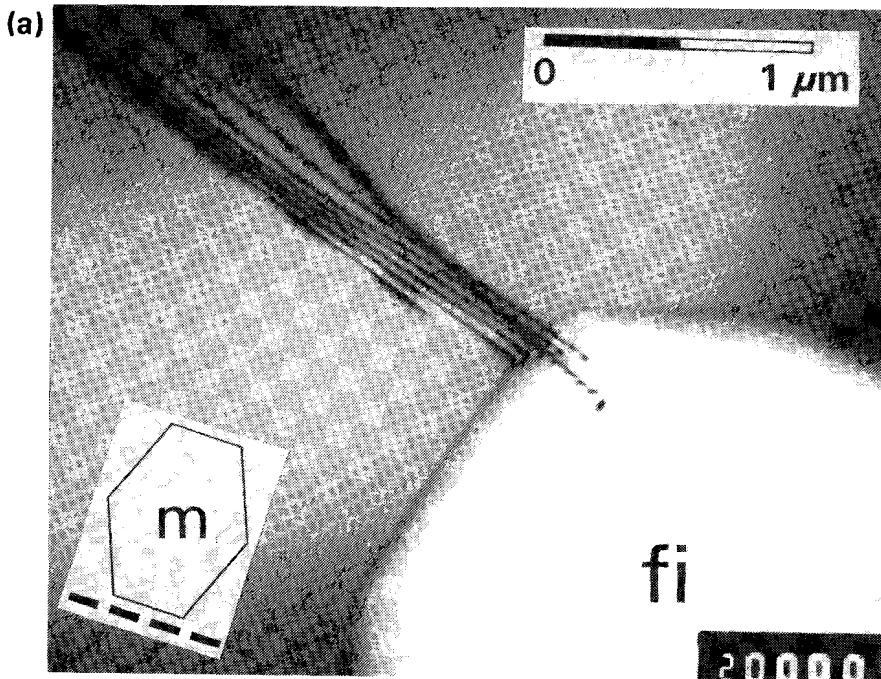
Figure. 4.4. (Continued)

Fig.4.4B reveals a trail of fi.s with diameter varying between 0.3 and 0.7 μm. The rhombohedric planes are strongly developed compared to the prismatic planes. Within the healed cracks between these fi.s several irregular curved dislocation lines occur. These dislocations contain small spheroidal bubbles of 20 nm diameter. Other small bubbles occur isolated in the newly grown quartz. They are not observed in the original Brazilian natural quartz, and in the healed cracks after the initial experiment. Within healed cracks, dislocations may be arranged in a hexagonal network (Fig.4.4C). The termination of the network indicates the position of the former crack walls, which is now the boundary between the original Brazilian quartz and the newly grow quartz. Similar to Fig.4.4B, many small bubbles of about 20 nm diameter are visible between dislocations and some are positioned at dislocation lines.

69

(b)

Figure 4.4. (Continued)

70

(c)
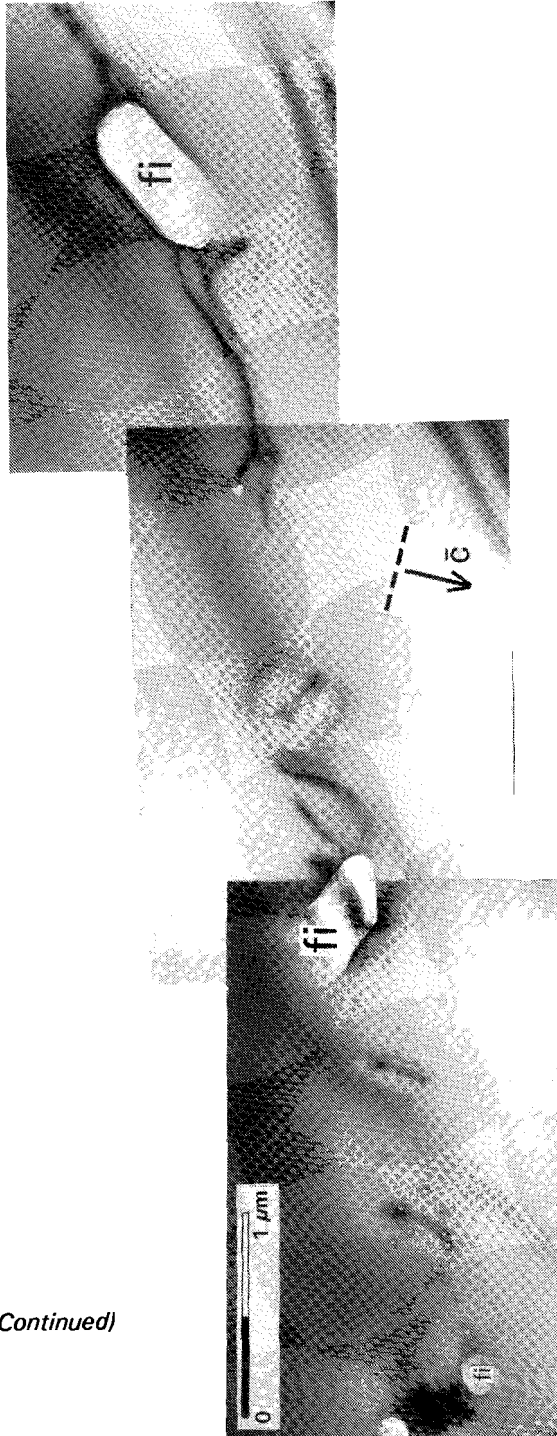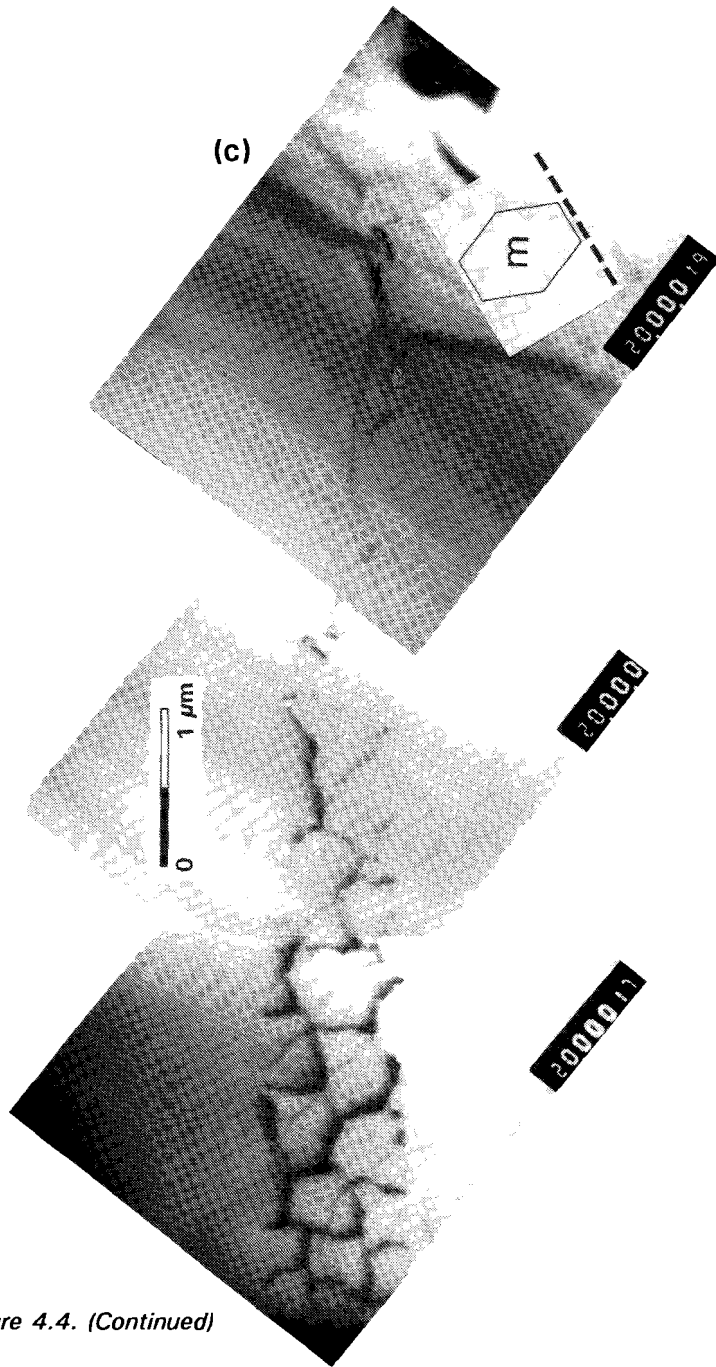
Figure 4.4. (Continued)
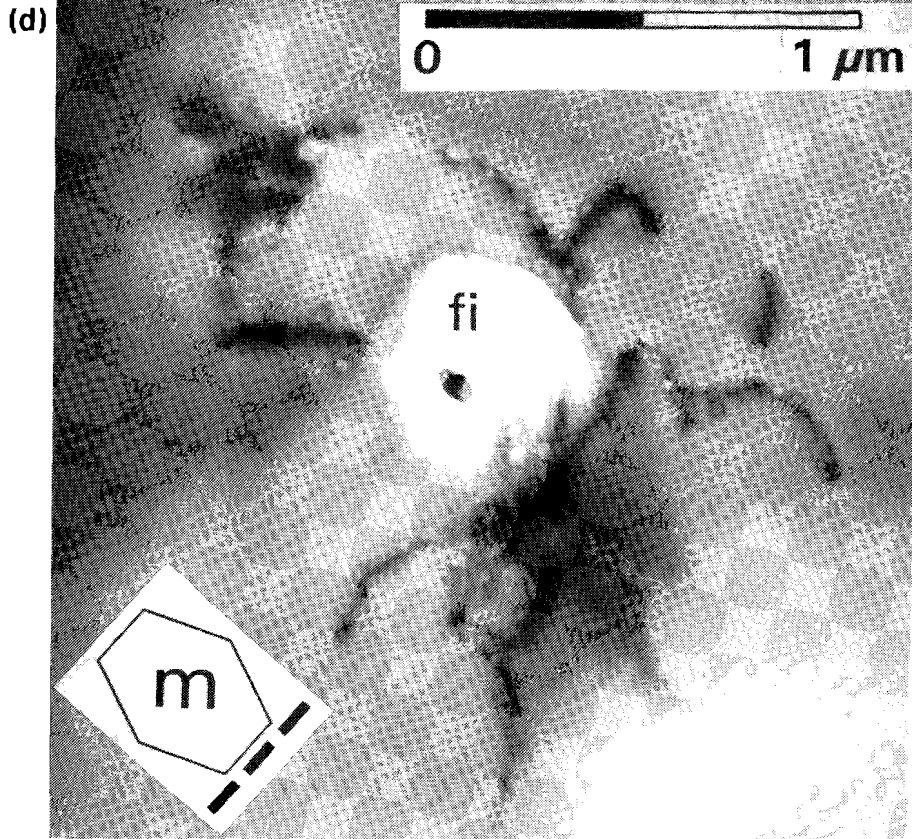
Figure 4.4. (Continued)

A spheroidal inclusion of 0.5 μm diameter (Fig.4.4D) is connected to dislocations with variable orientations. Each dislocation has up to twelve small bubbles of 35 nm diameter. In total, 62 small bubbles form a halo around the larger inclusion. Volume ratio between the large inclusion ($6.55 * 10^{-20}$ m^3) and the small bubbles ($\pm$ $2.26 * 10^{-23}$ m^3) is approximately 2900/1. Healed cracks are also marked with numerous features of small strain contrast (Fig.4.4E), which have a maximum diameter of 100 nm. The features are disk-shaped in the centre and have at both sides equal shaped

72

strain contrast halos. Planar defect structures which are expressed in fringe patterns, are connected to fi.s (Fig.4.4F). The patterns have distinct crystallographic orientations, parallel to $\{11\bar{2}0\}$ and $\{11\bar{2}1\}$. The $\{11\bar{2}0\}$ planes are arranged in prismatic configurations. The $\{11\bar{2}1\}$ and $\{11\bar{2}0\}$ planes are ordered in a rhombohedric mode. Thickness extinction contours are discontinuous on passing the fringes. The fringe pattern is symmetrical in the bright-field mode of the electron microscope, the outer fringes are either light or dark. Previously mentioned features of small strain contrast (Fig.4.4E) are observed near these fringes (Fig.4F).
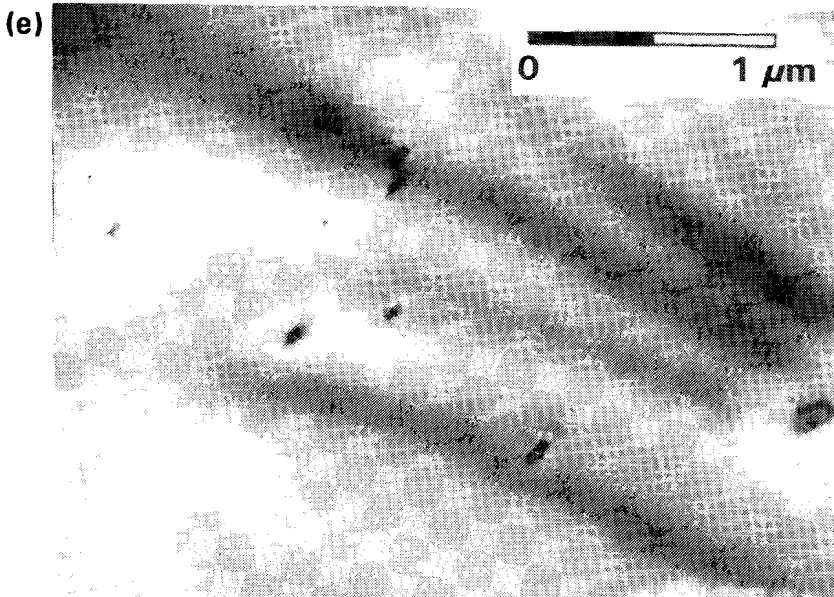
Figure 4.4. (Continued)

In Fig.4.4G, the healed crack is marked with a wide trail of small bubbles of 20 nm diameter, which pass into a fringe pattern. An additional fringe on passing a thickness extinction contour is created by forking of the central fringe. The termination of this pattern is a series of five small bubbles, which are located at a dislocation line. The dislocation line itself is out of contrast (Fig.4.4G). Mosaic fringe patterns may occur at positions of overlapping fringes. Finally, large fi.s may occur isolated without any of the previous mentioned features (Fig.4.4H). A large inclusion of 1 μm diameter and a series of small bubbles of 20 nm diameter occur in one trail. The shape of the large inclusion resembles a negative α-quartz crystal. The small bubbles have a spherical shape.

Figure 4.4. (Continued)

(h)
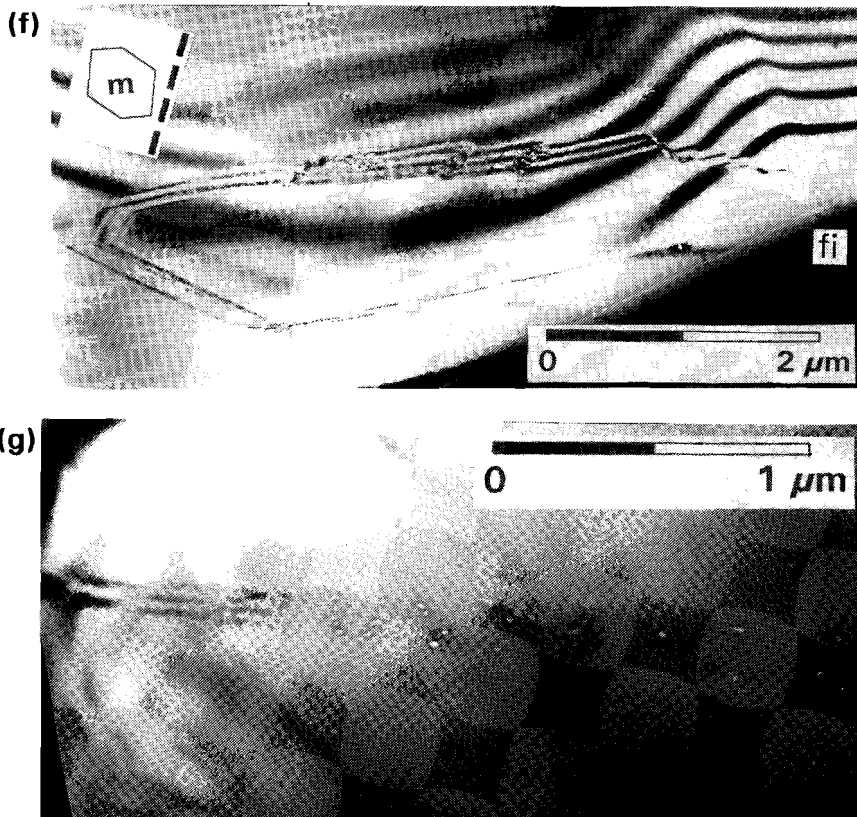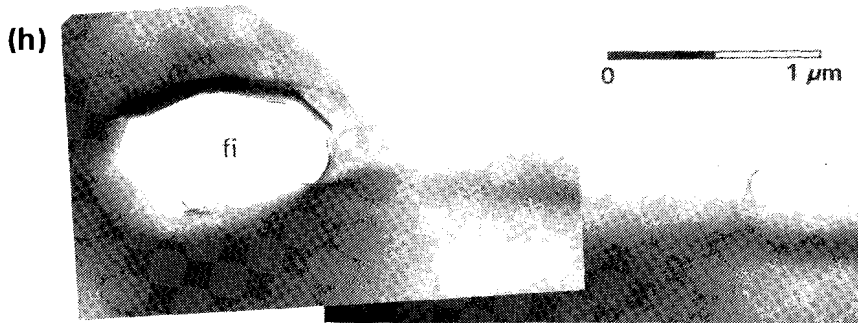
Figure 4.4. (Continued)

4.4 INTERPRETATION OF MICROSTRUCTURES

No electron beam damage centres are recognized in the electron micrographs in Fig.4.4E and 4.4F, revealing small strain features. Therefore, these features seem to be identical to features described by McLaren et al. (1983) in synthetic quartz and natural amethyst. They thought the features to represent strain around small lens-shaped H_2O inclusions (clusters) with high densities ($\pm$ 1.25 g/cm^3). The clusters were proposed to play an important role in hydrolytic weakening of quartz during deformation experiments (Aines et al., 1984). Annealing experiments caused the clusters to grow to distinct spherical small bubbles on dislocation loops. The small strain features in Fig.4.4E and 4.4F are proposed to be identical to clusters described by McLaren et al. (1983). The presence of these clusters in healed cracks (Fig.4.4E and 4F) indicates that the H_2O-concentration is higher than the original Brazilian quartz. Gerretsen et al. (1989) observed similar clusters in epitaxial overgrowth of a single quartz crystal. They calculated that the total amount of H_2O incorporated in the overgrown crystal is present as clusters and small bubbles. The halo of small bubbles on dislocations around a larger re-equilibrated synthetic fluid inclusion in Fig.4.4D is proposed to develop through bubble growth at dislocations. Quartz may be dissolved in the small bubbles, transported along dislocations, and precipitated in the larger fluid

75

inclusion. The total volume of the small bubbles in Fig.4.D is about 10% of the volume of the central inclusions. The growth of small bubbles may lead to optical visible "implosion halos", which have been recognized by Sterner & Bodnar (1989) and Bakker & Jansen (1991b, in **Chapter 3**). Like small strain features (clusters), the small bubbles may occur isolated within the healed cracks between dislocations and fi.s (Fig.4.4B, 4.4C and 4.4G). The small bubbles are assumed to result from annealing during the re-equilibration experiments, similar to the experiments of McLaren et al. (1983) and Gerretsen et al. (1989).

After the initial experiment (Fig. 4.3) the dislocations in healed cracks are thought to result from crystal growth in the healing cracks. During sample preparation, before the initial experiment, non-penetrative cracking in crystals causes a crystallographic misfit between the crackwalls. Crack healing would introduce many growth imperfections, like dislocations, in addition to fi.s (Fig.4.3), in order to restore the crystal. The high density of dislocations around fi.s (Fig.4.4A, 4.4B and 4.4D) within re-equilibrated quartz is proposed to be introduced through local deformation processes.

Brewster (1835, 1848 and 1861) already mentioned that the pressure exerted by fi.s strained the crystal. Carstens (1968) and Wilkins et al. (1992) noted clouds of dislocations around fi.s in natural quartz, which were assumed to form because of stress concentration. Stretching of fi.s was investigated by Larson et al. (1973), Bodnar & Bethke (1984) and Pécher (1984). The deformation mechanism associated with stretching was poorly understood and it was thought to be plastic flow related to movement of dislocations (Kirby & Green, 1980; Wanamaker & Evans, 1985 and 1989; Bouillier et al., 1989). Wanamakers & Evans (1989) showed a high dislocation density around an inclusion which has been annealed at 1400°C, they suggested that dislocations were produced on the inclusion surface in olivine and glide away from the inclusion. The dislocation microstructure in olivine (Wanamakers & Evans, 1989) and in natural quartz (Carstens, 1968) is identical to the observed microstructure around the synthetic inclusion in Fig.4.4D after the re-equilibration experiment. The similarity may imply that comparable deformation processes are operative in both natural quartz and experimentally treated quartz.

76

Planar defects in natural quartz were observed and visualized with TEM by McLaren & Phakey (1966 and 1969) and McLaren et al. (1967). The defects were related to Brazil and Daupiné twin boundaries, whose morphologies were described by Frondel (1962). Planar deformation features were often observed in quartz which is effected by shock metamorphism (Goltrant et al., 1991). They visualized planar defects with TEM as straight narrow bands parallel to the $\{10\bar{1}n\}$ planes. The fringe pattern in Fig.4.4F and 4.4G correspond to patterns described by McLaren & Phakey (1969) which diffraction contrast intensity relations were calculated to result from Dauphiné twin boundaries. The variable shape of the pattern, which is occasionally parallel to low-index planes, is also indicative for these twin boundaries (Frondel 1962). Dauphiné twins in Fig.4.4G are proposed to be primary, resulting from crystal growth in cracks during the initial experiment. Secondary Dauphine twinning, after crystal growth, may be produced by mechanical or thermal strain (Frondel, 1962). Dauphiné twins in Fig.4F are thought to result from local deformation (mechanical twinning) around fi.s, during re-equilibration.

4.5 DISCUSSION

We know from microthermometry and volume estimations (Bakker & Jansen, 1991b in **Chapter 3**) that the photographed re-equilibrated fi.s have leaked preferentially H_2O, which resulted in CO_2-richer fi.s with lower densities. Mimicking the setting of the experimentally healed crack in Fig.4.3, a quartz core with a healed crack is schematically illustrated in Fig.4.5, which is submitted to a hydrostatic pressure, different from the internal pressure. The healed crack (shaded area in Fig.4.5) has several growth dislocations and a synthetic inclusion with a CO_2-H_2O gas mixture. Activity gradients for H_2O and CO_2 exists between the fi.s and the pure H_2O fluid outside the quartz crystal. The activity of H_2O and CO_2 in fi.s with 20 mol% CO_2 and 200 MPa internal pressure during re-equilibration at 835 K are 0.85 and 0.29, respectively (Kerrick & Jacobs, 1981). Outside the crystal the

activity of H_2O and CO_2 are 1 and 0 for all re-equilibration experiments. These activity gradients would stimulate H_2O diffusion into the fi.s and CO_2 diffusion out of fi.s for both internal overpressurized and underpressurized fi.s. Our observations, including preferential leakage of H_2O and nearly constant CO_2 contents for both internal overpressurized fi.s and underpressurized fi.s (Bakker & Jansen, 1991b in **Chapter 3**), are not in accordance with the expected effects of this gradient. During all re-equilibration experiments (E463, E490), a pressure gradient exists between fi.s and the fluid outside the quartz crystal. Stress is concentrated in a rim around fi.s (Fig.4.5), due to both internal overpressure and underpressure. The crystal adjacent to the fi.s is strained by creep mechanism, expressed in the development of many dislocation. This deformation process will be highly effective in the healed crack (shaded area in Fig.4.5), where the quartz is softer (higher H_2O content) than the original Brazilian quartz.

The physical and chemical behaviour of H_2O in dislocation was suggested by Griggs & Blacic (1965) and Griggs (1974) to play an important role in hydrolytic weakening. Although the activation energy for pipe-diffusion was lower (Hirth & Lothe 1968), and the diffusion coefficient was higher (Yund et al. 1981) than those for bulk-diffusion, large diffusion lengths for pipe-diffusion were assumed to reduce the concentration gradient. However, calculations of Heggie & Jones (1987) and Heggie (1992) indicate that, theoretically, water was able to hydroxylate silicon-oxygen bonds in dislocations, and that H_2O molecules moved easily along dislocations without dissociation. Dislocations will spontaneously be saturated with water molecules if they are connected to fi.s which contain H_2O. The effect of H_2O diffusion along dislocations was clearly noticeable in single Brazilian quartz crystals with several inclusions synthesized during deformation experiments (S.W.J. den Brok, pers.comm., 1992). During an attempt to homogenize the pure H_2O inclusions, observable leakage occurred without decrepitation, before T_H was reached. Deformation of the Brazilian quartz must have resulted in a very high dislocation density around the fi.s, which provide many routes for leakage.

External hydrostatic pressure
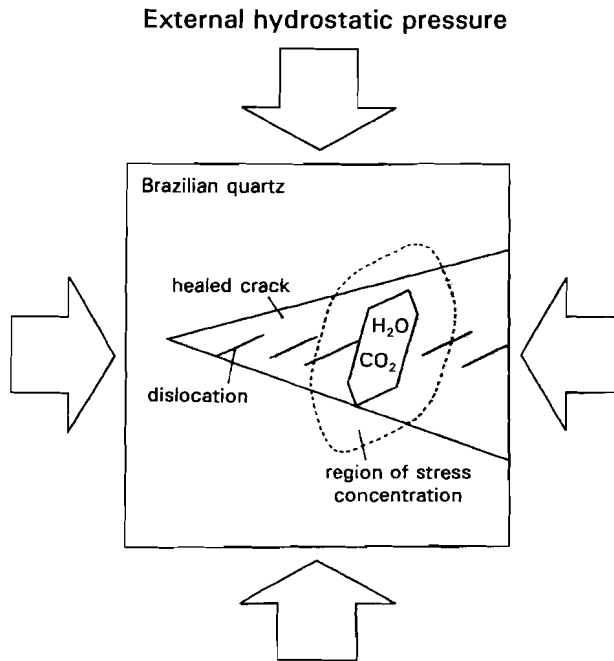
Figure 4.5.
A schematical sketch of a Brazilian quartz crystal with a healed crack
(shaded area), submitted to an external hydrostatic pressure (arrows).
The healed crack contains several dislocations and a fluid inclusion with a
gasmixture of CO_2 and H_2O. The area within the dashed line indicates the
region of stress concentration, which appears if the external pressure
differs from the pressure inside the inclusion during re-equilibration
experiments.

The physical and chemical behaviour of CO_2 in dislocation has never been a
subject of investigation. Belonoshko (1989) studied the properties of a CO_2-
H_2O mixture in a cylindrical pore of 0.8 to 2.5 nm diameter. According to his
adsorption calculations, the fluid in a pore of <2.5 nm diameter was H_2O
richer than the bulk fluid. Therefore, the dislocation core, which may be
considered as a small pore, was rich in H_2O. Intuitively, CO_2 molecules which
are about twice as large as H_2O molecules, are too large for effective CO_2
pipe-diffusion. The chemical interaction between quartz and CO_2 is negligible.

A crystal containing dislocations can always reach a lower energy state by getting rid of the dislocations, which is usually referred to as a process of recovery (Hirth & Lothe, 1968; Nicolas & Poirier, 1976). Hirth & Lothe (1968) defined an equation (eq.4.1) for the internal energy of a crystal associated with a defined length dislocation line.

$$E_{dislocation} \quad = \quad \frac{\mu b^2}{4\pi} \ln(\frac{R}{r_0}) \quad + \quad E_{core} \tag{4.1}$$

where μ is the shear modulus, b is the Burger's vector, R is the radius of the strain field around dislocations, r_0 is the radius of the dislocation core, and E_{core} is a factor for the core energy. As mentioned before, recovery process lowers the amount of energy in a crystal. The formation of small bubbles on dislocations is considered to be a mechanism to lower the internal energy of a strained crystal. The amount of energy which is needed for the formation of bubbles with variable diameter in quartz is defined by equation eq.4.2.

$$dE \quad = \quad \gamma dA \quad + \quad PdV \tag{4.2}$$

where dA is the amount of surface change ($4\pi r^2$ for a sphere), γ is the surface tension, dV is the amount of volume change, and P is the internal pressure. The internal pressure of the bubble accounts for a very small part of the energy, which is neglected in our calculations.

To verify the statement that bubble formation on dislocations is a recovery process, the energy of a dislocation with a selected length is compared to the energy of a bubble of a diameter which is equal to the selected length. Brace & Walsh (1962) and Parks (1984) estimated distinct values of surface tensions between quartz and water dependent on temperature, crystallography, and solutes in water. Holness et al. (1992) measured dihedral angles of quartz and a fluid of pure H_2O and a mixture of CO_2-H_2O to obtain surface tensions at different pressures. The dihedral angle decreases drastically above 600 MPa. Surface tensions varying between 0.3 and 0.7 Jm^{-2} are used in the calculations, which is approximately the range of estimated values between quartz and H_2O by Parks (1984).

80

	Wintsch & Dunning (1985)	Heggie & Nylén (1984)	Heinisch et al. (1975)
Shear Modulus (μ)	48.4 - 50.6 GPa	32 - 49 GPa	39.7 - 53.3 GPa (298 K) 36.5 - 44.6 GPa (773 K) 31.5 - 43.6 GPa (823 K)
Burger's Vector (b)	0.52 - 0.601 nm	0.4916 - 0.5406 nm	0.4913 - 0.7304 nm
Radius of dislocation core	0.52 - 0.601 nm	0.7389 nm	not included
Core Energy	$0.3\mu b^2$	$10^{-18.21}$ - $10^{-17.17}$ J/nm	

Table 4.1.

Shear modula, Burger's vectors, radii of dislocation core, and core energy described by Wintsch & Dunning (1985), Heggie & Nylén (1984) and Heinisch et al. (1975) required for the calculations of the energy of dislocations in a quartz crystal.

Table 4.1 reveals several selected shear modula, Burger's vectors, and radii of dislocation cores, which are used for our calculations. The shear modulus (μ) was derived from the elasticity theory, in which approximations were obtained by assuming isotropic linear behaviour of the crystal, or by using an average of the anisotropic shear modulus (Wintsch & Dunning, 1985). Heggie & Nylén (1984) used Keating potentials (Keating, 1966) to calculate the shear modulus. Poirier (1985) and Heinisch et al. (1975) indicated the temperature and pressure dependence of the shear modulus. The length of the Burger's vector was theoretically estimated, using the unit cell parameters of quartz, and must be larger than 0.264 nm, which was the minimum distance of oxygen atoms in quartz (Heggie & Nylén, 1984). Distinct types of dislocations had assorted Burger's vectors. The variation of these vectors with temperature and pressure were experimentally estimated by Hosieni et al. (1985). The variables R and r_0 were arbitrarily chosen, based on theoretical considerations of dislocations. In a crystal containing many dislocations, the average distance between the dislocations ($\overline{x}$ = $\sqrt{\rho}$, where ρ is the dislocation density) was an approximation of the radius R of the

strain field (Nicolas & Poirier 1976). Wintsch & Dunning (1985) assumed that equal amounts of dislocations were present with opposite sign, reducing the radius of the strain field to half the average distance between dislocations. They suggested the core energy to be larger than $0.3 \mu b^2$, which was measured for NaCl and metals. Heggie & Nylén (1984) defined core energies between $10^{-18.21}$ J/nm and $10^{-17.17}$ J/nm for distinct dislocations in quartz.

Calculated internal energy for dislocations is projected in Fig.4.6 to the energy of small bubbles with diameter similar to the length of the dislocation. The comparison of energy between a dislocation line and a small bubble is based on the assumption that a small bubble of diameter X replaces a dislocation line segment of length X. The model of Heggie & Nylén (1984), which considered energies for H_2O saturated dislocations ("wet disl." in Fig.4.6), indicate much lower energies than for dislocations without H_2O ("dry disl." in Fig.4.6) in the model of Wintsch & Dunning (1985). For the highest surface tension and the lowest H_2O saturated dislocation energy, bubbles of < 2 nm diameter are always energetically favourable. The maximum diameter of bubbles which are energetically favourable is 13 nm for the used parameters in Table 4.1. Therefore, formation of small bubbles at dislocation lines is a recovery process for strained crystals. The presence of small bubbles at dislocation lines observed after the re-equilibration experiments in Fig.4.4B, 4.4C, 4.4D, and 4.4G imply that this recovery process has been operating. However, the observed diameter of about 20 to 35 nm is not corresponding to the theoretically predicted diameter of maximally 13 nm. The decrease in surface tension at high PT conditions (Parks, 1984; Holness et al., 1992) indicate that the energy of equal sized bubbles is much lower at high temperatures and pressures than at low temperatures and pressures. The drop in energy for dislocations is less drastically than the energy drop for small bubbles. Therefore, the diameter of energetically favourable small bubbles is larger at high temperatures and pressures than 13 nm.

82
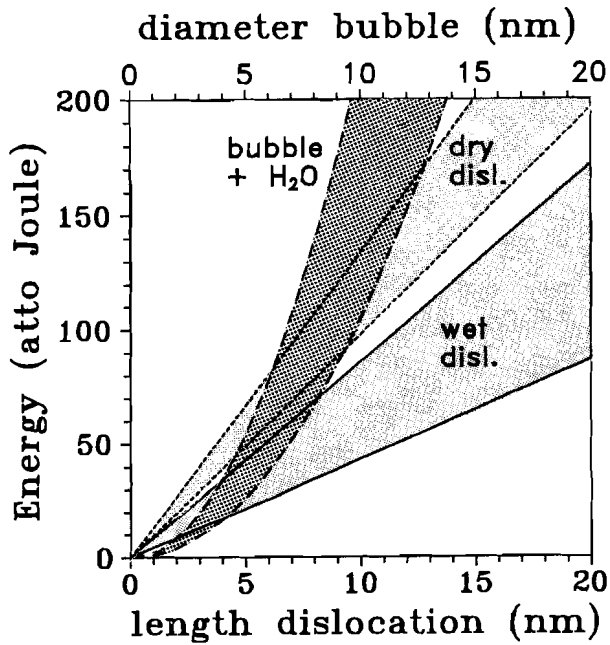
Figure 4.6.

Diagram of excess lattice energy versus length of dislocation or diameter of bubble at fixed temperature and pressure. Energy is expressed in atto-Joules (10^{-18}). The dark shaded area, bounded with large dashed lines and marked with "bubble + H_2O" is the surface energy of a bubble with a certain diameter according to Parks (1984). The upper and lower boundary are defined by surface tensions of 0.7 and 0.3 J/m_2, respectively. The light shaded area, bounded with short dashed lines and marked with "dry disl." is the energy for dislocation without water according the model of Wintsch & Dunning (1985). Heggie & Nylén (1984) reasoned much lower energies for H_2O saturated dislocations (light shaded area marked with "wet disl.").

McLaren et al. (1983) came forward with an argument for the observed diameters which are larger than 13 nm. Their small bubbles (10 to 100 nm diameter) in annealed synthetic quartz are thought to grow after the initial recovery process. McLaren et al. (1983) used the Laplace equation (eq.4.3 and Fig.4.7) to calculate the diameter of spherical bubbles in mechanical equilibrium at 0.1 MPa (P_{EXTERN}).

$$P_{BUBBLE} = P_{EXTERN} + \frac{4\gamma}{d} \tag{4.3}$$

where γ is the surface tension, r is the radius of the bubble, and P_{BUBBLE} is the pressure in the bubble. This equation indicates that the pressure in bubbles (P_{BUBBLE}) is always higher than the external pressure (P_{EXTERN}). McLaren et al. (1983) proposed that small bubbles grow through bulk-diffusion of $(4H)_{Si}$ defects into the small bubbles, and pipe-diffusion of silicon and oxygen through the simultaneously formed dislocations. The density of these pure H_2O small bubbles was suggested to be 0.8 g/cm^3. In re-equilibration experiments E463 and E490 at 835 K the internal pressure in similar small bubbles is 440 MPa (Fig.4.2) for both external pressures of 100 and 365 MPa, respectively. The Laplace-curve in Fig.4.7 (solid line) indicates the equilibrium overpressure in small bubbles with a variable diameter.

In re-equilibration experiment E463 and E490, the overpressure in the small bubbles are 340 MPa ("fi.1" in Fig.4.7) and 75 MPa ("fi.2" in Fig.4.7), respectively. After the recovery, a small bubble with a diameter of 13 nm may grow to a diameter of 20 nm in E463, and may shrink to a diameter of 11 nm in E490. The dashed lines in Fig.4.7 indicate the pressure drop and pressure rise in expanding and shrinking small bubbles, respectively, until mechanical equilibrium is reached at the Laplace-curve. Only small bubbles with an initial diameter of 20 nm ("big bubble" in Fig.4.7) in re-equilibration experiment E463 may reach the observed diameter of 35 nm. Because the initial diameter of small bubbles was argued to be maximally 13 nm, mechanical equilibrium between the pressure in small bubbles and the external pressure can not explain the occurrence of small bubbles with a diameter up to 35 nm, as observed in Fig.4.4B, 4.4C, 4.4D, and 4.4G.
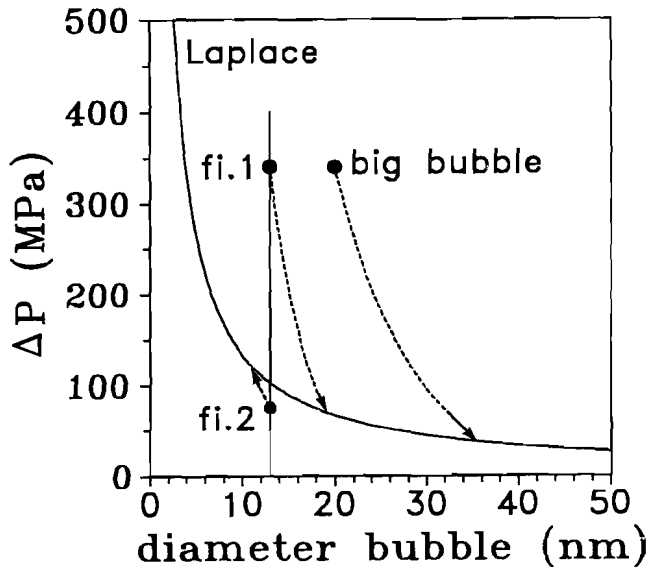
Figure 4.7.

ΔP versus bubble diameter diagram. ΔP is the difference between the
external hydrostatic pressure and the pressure inside bubbles. The solid
line indicates the overpressure in bubbles in quartz with a defined
diameter, which are in mechanical equilibrium (eq.4.3, Laplace). Bubbles
with a diameter of 13 nm will expand (fi.1) for a pressure difference of
340 MPa (E463), and will shrink (fi.2) for a pressure difference of 75
MPa (E490), until they reach equilibrium at the Laplace-curve. The dashed
lines for fi.1 and fi.2 indicate the decreasing and increasing pressure
difference during expansion and shrinkage, respectively. The "big bubble"
indicate the initial diameter of a bubble which has expanded to 35 nm of
diameter during E463.

The small bubbles on dislocations around a large synthetic inclusion in Fig.4.4D are proposed to be a preliminary stage in the development of an "implosion halo". The "implosion halos" observed by Sterner & Bodnar (1989) and Bakker & Jansen (1991b in Chapter 3) for synthetic fi.s with internal underpressures, consisted of many small bubbles which were optically visible. A solubility gradient within single crystals is proposed to be responsible for the growth of the initial small bubbles, formed during recovery, to larger bubbles, and to optically visible halos around underpressurized fi.s only after re-equilibration experiments. The effect of solubility gradients in single fi.s in salt was described by Lemmlein (1952), and caused migration of fi.s. The major controlling parameter is the solubility differences of the host mineral in a single inclusion, which may be caused by a thermal gradient. The solubility of quartz in H_2O is very sensitive to pressure (Anderson & Burnham 1965). Pressure differences in a single crystal may generate a solubility gradient. At 835 K, the solubility increases from about 0.5 wt% at 150 MPa to about 1 wt% at 300 MPa. In Fig.4.8 we have designed schematically a part of a quartz crystal which contains an inclusion, a dislocation, and a small bubble. The solubility in underpressurized fi.s during re-equilibration experiment E490 is lower than the solubility in the small bubble, which is positioned in higher pressure regions of the crystal (Fig.4.8). The quartz will preferentially dissolve in the small bubble, and precipitate in the inclusion. The dislocation line may act as a transport medium for the dissolved quartz and H_2O, and is inaccessible for CO_2. The original synthetic inclusion with a mixture of CO_2 and H_2O may shrink to a smaller CO_2-rich inclusion, and may have a halo of many small H_2O-rich bubbles.

Fi.s which are overpressurized (E463) have a reversed pressure gradient, and, therefore, a reversed solubility gradient. The small bubble will tend to shrink, and remain a small size which they initially obtained during recovery processes. Therefore, no "implosion halos" are observed after experiments with overpressurized fi.s.

fi

bubble

P_{IN}

dislocation

P_{EX}

low sol.   **high sol.**
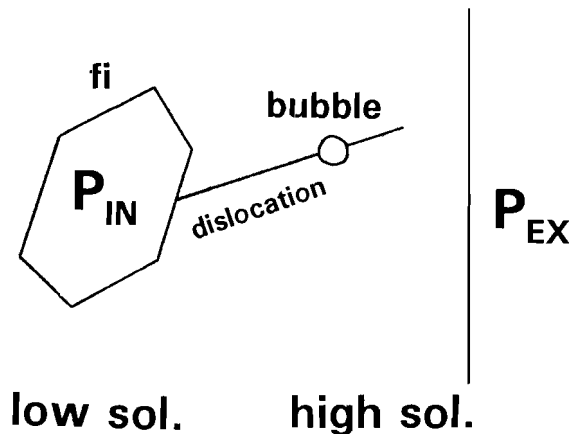
Figure 4.8.

*A schematical sketch of newly grown quartz within a healed crack, displaying a certain configuration of an inclusion (fi), a dislocation, and a small bubble. The solubility of quartz in H_2O in the bubble will be higher (**high sol.**) than the solubility in the inclusion (**low sol.**), if the external pressure outside the crystal (P_{EX}) is higher than the pressure in the inclusion (P_{IN}).*

4.6 VEIN QUARTZ FROM NAXOS

The natural vein quartz samples from Naxos are polycrystals, and display many deformation features, which are visible with an optical microscope. Electron micrographs of quartz adjacent to natural inclusions reveal a high defect densities (Fig.4.9), for example at subgrain-boundaries. The inclusions are often connected to dislocation networks. Several types of fi.s could be distinguished in natural quartz, in one single sample. Small negative β-quartz shaped fi.s, diameter 0.4 μm (Fig.4.9A) are arranged in a trail, and are mutually connected with dislocation, within a network. The negative β-crystal shape is well developed. The shape of the fi.s indicate that they were formed or recrystallized at temperatures above the transition temperature of α-quartz, which only occurred during the $M2_c$ re-equilibration (Fig.4.1).

(a)
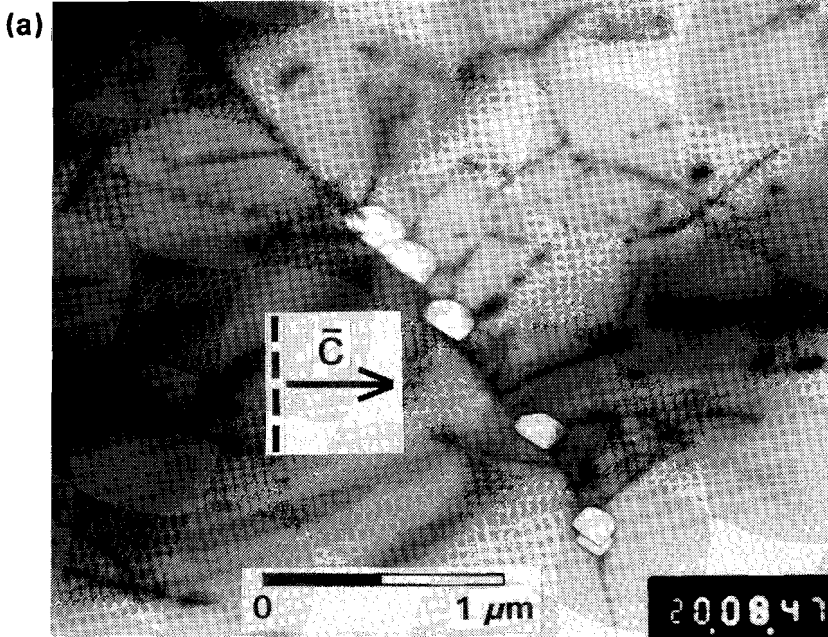
Figure 4.9.

Bright field electron micrograph (TEM) of vein quartz from Naxos. The orientation of the micrographs (see Appendix) is indicated with a short dashed line, which is an intersection of the basal plane with the photographic plane of projection. The arrows in (A), (B), and (C) are the crystallographic direction $\bar{c}$. The hexagon in (D) represents an intersection of prismatic planes m with the photographic plane of projection. (A) a trail of fi.s within a dislocation network. (B) a single inclusion connected to complex network of dislocations. (C) small bubbles at dislocations and isolated between dislocations. (D) a trail of irregular shaped inclusions with a high defect density between the inclusions in a naturally healed crack.

(b)

Figure 4.9. (Continued)

89

(c)

$\bar{C}$

0   ½ μm

(d)

0   1 μm

fi

fi

m

fi

fi

20.08.473

Figure 4.9. (Continued)

90
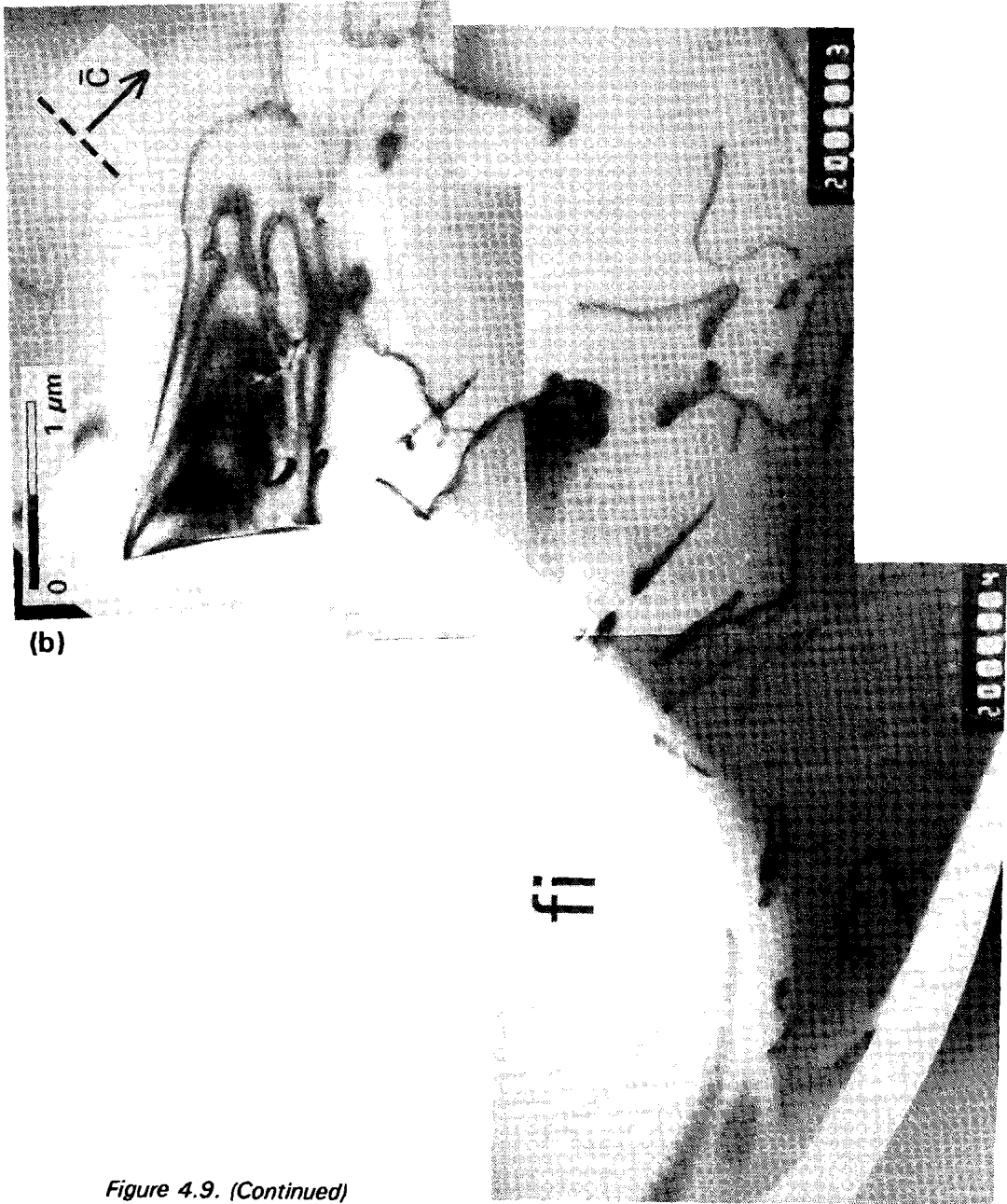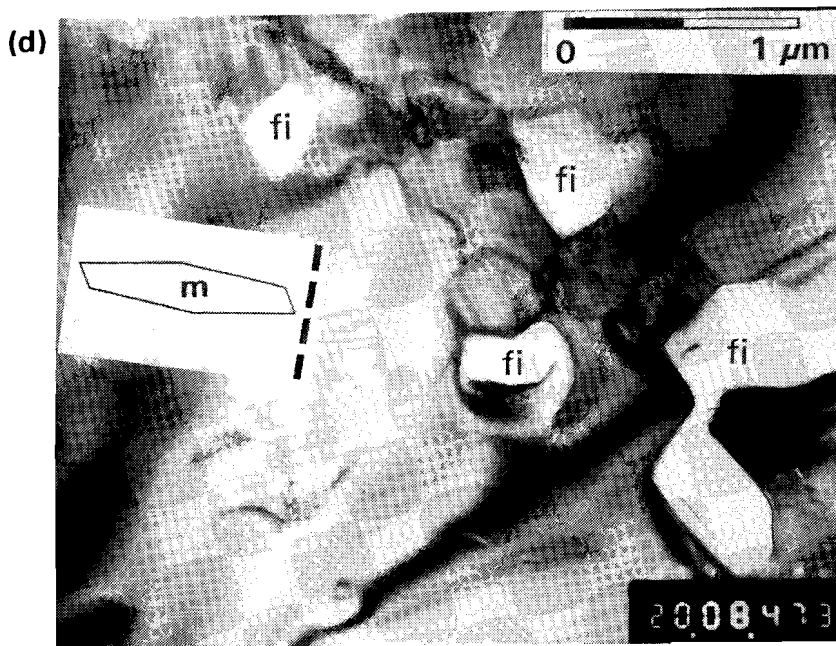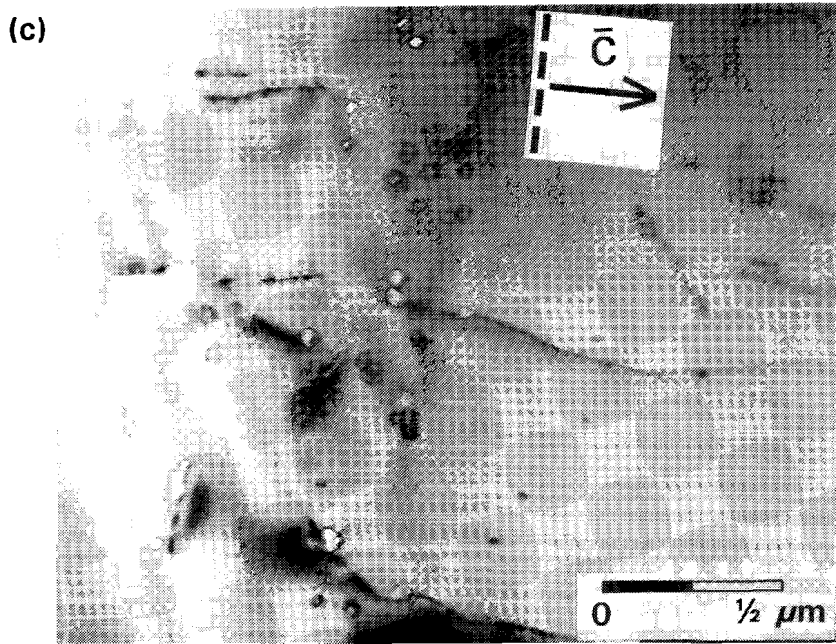
Large negative α-quartz shaped fi.s, diameter 4 μm (Fig.4.9B) are connected to complex dislocation networks. Dislocations occur as straight lines (some are parallel to $\overline{c}$) and curves. Several triple-junctions are present. In Fig.4.9C, several small fi.s of 30 nm diameter occur at dislocation lines, and occur isolated between dislocations. They have also well developed negative β-quartz crystal shapes. The dislocation density in these natural samples (Fig.4.9A, 4.9B and 4.9C) is much higher than the density in the experimentally healed cracks in Brazilian quartz (Fig.4.4). Routes for preferential H_2O leakage in deformed natural vein quartz are very abundant compared to the undeformed Brazilian quartz. The appearance of small bubbles on dislocation lines in natural samples (Fig.4.9C) is similar to the bubbles observed in Fig.4.4B, 4.4C and 4.4D, indicating that similar recovery processes may have occurred.

Between irregular shaped fi.s, maximal length 2 μm (Fig.4.9D) many dislocations are present. The shape is comparable to distinct synthetic fi.s, observed in experimentally healed cracks. These fi.s are assumed to be formed in a late stage. Fig.4.9D indicates that natural crack healing is similar to the mimicked crack healing in experiments, in which very irregular shaped fi.s occur in an early stage. Preservation of the irregular shape must have resulted from the absence of recrystallization after the crack healing process. The quartz further away from the inclusion trail have a lower density of defects, and represent the original crack wall. No planar crystal defects are observed in the natural samples.

4.7 CONCLUSIONS

The re-equilibrated CO_2-H_2O rich fi.s have leaked H_2O preferentially, resulting in relatively CO_2-richer fi.s (Bakker & Jansen, 1991b in chapter 3). The mechanism of non-decrepitative preferential H_2O leakage seems to be related to the occurrence of crystal defects.

The amount and variety of crystal defects near re-equilibrated fi.s, which have been overpressurized and underpressurized, is much higher compared to the initial synthesized fi.s during crack healing.

The presence of many small bubbles on dislocation lines around re-equilibrated fi.s must have resulted from recovery processes at high experimental temperatures.

Growth of small bubbles to optically visible "implosion halos" at the expense of the larger synthetic fi.s through selective diffusion of H_2O, silicon and oxygen along dislocations is proposed to account for preferential H_2O leakage from underpressurized fi.s. Diffusion of only H_2O along dislocations is thought to explain non-decrepitative preferential H_2O leakage from overpressurized fi.s.

Preferential H_2O leakage from natural fi.s must have been a highly active process in vein quartz from Naxos, because the quartz has a high dislocation density. The marked similarities with experimentally healed cracks indicate that comparable processes must have affected the natural fi.s.

92

Appendix

Orientation electron micrographs

The lattice type of quartz (Fig.4.10) is hexagonal. The crystal form is classified in the trigonal trapezohedral group. Due to the symmetry of quartz (Frondel, 1962) no distinction could be made between the $\overline{a}_1$, $\overline{a}_2$, and $\overline{a}_3$ axis. Consequently, no difference was made between 'a and a planes, between r and z planes, between 'l and l planes, and between 's and s planes.
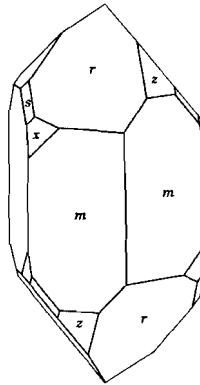
Figure 4.10

"Linksgewundenen" a-quartz crystal (after Frondel, 1962). The prism (m), positive and negative rhombohedra (r and z), trigonal pyramid (s), and the positive trigonal trapezohedron (x) are indicated.

The reciprocal lattice vector of common planes are projected in a Wulff net (Fig.4.11). The indices and the interplanar spacing (d) of these planes are given in Table 4.2. The orientation of Fig.4.3, 4.4, and 4.9 was obtained from diffraction patterns (Fig.4.12). These patterns were indexed with reference to the hexagonal unit cell of quartz in the stereographic projection (Fig.4.11).

93
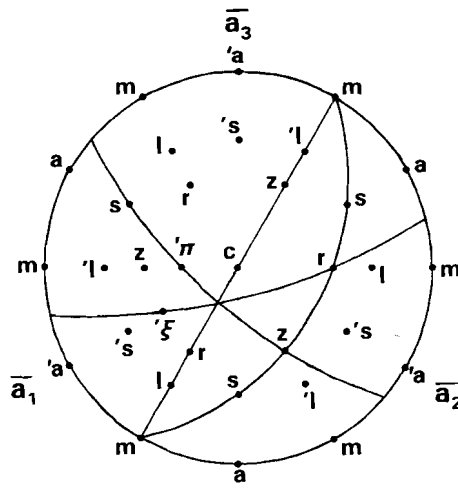
Figure 4.11
Stereographic projection in the Wulff net of quartz, showing common
planes (c, m, a, 'a, r, z, l, 'l, s, 's, 'π, and 'ξ) and the axes $\bar{a}_1$, $\bar{a}_2$, and $\bar{a}_3$.
Diffraction patterns are represented by great circles through reciprocal
lattice vectors (parallel to basal plane, through the m vectors in Fig.4.3;
through m, s, and r vectors in Fig.4.4A, 4C, and 4D; through r and 'ξ
vectors in Fig.4.4.F; through m, c, and r vectors in Fig.4.4.B, 4.9A, 9B,
and 9.C; through z and 'π vectors in Fig.4.9D).

plane	Miller-Bravais indices	d (nm)	plane	Miller-Bravais indices	d (nm)
c	0001	0.539365	l	$20\bar{2}1$	0.197968
m	$10\bar{1}0$	0.425505	'l	$02\bar{2}1$	0.197968
a	$11\bar{2}0$	0.245666	s	$11\bar{2}1$	0.223647
'a	$2\bar{1}\bar{1}0$	0.245666	's	$2\bar{1}\bar{1}1$	0.223647
r	$10\bar{1}1$	0.334331	'π	$01\bar{1}2$	0.228124
z	$01\bar{1}1$	0.334331	'ξ	$2\bar{1}\bar{1}2$	0.181781

Table 4.2
The Miller-Bravais indices and interplanar spacing (d) for crystallographic
planes indicated in Fig.4.11.

94

The zone axis of the diffracted planes is perpendicular to the orientation of the electron micrograph. The interplanar spacing (d) is obtained by measuring the distance (g) between two reciprocal lattice points in a row, and using the equation d = n/g, where n, which is dependend on the quartz crystallography and the used electron microscope, is approximately 1.8. The angle between two rows of reciprocal lattices is measured in the diffraction patterns (Fig.4.12). Electron micrographs are projected to diffraction patterns by rotation, which depends on the amount of magnification of an electron micrograph. For example, the diffraction pattern of Fig.4.4.D is projected in Fig.4.12. The sample is tilted a few degrees to obtain a two-beam condition, with the g vector of $(10\bar{1}0)$.
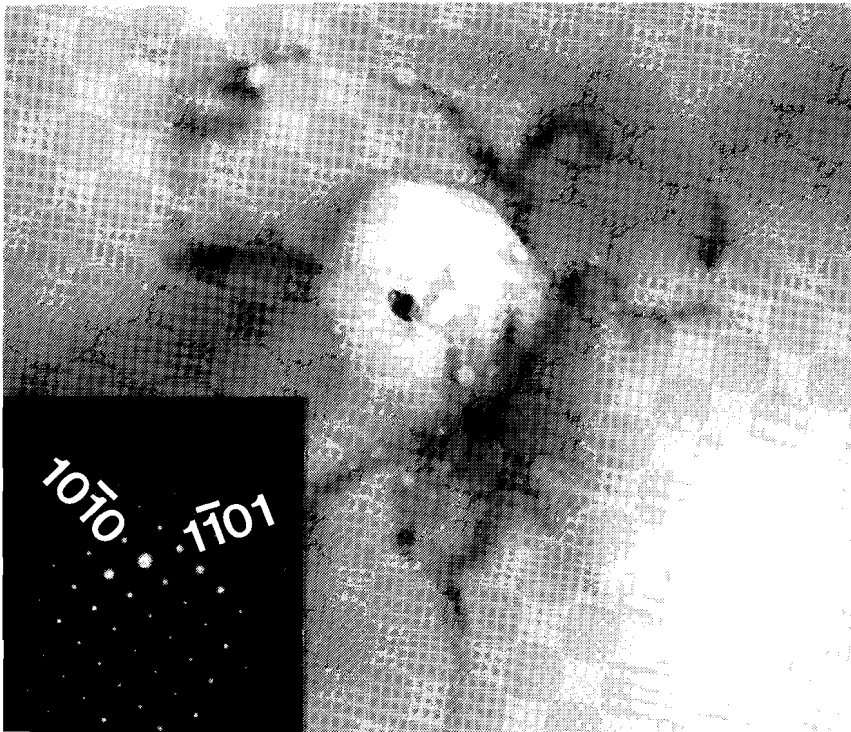
Figure 4.12
Electron micrograph (identical to Fig.4.4D) with projected diffraction pattern. The direction of m $(10\bar{1}0)$ and z $(1\bar{1}01)$ reciprocal lattice vectors are indicated. The angle between the rows is 66°.

Fig. 13.

96
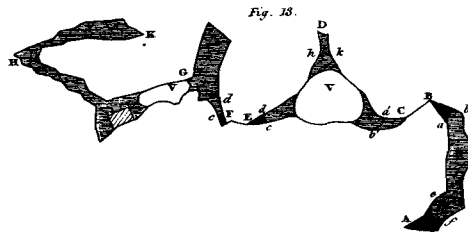
Chapter 5

THE PROGRAMS COHN: THEORETICAL BACKGROUND AND PROGRAM-STRUCTURE

5.1 INTRODUCTION

In order to calculate fluid compositions in rocks in the geological relevant gas-system COHN, a Pascal computer program has been developed. This program contains data from P-T-V-X relations of pure gases and gas mixtures, expressed in equations of state, molar volumes, isochoric systems and solvi. Additionally, heat capacity and molar volumes of minerals, which are used as buffers, are included in the program.

All physical and chemical interactions between molecules contribute to measurable properties, like pressure exerted by a gas and heat capacity, which characterise a calculated fluid in metamorphic rocks. However, due to the complexity of these interactions, no complete quantitative model has been proposed to predict observed properties. Most attemps die at the end in an emperical formulation within the measurable ranges of temperature and pressure. For example, you can drown in an ocean of emperical equations of state.

The theoretical background of the calculations and the design of the program are elucidated in this chapter.

5.2 THEORETICAL BASIS FOR THE PROGRAM

5.2.1 Statistical Thermodynamics

Measurable macroscopic properties (eg. volume, pressure, heat-capacity) are time averages over the very large number of possible quantum states (Hirschfelder et al., 1964; Prausnitz et al., 1986; Waldram 1991). The time average is the mean value (eq.5.1) for quantum states with a continuous range of possible values.

$$X = \sum_i p_i X_i \qquad (5.1)$$

where X, p_i and X_i are the macroscopic dynamic property, the probability of quantum state i and the value of this property which is in quantum state i, respectively. Applied to internal energy (E) of a system :

$$E = \sum_i p_i^* E_i \qquad (5.2)$$

where E_i is an approximate energy state, p_i^* is the most probable value that is equivalent to the average probability. In large systems, the mean spacing between energy states is extremely small. Therefore, the number of states per unit energy (density of states) is used for calculations. The density of states for a large system rises roughly exponentially with the number of possible quantum states, Stirling's approximation (derivation see Prausnitz et al., 1986; Waldram, 1991). All states having the same energy have the same probability, which is expressed as Boltzmann's distribution (eq.5.3).

$$p_i = \frac{e^{-\beta E_i(V\,N)}}{\sum_i e^{\beta E_i(V\,N)}} \qquad (5.3)$$

where V and N are the volume and the amount of particles, respectively. By definition, the value β is proportional to the reciprocal temperature (eq.5.4).

$$\beta = \frac{1}{kT} \tag{5.4}$$

The constant k is known as Boltzmann's constant ($1.3807*10^{-23}$ J/K). The summation term in the denominator is the partition function Q (eq.5.5), which is the sum over the states.

$$Q = \sum_i e^{-\beta E_i(V\,N)} \tag{5.5}$$

Substitution of eq.5.3 and 5.5 into eq.5.2:

$$E = \left(\frac{\partial lnQ}{\partial \beta}\right)_{VN} = kT^2\left(\frac{\partial lnQ}{\partial T}\right)_{VN} \tag{5.6}$$

To extract statistical analogues of thermodynamic functions, eq.5.2 must be differentiated (eq.5.7) to a formula corresponding to the first law in thermodynamics (eq.5.8).

$$dE = \sum_i E_i dp_i^* + \sum_i p_i^* dE_i \tag{5.7}$$

$$dE = TdS - PdV \tag{5.8}$$

Both terms in eq.5.7 are rewritten (derivation see Prausnitz et al., 1986) to eq.5.9 and 5.10, respectively.

$$\sum_i E_i dp_i^* = T\,d\left(-k\sum_i p_i^* lnp_i^*\right) \tag{5.9}$$

$$\sum_i p_i^* dE_i = \sum_i p_i^*\left(\frac{\partial E_i}{\partial V}\right)_N dV \tag{5.10}$$

Combination of eq.5.7, 5.8, 5.9 and 5.10 result in statistical analogues of entropy **S** (eq.5.11) and pressure **P** (eq.5.12).

$$S = k \, lnQ + (\frac{E}{T})$$ (5.11)

$$P = kT \, (\frac{\partial lnQ}{\partial V})_{TN}$$ (5.12)

To find a solution for the partition function **Q** it is convenient to examine seperately the energy contributions (eq.5.13) of various molecular degrees of freedom (micro systems).

$$Q = Q^{internal}(N,T) * Q^{kinetic}(N,T) * Q^{configuration}(N,T,V)$$ (5.13)

5.2.2 Pressure of gases

A relation between the pressure of an ideal monatomic gas and the velocity of the atoms (kinetic factor) is expressed in eq.5.14 (derivation see Waldram, 1991). In this equation, pressure depends only on the number of atoms present and not on any property of each atom itself. The partition function in eq.5.12 equals the volume **V** of an ideal gas, resulting in Boyle's law (Boyle, 1662) which is similar to eq.5.14.

$$PV = N_A kT$$ (5.14)

where N_A is Avogadro's number ($6.0220*10^{23}$ mol^{-1}). By definition, the gas constant **R** is $N_A k$ (8.31441 $JK^{-1}mol^{-1}$). The configurational factor, which add a non-ideal factor to the pressure of gases, depends on intermolecular forces, and is related to the potential energy between pairs of unlike molecules. The total potential energy (Γ_{total}) is the sum of the interactions $\Gamma_{ij}(r_{ij})$ of all possible pairs of molecules depending only on distance (Pitzer, 1939, eq.5.15).

100

$$\Gamma_{total} = \sum_{i<j} \Gamma_{ij}(r_{ij}) \qquad (5.15)$$

The forces between molecules are either repulsive or attractive (Mie, 1903; eq.5.16).

$$\Gamma_{total} = \Gamma_{repulsive} + \Gamma_{attractive} \qquad (5.16)$$

Types of attractive intermolecular forces are permanent electrostatic forces, induction forces, forces between non-polar molecules and chemical forces (Holloway, 1977; Prausnitz et al., 1986). Repulsive potential is not well understood. A semi-empirical model for potential energy is given by the Lennard-Jones 6-n potential (eq.5.17), in which n is an adjustable parameter (eg. n = 12).

$$\Gamma(r) = (\frac{n}{6})^{\frac{6}{n-6}} \frac{n}{n-6} \epsilon[(\frac{\sigma}{r})^n - (\frac{\sigma}{r})^6] \qquad (5.17)$$

where ϵ is the negative energy at equilibrium distance between the molecules, and σ is a distance equal to intermolecular seperation at zero potential energy. The configurational integral is expressed in eq.5.18.

$$Q^{conf.} = \int_V ... \int e^{-\frac{\Gamma_{total}(r_1...r_n)}{kT}} dr_1...dr_n \qquad (5.18)$$

where $\Gamma_{total}(r_1...r_n)$ is the total potential energy of the entire system of N molecules whose position are described by $r_1...r_n$. The configuration integral is expanded in terms of cluster integrals (Ursell, 1927), involving clusters of 1, 2, 3, ... N molecules (eq.5.19).

$$P = \frac{NkT}{V} * \{ 1 - \sum_{k=1}^{\infty} \frac{k\beta_k}{k+1}(\frac{N}{V})^k \} \qquad (5.19)$$

where β_k are various combinations of the cluster integrals (derivation see Hirschfelder et al., 1964; Waldram, 1991).

Many equations of state, which are mathematical relation between volume, pressure, temperature and composition, have been proposed, but

most of them are either totally or partially empirical. Van der Waals (1873) used molecule-displacement equations to obtain a pure theoretical relation between "den molekulairen druk" and "het volume". For the first time, the significance of critical pressure (P_c), temperature (T_c), and volume (V_c) was recognized by the shape of isotherms. Further studies concentrated on attractive forces between molecules (*a*) and the volume of molecules (*b*), which were incorporated in the equation.

In order to bring systematics in the many attemps to obtain *a*- and *b*-values, the virial equation (eq.5.20) was introduced by Kamerlingh-Onnes (1901). The equation, which was originally a best-fit attempt through data points, appeared to have a theoretical impact (compare with eq.5.19).

$$\frac{PV}{RT} = 1 + \frac{B(T)}{V} + \frac{C(T)}{V^2} + \frac{D(T)}{V^3} + \ldots \qquad (5.20)$$

The virial coefficients represent interactions involving two (**B**), three (**C**), four (**D**) etc. molecules, are directly expressible in terms of cluster integrals.

It was assumed that all gases have the same deviation from ideal behaviour at the same reduced pressure ($P_R = P/P_c$), reduced temperature ($T_R = T/T_c$), and reduced volume ($V_R = V/V_c$), which is used in the law of corresponding states (Pitzer, 1939). Therefore, critical values became inseparable from universal equations of state for individual gas species.

A semi-empirical equation of state, like the Redlich-Kwong equation (Redlich & Kwong, 1949, eq.5.21, 5.22. and 5.23) is a good reproduction of PTV relations in low PT ranges, above the critical point. This equation is an extended VanderWaals equation (van der Waals, 1873). Essentially, the assumption of constant *a* (eq.5.22) and *b* (eq.5.23), which is derived from critical values, is a worse approximation of the equation of state than the VanderWaals equation.

$$P = \frac{RT}{V-b} - \frac{a}{(V+b)V\sqrt{T}} \qquad (5.21)$$

102

$$a = \frac{0.4278 \; T_c^{5/2} R^2}{P_c} \qquad (5.22)$$

$$b = \frac{0.0867 \; T_c R}{P_c} \qquad (5.23)$$

Later, the temperature, pressure, and volume dependency of *a* and *b* was recognized, which leaded to modifications of the Redlich-Kwong equation. De Santis et al. (1974), Halbach & Chatterjee (1982) and Touret & Bottinga (1979) proposed several models for the value *a* and *b* which were emperically obtained. Holloway (1977) used constant values of *a* and *b* for CO, CO_2, CH_4, H_2, H_2O, H_2S, SO_2, N_2, NH_3 and O_2, and additionally temperature dependent *a* values for H_2O and CO_2 (de Santis et al., 1974, eq.5.24).

$$a(T) = a_0 + a_1(T) \qquad (5.24)$$

An example of a modified Redlich-Kwong equation (eq.5.25) is given by Kerrick & Jacobs (1981) and Jacobs & Kerrick (1981) for CO_2-H_2O-CH_4 mixtures. They included a repulsive factor which was modified by Carnahan & Starling (1972), by considering gas molecules to be rigid spheres.

$$P = \frac{RT (1 + y + y^2 - y^3)}{V (1 - y)^3} - \frac{a}{(V+b)V\sqrt{T}} \qquad (5.25)$$

where y = b/4V. The *a* term is empirically obtained in a power series in reciprocal volume V (eq.5.26).

$$a = c + \frac{d}{V} + \frac{e}{V^2} \qquad (5.26)$$

Similar to the VanderWaals equation, the virial equation has been frequently modified to virial-like equations of state (Saxena & Fei, 1987a and 1987b; Spycher & Reed, 1988; Belonoshko & Saxena, 1991a and 1991b; Duan et al., 1992a and 1992b). All equations are best-fit lines for data

obtained by direct PTV measurement (Saxena & Fei, 1987a; Spycher & Reed, 1988; Duan et al., 1992a and 1992b), by shock wave measurements (Saxena & Fei, 1987b), and by molecular dynamics simulations (Belonoshko & Saxena, 1991a and 1991b).

Saxena & Fei (1987a and 1987b) use besides a virial equation for H_2O, virial-like equation of state (eq.5.27) for pure Ar, Xe, N_2, O_2, CO, CO_2, CH_4, H_2 and H_2O which are valid in the PT range 10-1000 MPa and 400-1300 K.

$$\frac{PV}{RT} = A(T_R) + B(T_R)P_R + C(T_R)P_R^2 \qquad (5.27)$$

Belonoshko & Saxena (1991a, 1991b) calculated the virial coefficients for the pure supercritical fluids H_2O, CO_2, CH_4, CO, O_2 and H_2, which fit well experimental data at higher PT conditions. Their equation (eq.5.28) does not include an ideal gas component.

$$P = \frac{a(T)}{V} + \frac{b(T)}{V^2} + \frac{c(T)}{V^n} \qquad (5.28)$$

The virial-like equation of Duan et al.(1992a), which approach well the CO_2-H_2O-CH_4 system between 273-1273 K and 0-800 MPa, is a modification of the virial equation defined by Lee & Kessler (1975).

Christoforakis & Franck (1986) and Heilig & Franck (1989) develop an equation of state (eq.5.29, 5.30 and 5.31) based on a different model for potential energy, which describes and predicts the critical curve of binary mixtures (H_2O-CO_2, H_2O-CH_4, H_2O-N_2, H_2O-Xe). The repulsive factor (eq.5.31) is based on theoretical considerations of Carnahan & Starling (1972), and is similar to the repulsive term in eq.5.25.

$$P = P_{repulsive} + P_{attractive} \qquad (5.29)$$

$$P_{attractive} = -\frac{4RT}{V^2} \beta (\lambda^3 - 1)(e^{\frac{\epsilon}{kT}} - 1) \qquad (5.30)$$

$$P_{repulsive} = RT\frac{(V^3 + \beta V^2 + \beta^2 V - \beta^3)}{V(V - \beta)^3} \qquad (5.31)$$

where λ, ϵ, β are the relative wide of the square well, the depth of the square well, and a term related to the diameter of the spherical particles, respectively.

5.2.3 Heat capacity

The heat which is absorbed by one mole of substance per unit change of temperature can be measured at constant volume **V** (eq.5.32) or constant pressure **P** (eq.5.33).

$$c_V = (\frac{\partial E}{\partial T})_V = \frac{\partial}{\partial T} (kT^2 \frac{\partial lnQ}{\partial T}) \qquad (5.32)$$

$$c_P = (\frac{\partial H}{\partial T})_P = \frac{\partial}{\partial T} \{kT^2\frac{\partial lnQ}{\partial T} + kTV\frac{\partial lnQ}{\partial P}\} \qquad (5.33)$$

The relation between heat capacity at constant pressure and constant volume is:

$$c_P = c_V + T(\frac{\partial P}{\partial T})_V(\frac{\partial V}{\partial T})_P = c_V + \alpha^2 K_T VT \qquad (5.34)$$

where α is a temperature dependent coefficient of thermal expansion, K_T is the isothermal bulk modulus. The absorbed energy may be distributed among several factors in the partition function (eq.5.13). The atoms in ideal monatomic gases are assumed to behave like rigid bodies. Therefore, the heat capacity (eq.5.36) is derived from the translation energy of the atoms, the kinetic factor (eq.5.35).

$$Q^{kinetic} = V(\frac{2\pi mkT}{h^2})^{\frac{3}{2}N} \qquad (5.35)$$

$$c_V = \frac{3}{2}Nk \qquad c_P = \frac{5}{2}Nk \qquad (5.36)$$

where **N**, **m** and **h** are the amount of atoms, the mass of an atom, and Planck's constant ($6.62618 * 10^{-34}$ Js). Energy attributions from internal motions of gases causes deviation from the obtained values in eq.5.32-5.34. In diatomic gas the relative motion of the nuclei is vibration or rotation. The mean energy of a harmonic oscillator is expressed in Planck's formula (eq.5.37), in which all atoms have the same frequency *v*.

$$E^{vibration} = \frac{1}{2}h\nu + \frac{h\nu}{e^{\frac{h\nu}{kT}}-1} \qquad (5.37)$$

Heat capacity is obtained by substitution of eq.5.37 in eq.5.32. After partial differentiation, c_V approaches kT at high temperatures. The rotational energy is calculated by assuming the molecules to be rigid rotators (see Waldram, 1991).

Heat capacity of solids is partial defined by vibrational modes and their frequencies of atoms at fixed positions in a lattice (Waldram, 1991). Using a mean frequency (Einstein, 1907) the heat capacity c_V approaches 3Nk (Dulong and Petit's law) at high temperature. At low temperature, the Debye model (Debye, 1912) predicts more accurately the experimentally lattice heat capacity. However, heat capacities of silicates show large deviations from the behaviour expected from these considerations (Kieffer, 1979). Therefore, polynomial expressions, which are best-fit equations through experimentally obtained data, are proposed for minerals. Maier & Kelley (1932) used an emperical power function (eq.5.38), where *a*, *b* and *c* stand for temperature independent coefficients characteristic for each individual mineral.

106

$$c_P = a + bT + \frac{c}{T^2} \qquad (5.38)$$

Haas & Fisher (1976) used an extension of the Maier-Kelley equation for nonaqueous species (eq.5.39).

$$c_P = a + bT + cT^2 + \frac{d}{T} + e\sqrt{T} + fT^3 \qquad (5.39)$$

Helgeson et al.(1978) prefered the Maier-Kelley equation, while Robie et al. (1978) used the Haas-Fischer equation. Berman & Brown (1985) and Berman (1988) included, additional to the lattice factor (eq.5.40), a lambda-transition and a order-disorder heat capacity factor, to attempt extrapolations to higher temperatures.

$$c_P = k_0 + \frac{k_1}{\sqrt{T}} + \frac{k_2}{T^2} + \frac{k_3}{T^3} \qquad (5.40)$$

The lattice heat capacity is represented by the k_0-k_3 coefficients. For a phase with a lambda transition, a lambda factor (eq.5.41) is added at temperatures below the transition temperature T_λ.

$$c_P(\lambda) = (T+T_D) \{ l_1 + l_2(T+T_D) \}^2 \qquad (5.41)$$

where T_D is the temperature difference between the transition temperature at elevated pressures and 0.1 MPa. Berman & Brown (1985) and Berman (1988) demonstrated that the heat capacity of minerals can be reliably extrapolated to higher temperatures than available from calorimetric data. However, they did not include the high temperature limit of the Dulong and Petit's law. Fei & Saxena (1987) propose a polynomial expression for c_V (eq.5.42) which obbey this high temperature limit.

$$c_V = 3Rn \{1 + \frac{k_1}{T} + \frac{k_2}{T^2} + \frac{k_3}{T^3}\} \qquad (5.42)$$

where n and R are the number of atoms in the chemical formula, and the gas constant, respectively. C_P is obtained by adding an extra term (eq.5.43) to

eq.5.42, which is theoretically predicted in eq.5.34.

$$\alpha^2 K_T VT \equiv A + BT \qquad (5.43)$$

where **A** and **B** are empirically obtained constants. If atoms behave as anharmonic oscillators or cation disordening is present, an additional factor c_p' contributes to eq.5.42.

5.2.4 Mineral volumes

Minerals have different expansivities (*a*) and compressibilities (*B*), even within the same structural group, due to varied response to temperature and pressure of bond angles between polyhedra of different minerals. *a* and *B* may be predicted with the thermodynamic relationship eq.5.34 (Saxena, 1989b). To characterize mineral volume over several PT condition, the total differential of volume **V** (eq.5.44) is formulated in thermal expansion (eq.5.45) and in compressibility (eq.5.46).

$$dV = (\frac{\partial V}{\partial T})_P \, dT + (\frac{\partial V}{\partial P})_T \, dP \qquad (5.44)$$

$$\alpha = \frac{1}{V}(\frac{\partial V}{\partial T})_P \qquad (5.45)$$

$$B = \frac{1}{K_T} = -\frac{1}{V}(\frac{\partial V}{\partial P})_T \qquad (5.46)$$

where K_T is the bulk modulus, similar in eq.5.34. According to eq.5.45 and 5.46, both *a* and *B* are dependent on temperature and pressure. Usually, a bestfit line is constructed through data points either at constant pressure (eq.5.47 and 5.48) or constant temperature (eq.5.49).

$$\alpha(T) = \alpha_0 + \alpha_1 T + \frac{\alpha_2}{T^2} + \frac{\alpha_3}{T^3} \qquad (5.47)$$

$$K_T = K_0 + K_1 T + K_2 T^2 + K_3 T^3 \qquad (5.48)$$

$$B = B_0 + B_1 P + B_2 P^2 \qquad (5.49)$$

A precise method to calculate the molar volume of minerals at fixed PT conditions is directly from the volume of an unit cell as calculated from X-ray data (eg. Hosieni et al., 1985). Berman (1988) used a pure empirical equation for mineral volumes (eq.5.50), which has no theoretical basis and is restricted to P < 1 GPa.

$$\frac{V}{V_0} = 1 + v_1(P-P_{rf}) + v_2(P-P_{rf})^2 + v_3(T-T_{rf}) + v_4(T-T_{rf})^2 \qquad (5.50)$$

where V_0 is molar volume at reference pressure P_{rf} and reference temperature T_{rf}. Fei & Saxena (1987) used the Murnaghan equation (eq.5.51) to calculated molar volumes of minerals.

$$V = V_0 * \left\{ 1 + \int_{298}^{T} \alpha(T) dT \right\} * \left(1 + \frac{K_0'}{K_0} P \right)^{-\frac{1}{K_0'}} \qquad (5.51)$$

where K_0 and K_0' are the bulk modulus and it's pressure derivative, respectively.

5.2.5 Fundamental equations

The enthalpy H, entropy S and Gibbs energy G depend on pressure and temperature. Their change is independent of the path chosen to effect that change. Therefore, the total differentials are :

$$dH = \left(\frac{\partial H}{\partial T}\right)_P dT + \left(\frac{\partial H}{\partial P}\right)_T dP \qquad (5.52)$$

$$dS = \left(\frac{\partial S}{\partial T}\right)_P dT + \left(\frac{\partial S}{\partial P}\right)_T dP \qquad (5.53)$$

$$dG = \left(\frac{\partial G}{\partial T}\right)_P dT + \left(\frac{\partial G}{\partial P}\right)_T dP \qquad (5.54)$$

Fundamental relationships of thermodynamics, summarized by Nordstrom & Munoz (1985), are shown in eq.5.55, 5.56 and 5.57.

$$G = H - TS \qquad (5.55)$$

$$dG = dH - TdS - SdT \qquad (5.56)$$

$$dG = VdP - SdT \qquad (5.57)$$

Gibbs Energy of substances can be obtained from the enthalpy and the entropy at constant temperature and pressure. The thermodynamical data, which is needed to solve these equations is obtained from calometry and volume measurements. Heat capacity measurements at constant pressure provide a means to calculate enthalpy (eq.5.58 and 5.59) and entropy (eq.5.60 and 5.61).

$$C_P = \left(\frac{\partial H}{\partial T}\right)_P \qquad (5.58)$$

$$\int dH = \int C_P \, dT \qquad (5.59)$$

$$dS = \frac{dQ}{T} \qquad (5.60)$$

$$\int dS \ = \ \int \frac{C_p}{T} \ dT \qquad\qquad (5.61)$$

Eq.5.62 and 5.63 include pressure effects on entropy and enthalpy at constant temperature, derived from volume estimations.

$$dH \ = \ c_p \, dT \ + \ \{ T \, (\frac{\partial V}{\partial T})_p \ + \ V \} \, dP \qquad (5.62)$$

$$dS \ = \ \frac{c_p}{T} \, dT \ - \ (\frac{\partial V}{\partial T})_p \, dP \qquad\qquad (5.63)$$

5.2.6 Phases

A phase, like a solid, a liquid or a vapour, may be composed of many components. Each phase may be a solution of many end members. Eq.5.54 is extended with partial molal Gibbs energies (eq.5.64) for individual components (n_i) in solutions (Gibbs, 1876).

$$dG \ = \ (\frac{\partial G}{\partial T})_{P \, n_i} \, dT \ + \ (\frac{\partial G}{\partial P})_{T \, n_i} \, dP \ + \ \sum_i (\frac{\partial G}{\partial n_i})_{T \, P \, n_j} \, dn_i \qquad (5.64)$$

The chemical potential (μ_i) is the partial molal Gibbs energy ($\partial G/\partial n_i$). Similar equations to eq.5.54 are defined for the chemical potentials (eq.5.65).

$$d\mu_i \ = \ (\frac{\partial \mu_i}{\partial T})_P \, dT \ + \ (\frac{\partial \mu_i}{\partial P})_T \, dP \qquad\qquad (5.65)$$

Partial volume V_i of gases in a mixture (eq.5.66) and the partial entropy S_i (eq.5.67) are deduced from fundamental relations in thermodynamics (eq.5.54 and 5.57).

$$\left(\frac{\partial \mu_i}{\partial P}\right)_T = V_i \qquad \qquad (5.66)$$

$$\left(\frac{\partial \mu_i}{\partial T}\right)_P = -S_i \qquad \qquad (5.67)$$

A solution for eq.5.66 is obtained by introducing the concepts fugacity (f_i) and activity (a_i), which are defined by eq.5.68 and eq.5.69, respectively (derivation see Prausnitz et al., 1986).

$$\ln\frac{f}{P} = -\frac{1}{RT} \int_0^P \left(\frac{RT}{P} - \overline{V}\right) dP \qquad \qquad (5.68)$$

$$a_i \equiv \frac{f_i}{f_i^0} \qquad \qquad (5.69)$$

where f_i^0 is the fugacity of species i at the reference pressure P_0. The activity of pure components, which take part in the reactions, are equal to 1. The fugacity coefficient (γ_i) is defined by eq.5.70.

$$\gamma_i = \frac{f_i}{P_i} \qquad \qquad (5.70)$$

The fugacity coefficient is calculated with molar volumes of real gases which are described in the virial equation of state (eq.5.20, 5.27, and 5.28) or the modified Redlich-Kwong equation of state (eq.5.21, 5.25, and 29). The relation between activity and chemical potential (eq.5.71) is obtained by substitution of eq.5.68 and eq.5.69 in eq.5.66.

$$\mu_i = \mu_i^0 + RT \ln a_i \qquad \qquad (5.71)$$

where μ_i^0 is the chemical potential of the pure gas i at the reference pressure P_0, usually 0.1 MPa.

In our calculations we regard buffer minerals and graphite as pure substances (pure phases), and the buffered fluid a solution of H_2, N_2, O_2,

112

CH_4, CO, CO_2, H_2O, NH_3 and NO_2. Raoult (1888) described an ideal solution for gases, in which the vapour pressure of individual gases (p_i) depends on their mole fractions X_i (eq.5.72).

$$P_{total} = \sum_i p_i = \sum_i X_i \, P_{total} \qquad (5.72)$$

Ideal mixing of real gases (Lewis-Randal rule) was used by Eugster & Skippen (1967) to calculate the fugacity of all gas species at metamorphic conditions. However, at high pressures and temperatures non-ideal behaviour prevail in the gas phase. Berthelot (1879) proposed a non-ideal mixing rule for the attractive forces between different molecules (eq.5.73), value *a* in eq.5.22. Ideal mixing (eq.5.74) is assumed for the co-volume of molecules, value *b* in eq.5.23.

$$a_{mixture} = \sum_i \sum_j X_i \, X_j \, a_{ij} \qquad (5.73)$$

$$b_{mixture} = \sum_i X_i \, b_i \qquad (5.74)$$

The cross coefficient ($i \neq j$) is arbitrarily a geometric mean (eq.5.75).

$$a_{ij} = \sqrt{a_i \, a_j} \qquad (5.75)$$

De Santis et al.(1974) propose physically reasonable mixing rules for mixtures of H_2O and nonpolar gases, which are expressed in the cross coefficient. Holloway (1977), Flowers (1979) and Jacobs & Kerrick (1981) used these mixing rules to calculate the composition of metamorphic fluids. Mixing rules for the virial coefficients B (eq.5.76) and C (eq.5.77) in eq.5.20 give a complete description of interactions between different molecules (Prausnitz et al., 1986).

$$B_{mixture} = \sum_{i=1}^{m} \sum_{j=1}^{m} X_i \, X_j \, B_{ij} \qquad (5.76)$$

$$C_{mixture} = \sum_{i=1}^{m} \sum_{j=1}^{m} \sum_{k=1}^{m} X_i \, X_j \, X_k \, C_{ijk} \qquad (5.77)$$

Alas, the values for B_{ij} and C_{ijk} are not yet defined in literature. Spycher &

Reed (1988) and Duan et al. (1992b) performed the first attempts to determine emperically these values for mixtures of CO_2-H_2O-CH_4.

5.2.7 Equilibria

The basic assumption for equilibrium is reversibility of processes in a closed system with no energy or mass transfer with the surroundings (Nordstrom & Munoz, 1985). A reaction may occur between different phases or between different components in a phase. Relations between phases are extensively described by Oonk (1981). Products and reactants of a chemical reaction are in equilibrium when $\Delta G_{reaction} = 0$, at constant pressure and temperature (eq.5.78).

$$\Delta G_{reaction} = \sum_i \nu_i \, \mu_i = 0 \qquad (5.78)$$

where ν_i is the stoichiometric value of reactant and product i. The fundamental relation in eq.5.55 is replaced by eq.5.79 for a reaction.

$$\Delta G = \Delta H - T\Delta S \qquad (5.79)$$

Substitution of eq.5.65 for each participant of the reaction into eq.5.78 results in :

$$\Delta \mu_i = \Delta \mu_i(0.1 MPa, \ 298K) \ + \ \int_{298}^{T} \Delta S_i \ dT \ + \ \int_{0.1}^{P} \Delta V_i \ dP = 0 \quad (5.80)$$

The last term in eq.5.71 replaces the volume integral in eq.5.80 :

$$\int_{0.1}^{P} \Delta V_i dP = \sum_i \nu_i \ (\int_{0.1}^{P} V_i dP) = RT \ \ln \Pi_i \ a_i^{\nu_i} \qquad (5.81)$$

By definition, the equilibrium constant K_{eq} (eq.5.82) is the product of activities in eq.5.81.

114

$$K_{eq} = \Pi_i \, a_i^{v_i} \qquad\qquad (5.82)$$

To calculate equilibrium constant for complex mineral and gas reactions, the reaction is split into several elementary reaction for each component.

5.3 THE COHN PROGRAMS

French (1966) and Eugster & Skippen (1967) calculated gas fugacities in the C-O-H and C-O-H-S system in rocks, with a combination of gas equilibria involving several independent reactions (Table 5.1) and the sum of all gas pressures (eq.5.72). Equilibrium constants for the gas species were calculated with eq.5.82. According to the phase-rule, the presence of graphite in a C-O system defines all fugacities (CO, CO_2, and O_2) at defined P-T conditions, and no extra mineral buffer is needed. In the O-H system, a buffer (Table 5.1) is needed to define all gas species (H_2, H_2O, and O_2). Likewise, if graphite is present in the C-O-H system, which has 3 components and 2 phases (solid graphite and a fluid), a mineral assemblage must buffer one of the gas species (H_2, O_2, CH_4, CO, CO_2, or H_2O) to define all gas fugacities. The graphite and the solid participants in the buffer are assumed to be pure. Within systems with four components in equilibrium with graphite (eg. C-O-H-S or C-O-H-N) two distinct buffers have to be used to define all gas fugacities. The presence of the buffering mineral assemblage and graphite in metamorphic rocks would specify the fluid phase for a wide range of geological possible conditions.

To calculated isopleths or iso-fugacities in the C-O-H-N gas system (H_2, N_2, O_2, CH_4, CO, CO_2, H_2O, NH_3, NO_2) at any relevant P-T conditions, a computer program (**CURVES**) has been written in Pascal. The program **CURVES** is based on the method described by French (1966) and Eugster & Skippen (1967). We have selected several mineral assemblages to buffer O_2, N_2, H_2O, and NH_3 (Table 5.1).

Table 5.1
Reactions for gas equilibria, oxygen buffers, nitrogen buffers, water buffers, and ammonium buffers. The abbreviations of the buffers are given between brackets.

Nitrogen Buffers	$2CrN \rightleftharpoons 2Cr + N_2$	(CCN)
	$2TiN \rightleftharpoons 2Ti + N_2$	(TTN)
Water Buffers	$KMg_3(AlSi_3)O_{10}(OH)_2 + 3SiO_2 \rightleftharpoons 3MgSiO_3 + KAlSi_3O_8 + H_2O$	(PQEK)
	$KAl_2(AlSi_3)O_{10}(OH)_2 + SiO_2 \rightleftharpoons Al_2SiO_5 + KAlSi_3O_8 + H_2O$	(MQAK)
	$Ca_2Mg_5Si_8O_{22}(OH)_2 \rightleftharpoons 2CaMgSi_2O_6 + 3MgSiO_3 + SiO_2 + H_2O$	(TDEQ)
Ammonium Buffers	$2NH_4Si_3AlO_8(\frac{1}{2}H_2O) \rightleftharpoons Al_2SiO_5 + 5SiO_2 + 2NH_3 + 3H_2O$	(BAQ)
	$6NH_4Si_3AlO_8(\frac{1}{2}H_2O) \rightleftharpoons 2NH_4Al_2Si_3AlO_{10}(OH)_2 + 12SiO_2 + 4NH_3 + 2H_2O$	(BTQ)

Gas Equilibria	$C + \frac{1}{2}O_2 \rightleftharpoons CO$	
	$C + O_2 \rightleftharpoons CO_2$	
	$C + 2H_2 \rightleftharpoons CH_4$	
	$H_2 + \frac{1}{2}O_2 \rightleftharpoons H_2O$	
	$\frac{1}{2}N_2 + \frac{3}{2}H_2 \rightleftharpoons NH_3$	
	$\frac{1}{2}N_2 + O_2 \rightleftharpoons NO_2$	
Oxygen Buffers	$6Fe_2O_3 \rightleftharpoons 4Fe_3O_4 + O_2$	(HM)
.	$2Fe_3O_4 + 3SiO_2 \rightleftharpoons 3Fe_2SiO_4 + O_2$	(QFM)
	$Fe_2SiO_4 \rightleftharpoons SiO_2 + 2Fe + O_2$	(QFI)
	$\frac{2X}{4X-3}Fe_3O_4 \rightleftharpoons \frac{6}{4X-3}Fe_xO + O_2$	(WM)
	$2Fe_xO \rightleftharpoons 2X\,Fe + O_2$	(WI)
	$\frac{1}{2}Fe_3O_4 \rightleftharpoons \frac{3}{2}Fe + O_2$	(MI)
	$2NiO \rightleftharpoons 2Ni + O_2$	(NNO)
	$6SiO_2 + 2Fe_3O_4 \rightleftharpoons 6FeSiO_3 + O_2$	(QMP)

Table 5.1 (Continued)

The program **FLEVOL** is able to calculate the fluid development in rocks, which have passed throught a specific P-T path defined by the mineral assemblages. The stabillity of observed natural fluids in metamorphic rock may be inspected.

Additionally, the program **MIAT** calculates densities with measured homogenization temperatures for natural fi.s with a known composition. Homogenization temperatures of theoretically calculated fluids in inclusions are predicted. Thermodynamical data, like heat capacity, entropy or enthalpy can be calculated for minerals and gases at any P-T condition.

Each program uses several units which include specific subjects, described in section 5.2.

5.3.1 Units

The unit **GRAPHTESTER** uses the procedure "*Initgraph*" to identify the graphics hardware of the computer, initializes the appropriate graphics drivers, and put the system into the graphics mode. The procedure "*DetectGraph*" determines which graphics driver and mode is used. If no graphics driver and mode are detected, the program will be aborted.

The unit **LAYOUT** provides the layout in the graphics mode, which is used for the input through the keyboard. The procedure "*Kader*" draws a framework at the edges of the screen, and indicates how to use the keyboard to choose a requested number and word during input routines. The procedure "*Clean*" is able to clean the screen or parts of the screen. An appropriate choice out of a set, defined in the programs, is made in the function "*BlokChoice*". The function "*Reading*" is used to read numbers and words through the keyboard. Both words and numbers are read as strings. The numbers are converted to reals. Procedure "*File-Info*" organizes the data representation for many types of diagrams, which are described in section 5.3.2.

Variables, constants, types and procedures which are accesible for all units and programs are defined in the unit **CENTRAL**. The elements, gases ,

118

minerals and their phases are defined as types (Table 5.2). The procedure "*Control*" displays a calculated value (integer, real or extended real) on the screen at a defined position (X,Y). The procedure "*Defect*" aborts the program when limits are exceeded or when the solution of calcultions is non realistic. The procedure "*Nul*" apoints the value 0 to all proporties of elements, gases, minerals, and phases. The procedure "*VirialNul*" and "*VirialSym*" apoints the value 0 to each virial-coefficient, and equalises the virial-coefficients with corresponding subscripts, respectively. The procedure "*Fuga-Mole*" calculates for each gas species the fugacity and mole fraction with a known fugacity of O_2, H_2, N_2, and a known activity of carbon.

All thermodynamical data are stored in the unit **THERMOD**. Heat capacity coefficients, entropy at a reference temperature (S_{ref}), and enthalpy difference between 298 K and a reference temperature (HT_{ref}-H_{298}) for each element, gas, and mineral are displayed in a 2 dimensional array of constants. The format of the array is : k_0, k_1, k_2, k_3, l_1, l_2, l_3, T_{ref}, T_{top}, S_{ref}, HT_{ref}-H_{298}, where k_0-k_3 and l_1-l_3 are the coefficients for heat capacity defined by eq.5.83 (combination of eq.5.40 and 5.41).

$$c_P \;=\; k_0 \;+\; \frac{k_1}{\sqrt{T}} \;+\; \frac{k_2}{T^2} \;+\; \frac{k_3}{T^3} \;+\; l_1 T \;+\; l_2 T^2 \;+\; l_3 T^3 \qquad\qquad (5.83)$$

The heat capacity coefficients are valid between the lower (T_{ref}) and upper temperature boundaries (T_{top}). Procedure "*PhaseChange*" compares a given temperature to transition temperatures of certain minerals (eg. iron, quartz, hematite, and magnetite), and select the proper heat capacity coefficients for each phase (Table 5.2). The molar volume of minerals is divided into several procedures. Procedure "*ConstantVolume*" gives constant values for element and mineral molar volumes (Robie et al., 1978), which do not vary with temperature and pressure. Procedure "*VolumeBerman*" uses eq.5.50 (Berman, 1988) to calculate molar volumes as function of temperature and pressure, up to 1 GPa.

Gases	Hydrogen (*H2*)	Nitrogen (*N2*)	Oxygen (*O2*)
	Methane (*CH4*)	Carbon monoxide (*CO*)	Carbon dioxide (*CO2*)
	Water (*H2O*)	Ammonium (*NH3*)	Nitrogen dioxide (*NO2*)
Elements	Aluminium (*Al, Al_liq*)		
	Carbon (*C_gr*)		
	Calcium (*Ca, Ca_b, Ca_liq, Ca_vap*)		
	Chromium (*Cr, Cr_a2, Cr_liq*)		
	Iron (*Fe, Fe_a2, Fe_a3, Fe_a4, Fe_a5, Fe_c, Fe_d, Fe_liq*)		
	Potassium (*K, K_liq, K_vap*)		
	Magnesium (*Mg, Mg_liq, Mg_vap*)		
	Sodium (*Na, Na_liq, Na_vap*)		
	Nickel (*Ni, Ni_a2, Ni_a3, Ni_a4, Ni_a5, Ni_a6, Ni_liq*)		
	Silicon (*Si, Si_liq*)		
	Titanium (*Ti, Ti_b*)		
Minerals	Corundum (*cor*)	Andalusite (*and*)	Kyanite (*ky*)
	Sillimanite (*sil*)	Kaolinite (*kao*)	Pyrophyllite (*pph*)
	Tremolite (*trm*)	Diopside (*dps*)	Carlsbergite (*CrN*)
	Dichromium nitride (*Cr2N*)	Iron oxide (*FeO, FeO_d*)	Wustite (*wus*)
	Hematite (*hem*)	Magnetite (*mag*)	Ferrosilite (*fsil*)
	Fayalite (*fay*)	Ilmenite (*ilm*)	Titanomagnetite (*tmag*)
	Dipotasium monoxide (*K2O*)	Microcline (*mic*)	Sanidine (*san*)
	Muscovite (*mus*)	Phlogopite (*phl*)	Spinel (*spl*)
	Geikelite (*gel*)	Cordierite (*cdt*)	Pyrope (*pyr*)
	Periclase (*per*)	Clino-enstatite (*en_c*)	Ortho-enstatite (*en_o*)
	Forsterite (*fo*)	Talc (*ta*)	Anthophyllite (*aph*)
	Disodium monoxide (*Na2O*)	Jadeite (*jad*)	low Albite (*al_l*)
	high Albite (*al_h*)	Paragonite (*par*)	Bunsenite (*bun, bun_b, bun_c, bun_c1, bun_c2*)
	Quartz (*qtz*)	Rutile (*rut*)	
	Titanium nitride (*TiN*)	Osbornite (*osb*)	Anatase (*ana*)

Table 5.2
List of elements, gases, and minerals which are included in the C-O-H-N programs. The abbreviations of the phases are mentioned between brackets.

Procedure "*VolumeFeiSaxena*" uses the Murnaghan equation (eq.5.51, Fei & Saxena, 1987) to calculate several molar volumes in the system Fe-Mg-Si-O at elevated temperarues and pressures. Procedure "*VolumeHosieni*" calculates the molar volume of α-quartz and β-quartz (Hosieni et al., 1985) up to 1900 K and 4000 MPa. The heat capacity and molar volume of minerals and gases at high temperatures and pressures are both used in the procedures "*SpecificHeat*", "*Entropy*", and "*Enthalpy*" to calculate the heat capacity (c_p), entropy (S), and enthalpy difference (dH), respectively. The procedure "*Reaction*" calculates the activity quotient (eq.5.82) for a chosen stoichiometric reaction. Eq.5.80 and eq.5.81 are solved with data from heat capacity and molar volume of minerals and gases to obtain an equilibrium constant for an arbitrarely chosen reaction. The unit **SPELIN** calculates the temperature and the oxygen fugacity of coexisting Fe-Ti oxides, hematite-ilmenite solid solution and the magnetite-ulvospinel solid solution (Spencer & Lindsey, 1981).

The unit **GASEQUILIBRIUM** calculates the equilibrium constants (eq.5.80-5.82) for the gases CH_4, CO, CO_2, H_2O, NH_3, and NO_2 (Table 5.1) at defined PT conditions.

The unit **BUFFEREQUILIBRIUM** calculates the equilibrium constants (eq.5.80-5.82) for a chosen O_2, N_2, H_2O, and NH_3 buffer (Table 5.1).

Equations of state are seperated in individual units. Each unit is able to calculated the pressure, molar volume, and fugacity coefficients of pure gases and gas mixtures. The unit **HOLFLO** contains eq.5.21-24 (Holloway, 1977; Flowers, 1979), unit **JACKER** contains eq.5.25-26 (Jacobs & Kerrick, 1981; Kerrick & Jacobs, 1981), unit **SAXFEI** contains eq.5.20 for H_2O and eq.5.27 for other gas species (Saxena & Fei, 1987a), unit **SAXFEI-HP** contains eq.5.27 (Saxena & Fei, 1987b), unit **BELOSAXE** contains eq.5.28 (Belonoshko & Saxena, 1991a, 1991b), unit **SPYREED** contains an equations with a series in pressure similar to eq.5.20 (Spycher & Reed, 1988), unit **DUAN** contains an equation defined by Lee & Kesler (1975) which is a modification of eq.5.20 (Duan et al., 1992a, 1992b), unit **CHRFRA** contains eq.5.29-31 (Christoforakis & Franck, 1986). Both ideal and non-ideal mixing rules (de Santis et al., 1974; Spycher & Reed, 1988; Duan et al., 1992b) may be used for these calculations.

Dalton's law (eq.5.84 and eq.5.85) is solved for the gas system C-O-H-N in the unit **DALTON**.

$$P_{TOTAL} = \sum p_i \qquad (5.84)$$

$$P = \frac{f_{H_2}}{\gamma_{H_2}} + \frac{f_{N_2}}{\gamma_{N_2}} + \frac{f_{O_2}}{\gamma_{O_2}} + \frac{f_{CH_4}}{\gamma_{CH_4}} + \frac{f_{CO}}{\gamma_{CO}} + \frac{f_{CO_2}}{\gamma_{CO_2}} + \frac{f_{H_2O}}{\gamma_{H_2O}} + \frac{f_{NH_3}}{\gamma_{NH_3}} + \frac{f_{NO_2}}{\gamma_{NO_2}} \qquad (5.85)$$

The equation is rearranged to be solved for one of the gas species, where all other variables are known. The procedure *"Calcluations"* may calculated the fugacity of H_2, N_2, O_2, and the activity of carbon, respectively.

The obtained fugacities are recalculated in the unit **WRITINGS** to appropriate data for a chosen diagram. Atom-equivalents are calculated in the procedure *"COHN"*. The procedure *"CH4-CO2-N2"* includes only the mole fractions of the gas species CH_4, CO_2, and N_2, which are revalued to 100%, to construct a CH_4-CO_2-N_2 compostion diagram. Other gas species may be projected in this diagram. Likewise, the procedure *"CH4-CO2-H2O"* includes only the mole fractions of the gas species CH_4, CO_2, and H_2O. The procedure *"Density"* calculates the density of the gas mixture. The obtained results can be orderly stored in arrays in files, with a *".DAT"* extension, which can easely be used in **GRAPHER Version 1.79D** (Golden Software, Inc. 1988) to construct diagrams.

5.3.2 Programs

The program <u>CURVES</u> uses the units **GRAPHTESTER, LAYOUT, CENTRAL, GASEQUILIBRIUM, HOLFLO, JACKER, SAXFEI, SAXFEI-HP, SPYREED, DUAN, DALTON** and **WRITINGS**. The information which is required to calculate an isopleth (constant mole fraction), or an iso-fugacity (constant partial fugacity) of a gas mixture at defined P-T conditions, is inserted with four menus. A three component gas system (COH, NOH, CHN, CON) is chosen in the first menu. Addition of a constant value for the fourth component may extend the calculations to gas mixtures in the COHN gas

system. In the second menu, the value of the isopleth or iso-fugacity of H_2, N_2, O_2, CH_4, CO_2, H_2O, and NH_3 are enquired. The PT conditions, the equation of state, and the mixing rule are enquired in the third menu. Holloway (1977), Flowers (1979), and Saxena & Fei (1987a) profide equations of state for mixtures of all gas species. Kerrick & Jacobs (1981), Jacobs & Kerrick (1981), Spycher & Reed (1988), and Duan et al. (1992a, 1992b) include only mixtures of CO_2, CH_4 and H_2O. The information about the file which include the calculated values ordered in coloms is entered in the fourth menu. Figure 5.2 shows several applications of the program **CURVES**.

(a)

$$f(CH_4) = 50 \ MPa$$
$$f(CO_2) = 10 \ MPa$$
$$f(H_2) = 40 \ MPa$$
$$f(O_2) = 10^{-19} \ MPa$$
$$f(H_2O) = 60 \ MPa$$

CO

CO_2

CH_4

1

4

7 6 2 5 H_2

O

H_2O

H
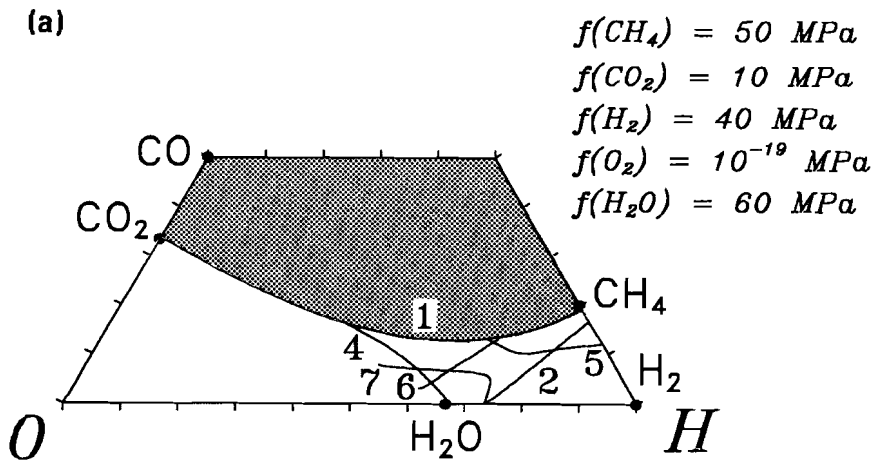
Figure 5.2

*Examples of phase diagrams which are calculated with eq.5.21 (Holloway, 1977; Flowers, 1979) in the program **CURVES** at 1000 K and 100 MPa. The numbered lines in the diagrams are iso-fugacities for graphite-boundary (1), hydrogen (2), nitrogen (3), oxygen (4), methane (5), carbon-dioxide (6), water (7), and ammonium (8). (A) COH diagram, f(N₂) = 0; (B) NOH diagram, a(carbon) = 0; (C) CHN diagram, f(O₂) = 0; (D) CON diagram, f(H₂) = 0; (E) CO₂-CH₄-H₂O composition diagram, f(N₂) = 0; (F) CO₂-CH₄-N₂ composition diagram in equilibrium with graphite. The values of the iso-fugacities are revealed in each diagram. Stable fluid compositions do not exist within the shaded areas.*

(b)

$f(H_2O) = 50\ MPa$
$f(N_2) = 50\ MPa$
$f(NH_3) = 10\ MPa$
$f(H_2) = 40\ MPa$
$f(O_2) = 10^{-19}\ MPa$

(c)

$f(N_2) = 50\ MPa$
$f(NH_3) = 10\ MPa$
$f(H_2) = 60\ MPa$
$f(CH_4) = 50\ MPa$

Figure 5.2 (Continued)

124

(d)

(e)

$f(H_2O) = 50$ MPa
$f(CH_4) = 60$ MPa
$f(CO_2) = 60$ MPa
$f(H_2) = 50$ MPa
$f(O_2) = 10^{-18.7}$ MPa

Figure 5.2 (Continued)

(f)

$$f(H_2O) = 20\ MPa$$
$$f(N_2) = 50\ MPa$$
$$f(NH_3) = 0.4\ MPa$$
$$f(H_2) = 50\ MPa$$
$$f(O_2) = 10^{-18.7}\ MPa$$
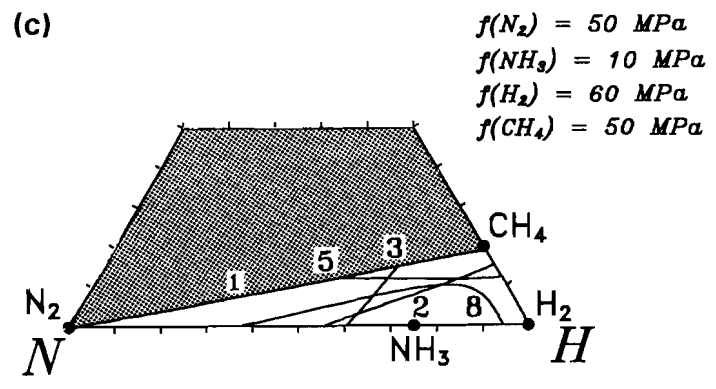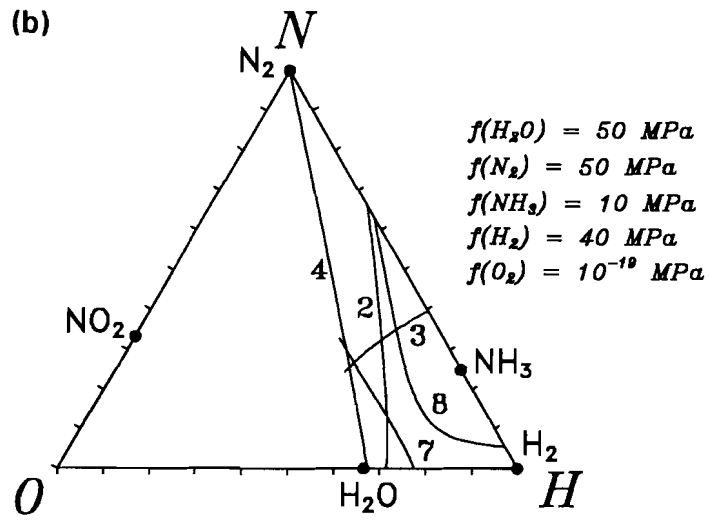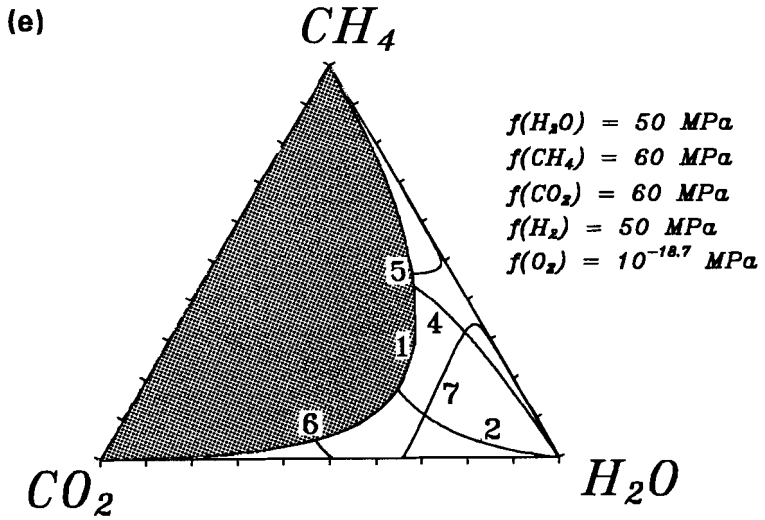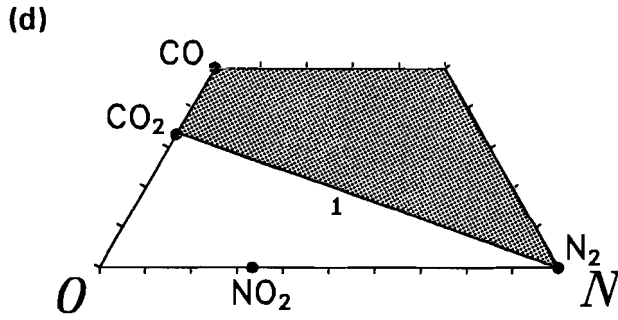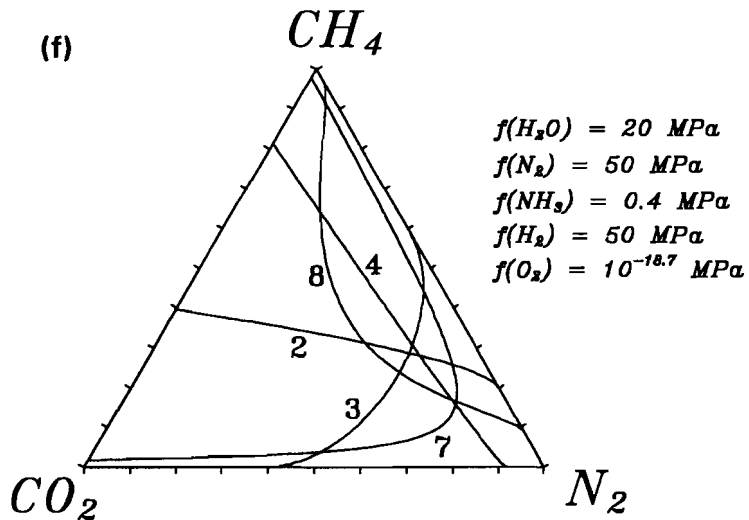
Figure 5.2 (Continued)

The program <u>FLEVOL</u> uses the units **GRAPHTESTER, LAYOUT, CENTRAL, HOLFLO, JACKER, SAXFEI, SAXFEI-HP, SPYREED, DUAN, GASEQUILIBRIUM, BUFFEREQUILIBRIUM, SPELIN, DALTON** and **WRITINGS.** The fluid evolution in rocks may be calculated in the COH or the COHN gas system, which is selected in the first menu. In the second menu a combinations of buffers (Table 5.1) are chosen which define O_2, H_2O, N_2, and NH_3 fugacities. The presence of graphite buffers CH_4, CO, and CO_2. The molar volume of minerals parcipitating in buffer reactions is constant at all P-T conditions (Robie et al., 1978) or varies with temperature and pressure (Berman, 1988; Fei & Saxena, 1987). A representative PT-path for metamorphic rocks which fit to eq.5.86 or to eq.5.87, is enquired in the third menu. Additionally, the upper and lower limits for pressure and temperature are defined.

126

$$P = a_1 T^5 + b_1 T^4 + c_1 T^3 + d_1 T^2 + e_1 T + f_1 \qquad (5.86)$$

$$T = a_2 P^5 + b_2 P^4 + c_2 P^3 + d_2 P^2 + e_2 P + f_2 \qquad (5.87)$$

The fourth menu defines the equation of state and the mixing rule, identical to the program **CURVES**. The information about the file which include the calculated values ordered in coloms is entered in the fifth menu. Figure 5.3 shows several phase diagrams produced with the program **FLEVOL**.

(a)
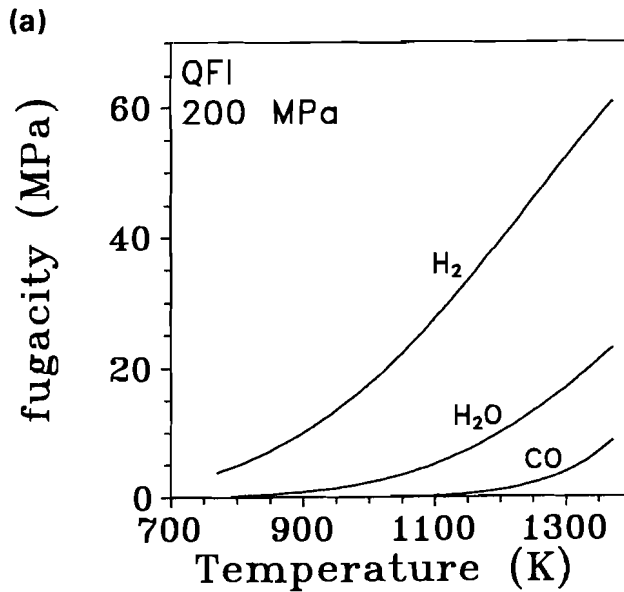
Figure 5.3

Examples of phase diagrams which are calculated with the program
***FLEVOL**. (A) Temperature-fugacity diagram at constant pressure 200 MPa*
for a QFI buffer in the COH gas system. (B) COH diagram for the buffer
combination WI+graphite (1), MI+MQAK (2), and QFM+MQAK (3) at
200 MPa and variable temperatures (in K). (C) Pressure-mole fraction
diagram for the QFM-2 buffer and graphite in the COH gas system. The
*pressure is defined by the equation: P(MPa) = T(K) + 100. **M** and **Q** are*
the phase changes of magnetite (848 K) and quartz (894 K), respectively.

(b)

(c)
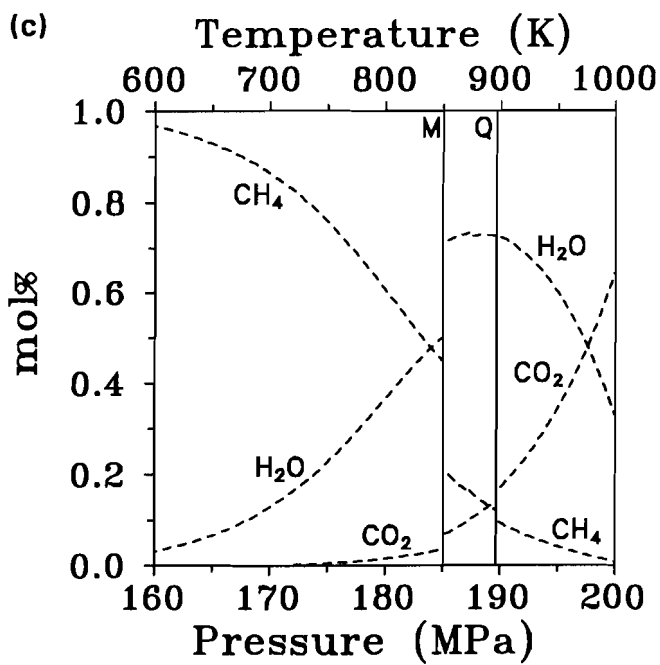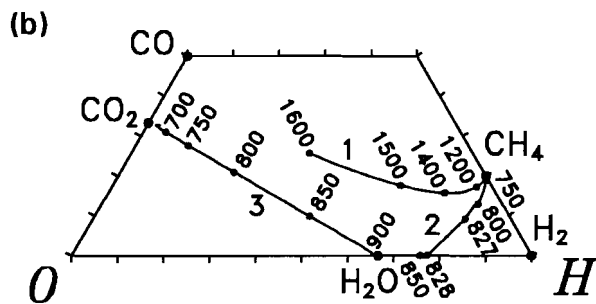
Figure 5.3 (Continued).

The program **MIAT** uses the units **GRAPHTESTER, LAYOUT, CENTRAL, THERMOD, SPELIN, HOLFLO, JACKER, SAXFEI, SAXFEI-HP, BELOSAXO, SPYREED, DUAN, CHRFRA,** and **WRITINGS.** The heat capacity, entropy, enthalpy difference, gibbs energy difference, molar volumes of individual gases and minerals (Table 5.2) may be calculated for any temperature and pressure. Equilibrium constants, $\Delta G_{reaction}$ for stoichiometric reaction are calculated. Fugacity coefficients of the gas species at any P,T, and molefraction may be calculated, and several equations of state may be compared. Isochores, isotherms, and isobars may be calculated for fluids in inclusions with a known composition and density. The density may be derived from homogenization temperatures for all pure gases and for mixtures of CO_2, CH_4, and H_2O. Figure 5.4 reveals several examples of diagrams produced with the program **MIAT**.

(a)

(b)
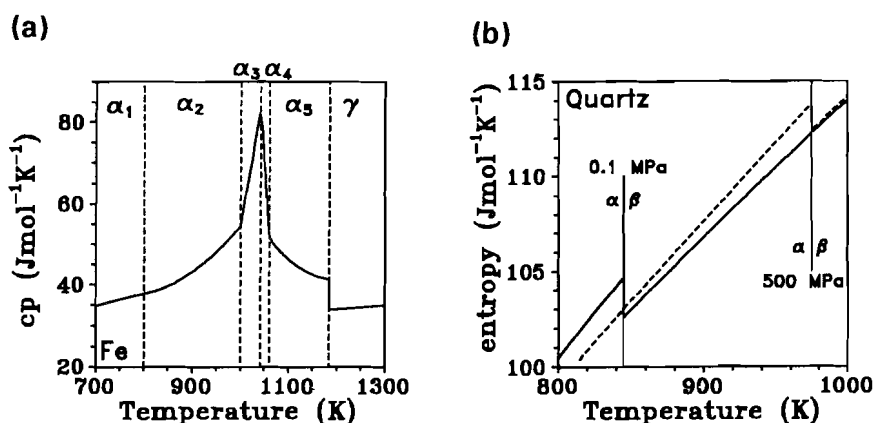
Figure 5.4 (Continued, see page 130)

(c)

(d)
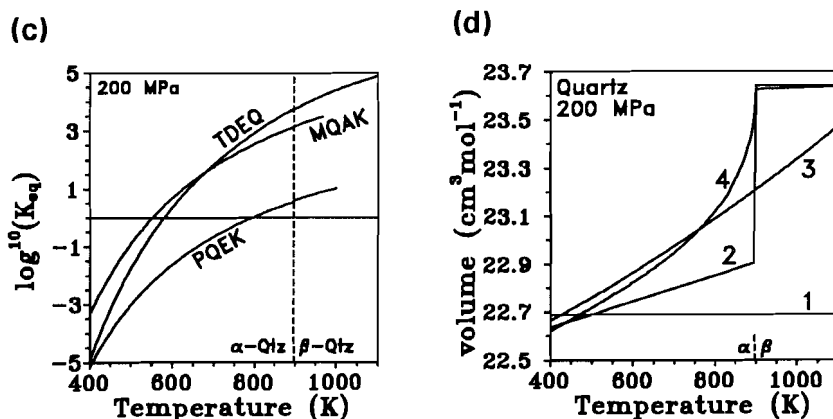
Figure 5.4

Examples of phase diagrams which are calculated with the program
MIAT. (A) Heat capacity-Temperature diagram for iron (at 0.1 MPa),
indicating all phase changes (Barin & Knacke, 1973). (B) Entropy-
Temperature diagram for quartz at 0.1 and 500 MPa. Transition
temperature is derived from Hosieni et al. (1985). (C) Log(K_{eq})-
Temperature diagram for the H_2O buffers TDEQ, MQAK, and PQEK (at
200 MPa). The phase change of quartz is indicated with the dashed line.
(D) Molar volume-Temperature diagram for quartz (at 200 MPa). The
volume of quartz is calculated with data from Robie et al. (1978, line 1),
Berman (1988, line 2), Fei & Saxena (1987, line 3), and Hosieni et al.
(1985, line 4). (E) Fugacity coefficient-Temperature diagram for pure H_2O
at 200 MPa, calculated with several equations of state (SF = Saxena &
Fei, 1987; KJ = Kerrick & Jacobs, 1981; HF = Holloway, 1977, and
Flowers, 1979). (F) Fugacity coefficient-Temperature diagram for CO_2 in
CO_2-H_2O mixtures at 100 MPa), for 0, 0.2, 0.4, 0.6, and 0.8 mol% H_2O
(Kerrick & Jacobs, 1981). (G) Pressure-Temperature diagram with
isochores for CH_4 (in cm³/mol), calculated with eq.5.21 (Holloway, 1977;
Flowers, 1979) at conditions indicated with the black dots. (H) Molar
volume-Pressure diagram with isotherms for H_2O (in K), calculated with
the equation of state defined by Spycher & Reed (1988).

130

(e)

H₂O
200 MPa

γ (fug.coef.)

SF

KJ

H-F

Temperature (K)

(f)

100 MPa

γ (fug.coef.)

0.8

0.6

0.4

0.2

0.0

CO₂

Temperature (K)

(g)

pressure (MPa)

72.23

81.16

90.05

98.87

107.65

CH₄

Temperature (K)

(h)

H₂O

volume (cm³mol⁻¹)

800

700

400

500

600

Pressure (MPa)

Figure 5.4 (Continued)

131
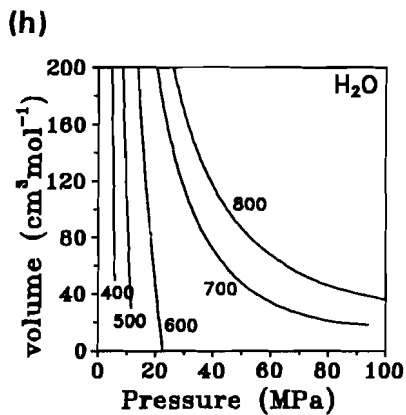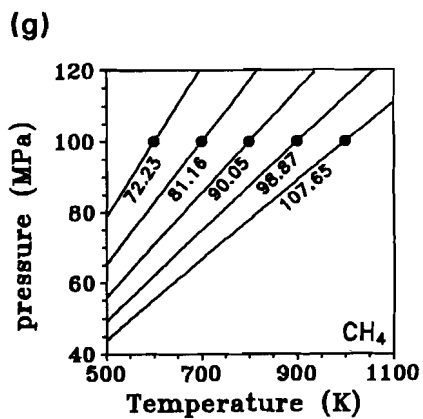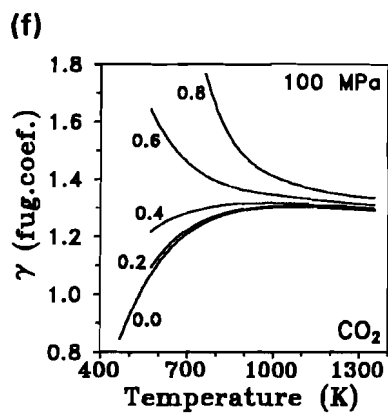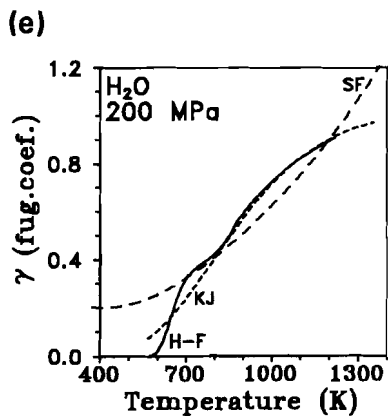
APPENDIX

The programs are originally written at an IBM-compatible *Commodore PC 50II* computer, with a high performance 80386SX microprocessor, a 80387SX numeric coprocessor, and a built-in VGA video circuit (640x480 graphics mode). The programs can be executed at XT and AT computers with a numeric coprocessor. Programming was performed in **TURBO PASCAL Version 5.0** (Borland Inc. 1988). The programs are available on 3½ and 5¼ inch diskettes. The disk contains the files **FLEVOL.EXE, CURVES.EXE,** and **MIAT.EXE,** which are run individually, and the amount of bites used by these programs is 180 K, 170 K, and 170 K, respectively. Furthermore, the disk contains the files **GRAPHTESTER.TPU, LAYOUT.TPU, CENTRAL.TPU, THERMOD.TPU, SPELIN.TPU, GASEQUILIBRIUM.TPU, BUFFEREQUILIBRIUM.TPU, HOLFLO.TPU, JACKER.TPU, SAXFEI.TPU, SAXFEI_HP.TPU, BELOSAXE.TPU, SPYREED.TPU, DUAN.TPU, CHRFRA.TPU, DALTON.TPU,** and **WRITINGS.TPU** which are used in the executable programs. Text styles which are used in the programs, are located in the font files LITT.CHR, SANS.CHR, and TRIP.CHR. The files EGAVGA.BGI, ATT.BGI, CGA.BGI, HERC.BGI, and PC3270.BGI are the graphics device drivers.

The programs can be ordered from R.J.Bakker, Department of Geochemistry, Institute for Earth Sciences, PO.Box 80.021, 3508 TA Utrecht, The Netherlands.

Fig. 13.
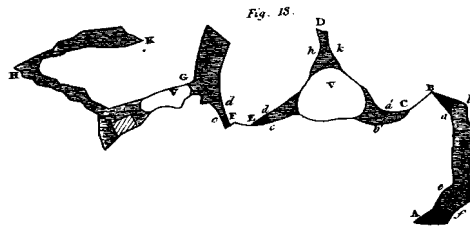
Chapter 6

CALCULATED FLUID EVOLUTION PATH VERSUS FLUID INCLUSION DATA IN THE COHN SYSTEM AS EXEMPLIFIED BY METAMORPHIC ROCKS, ROGALAND SW NORWAY

(this chapter has been submitted to **Journal of Metamorphic Geology**, co-author: J.B.H.Jansen)

6.1 ABSTRACT

Fluid evolution in the COHN system can be calculated for metamorphic rocks if the relevant data are available regarding the mineral assemblages present, and the oxidation and nitrodation state throughout the entire P-T loop. The composition of fluid inclusions observed in granulitic rocks from Rogaland (SW Norway) are compared with theoretical fluid compositions and molar volumes. The fluid parameters are calculated using a P-T path based on mineral assemblages, which are represented by rocks within the pigeonite-in isograd and by rocks near the orthopyroxene-in isograd surrounding an intrusive anorthosite massif. The oxygen and nitrogen fugacities are assumed to be buffered by the coexisting Fe-Ti oxides and chromium-carlsbergite, respectively. Many features of the natural fluid inclusions, including 1) the occurrence of CO_2-N_2-rich graphite absent fluid inclusions near peak M2 metamorphic conditions (1200 K and 400 MPa), 2) the non-existence of

intermediate ternary CO_2-CH_4-N_2 compositions, and 3) the low molar volume CO_2-rich fluid inclusions (36-42 cm^3/mol) are reproduced in the calculated fluid system. The CO_2-CH_4-rich inclusions with minor amount of N_2 (5 mol%) observed, should according to the calculations also include a large proportion of H_2O. The absence of H_2O from these natural high molar volume CO_2-CH_4-rich inclusions and the occurrence of natural CH_4-N_2-rich inclusions are both assumed to result from preferential leakage of H_2O. This has been experimentally demonstrated for H_2O-CO_2-rich fluid inclusions by Bakker & Jansen (1989, chapter 2, and chapter 3), and theoretically predicted by Hollister (1988, 1990). Fluid deficient conditions may explain the relatively high molar volumes. However, the occurrence of CH_4-N_2-rich inclusions and the absence of H_2O cannot be explained using this assumption.

6.2 INTRODUCTION

The evolution of fluids in metamorphic terranes can be traced by accurate measurement of the composition and density of fluid inclusions (fi.s). The trapping sequence of different generations of fi.s can be established from their geometrical relationships. Each generation represents a distinct metamorphic fluids, which only mix locally at intersections. The fluids are often composed of gas species in the COHN system. Nitrogen has been frequently analyzed from rocks and minerals by mass spectrometry. This method entails rock-crushing and mineral-cleaving under a vacuum and is nonselective. The insitu measurement of N_2 in fi.s by non-destructive methods was first described by Dhamelincourt et al.(1979), Swanenberg (1980), and Guilhaumou et al.(1981) using microthermometry and Raman spectroscopy. The composition of metamorphic fluids in the COHN system may of course be influenced by mineral assemblages present in the host rock, and these inturn are dependent on the conditions of metamorphism (Bastoul et al., 1991; Doria et al., 1991). Metamorphic P-T paths from geothermometry and geobarometry of stable mineral assemblages, can be

134

used to calculate the coexisting fluid compositions. The results from these
calculations can than be compared with the natural fi.s observed. In order to
carry out these calculations, several fundamental assumptions must be made.
First, the fluid compositions are defined by the P-T conditions and internal
nitrogen- and oxygen- or hydrogen-fugacity buffers. Second, carbon, oxygen,
hydrogen and nitrogen must remain available in the rock at all P-T conditions.
The presence of minerals containing these elements, which take part in
chemical equilibria, allow their interchange with the fluid phase.

The original source of nitrogen in sedimentary rocks is most often
assumed to be organic matter (Arrhenius, 1950; Stevenson, 1962).
Stevenson (1962) postulated that most nitrogen exists as ammonium ions
held within mineral lattices. In metamorphic and magmatic rocks ammonium
substitutes for potassium in biotite, muscovite, K-feldspar and plagioclase
(Stevenson, 1962; Hallam & Eugster, 1976; Honma & Itihara, 1981; Touret,
1982; Duit et al., 1986; Bos et al., 1988). Dubessy & Ramboz (1986)
evaluated the behaviour of N_2 fluids which originated from the release of
ammonium from minerals during diagenesis and metamorphism.

In order to calculate fluid compositions within the COHN system, we
have developed a Pascal computer program (**Chapter 5**, and Bakker &
Jansen, 1991a). Using this program it is possible to calculated the P-T-V-X
relations of both pure gases and gas mixtures, from the relevant equations of
state, and data on molar volumes, isochoric systems and solvi (Holloway &
Reese, 1974; Holloway, 1977; Flowers, 1979; Kerrick & Jacobs, 1981;
Jacobs & Kerrick, 1981; Saxena & Fei, 1987). Thermodynamic data on
gases and mineral buffers were taken from several sources: the JANAF-
tables; Robie et al. (1978); Eugster & Skippen (1967); and Berman (1988).
Six independent gas reactions (eq.6.1-6) are used to calculate fugacities of
the nine relevant gas species (O_2, H_2, N_2, H_2O, CO_2, CO, CH_4, NH_3 and NO_2),
according to the method described by French (1966).

$$C \; + \; O_2 \; \rightarrow \; CO_2 \qquad\qquad (6.1)$$

$$C \; + \; \frac{1}{2}O_2 \; \rightarrow \; CO \qquad\qquad (6.2)$$

$$C \ + \ 2H_2 \ \rightarrow \ CH_4 \qquad\qquad (6.3)$$

$$H_2 \ + \ \frac{1}{2}O_2 \ \rightarrow \ H_2O \qquad\qquad (6.4)$$

$$\frac{1}{2}N_2 \ + \ \frac{3}{2}H_2 \ \rightarrow \ NH_3 \qquad\qquad (6.5)$$

$$\frac{1}{2}N_2 \ + \ O_2 \ \rightarrow \ NO_2 \qquad\qquad (6.6)$$

The total pressure of the fluid is given by Dalton's law (eq.6.7).

$$P_{total} \ = \ \sum (\frac{f_i}{\gamma_i}) \qquad\qquad (6.7)$$

The parameters P_{total}, f_i and γ_i are total fluid pressure, fugacity and fugacity coefficient of gas-species i, respectively. The total fluid pressure is assumed to be equal to the lithostatic pressure, although this need not be the case (Lamb & Valley, 1985; Skippen & Marshall, 1991). In addition, two equations are needed to define all gas fugacities at given P-T conditions. These two equations are given by mineral buffers that define fugacities of two distinct gas species.

6.3 OXIDATION AND NITRODATION TRENDS IN ROCKS

Mineral assemblages in metamorphic rocks are capable of buffering the concentration of volatile species in metamorphic fluids (Greenwood, 1975). An inventory of fluids in various metamorphic rocks by Rice & Ferry (1982) indicates that buffering is, in general, a far more important control on fluid composition than infiltration. If infiltration of an external fluid occurs, the

136

local pore fluid composition may still be controlled by the buffering capacity of the rock (Rice & Ferry, 1982) until the buffering reaction is exhausted.

The oxidation state of rock may be described by buffer reactions, whose components are not necessarily present in the rock (Haggarty, 1976). For example, the top of the upper mantle is as oxidized as the QFM buffer (Saxena, 1989a). The oxygen fugacity of the lower upper mantle is closer to the WI buffer (Ulmer et al., 1987). Holloway (1981) characterized a hypothetical metamorphic fluid without reference to data on coexisting mineral assemblages. His oxygen fugacities are expressed in terms of their position relative to the QFM buffer. In general, the oxidation state of the lower and upper crust, with relatively well known phase-relations, can be established by the use of a single reaction (Thompson, 1975; Thompson & Thompson, 1976; Ferry, 1979; Ferry & Burt, 1982). Coexisting Fe-Ti oxides (eq.6.8) have been used to estimate temperatures from several igneous and high-grade metamorphic rocks (Buddington & Lindsey, 1964; Spencer & Lindsey, 1981), using the reaction :

$$3Fe(Ti,Fe)O_3 \leftrightarrow 2Fe_2(Ti,Fe)O_4 + O_2 \qquad (6.8)$$
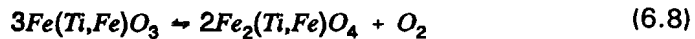
The compositions of these phases at equilibrium are dependent on temperature and oxygen fugacity. Therefore, temperature estimates can be used to indicate the oxidation state of these rocks. Here coexisting Fe-Ti oxides (eq.6.8) are used to calculate the reference oxygen fugacities within the rocks. Lamb & Valley (1985) and Valley et al. (1990) have also used coexisting Fe-Ti oxides (eq.6.8) to calculate local oxygen fugacities in granulites. They used several mineral buffers, assuming ideal stoichiometry, to calculate H_2O fugacity in pelites (eq.6.9 & 6.10) and amphibolites (eq.6.11).

$$2KFe_3(AlSi_3)O_{10}(OH)_2 + O_2 \leftrightarrow 2KAlSi_3O_8 + 2Fe_3O_4 + 2H_2O \qquad (6.9)$$

$$KAl_2Si_3AlO_8(OH)_2 + SiO_2 \leftrightarrow Al_2SiO_5 + KAlSi_3O_8 + H_2O \qquad (6.10)$$

$$Ca_2Mg_5Si_8O_{22}(OH)_2 \rightharpoonup 2CaMgSi_2O_6 + 3MgSiO_3 + SiO_2 + H_2O \quad (6.11)$$
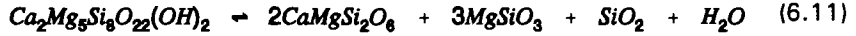
An oxygen buffer with higher capacity (eq.6.12) than coexisting Fe-Ti oxides (eq.6.8) can also be used to calculate oxygen fugacities for charnockites at granulitic conditions (Hansen et al.1984).

$$6FeSiO_3 + O_2 \rightharpoonup 2Fe_3O_4 + 6SiO_2 \quad (6.12)$$
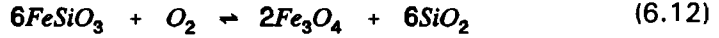
Within the COHN-system, an extra buffer is needed to define the nitrogen fugacity. Hallam & Eugster (1976) estimated equilibrium constants for reactions involving the ammonium silicates tobelite and buddingtonite (eq.6.13 and 6.14).

$$6NH_4Si_3AlO_8(\tfrac{1}{2}H_2O) \rightharpoonup 2NH_4Al_2Si_3AlO_{10}(OH)_2 + 12SiO_2 + 4NH_3 + 3H_2O \quad (6.13)$$

$$2NH_4Si_3AlO_8(\tfrac{1}{2}H_2O) \rightharpoonup Al_2SiO_5 + 5SiO_2 + 2NH_3 + 2H_2O \quad (6.14)$$
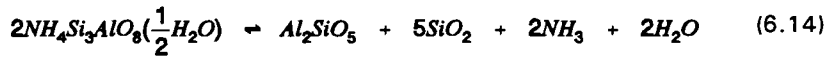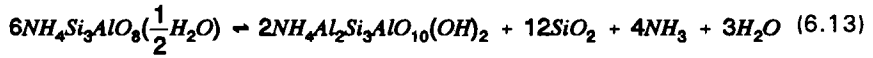
However, the accuracy of their equilibrium constant estimates is not good. Voncken et al. (1988) argued against the existence of natural hydrous buddingtonite. They measured the unit cell parameters of synthetic anhydrous buddingtonite and found these to be similar to the natural supposed hydrous samples. Hallam & Eugster (1976) suggested that ammonium takes part in a cation exchange reaction with muscovite (eq.6.15).

$$K\text{-}muscovite + NH_4^{+(aq)} \rightharpoonup NH_4\text{-}muscovite + K^{+(aq)} \quad (6.15)$$
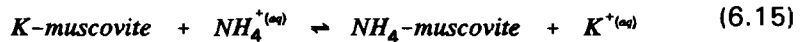
Bos (1990) estimated the distribution coefficient of NH_4^+/K^+ between phlogopite and a chloride vapour phase, analogous to eq.6.15. Preliminary calculations using eq.6.14 indicate that nitrogen is an important gas species in the fluids at high temperatures.

Because of the incomplete and imprecise thermodynamic data, we have used N_2-rich natural fi.s to select an appropriate nitrogen buffer from which to calculate the nitrodation trend. The nitrodation trend is displayed

138

relative to the chromium-carlsbergite buffer (eq.6.16), analogous to the method described by Holloway (1981) for oxygen fugacities.

$$2Cr + N_2 \rightarrow 2CrN \qquad\qquad (6.16)$$

6.4 ROGALAND (SW NORWAY)

The method was tested against fi.s data, from the metamorphic rocks of Rogaland, SW Norway (Fig.6.1A), which have been the subject of many previous studies (Hermans et al., 1975; Sauter, 1983; Tobi et al., 1985; Jansen et al., 1985; Maijer & Padget, 1987; Bol, 1990). In this area three stages of Grenvillian metamorphism (M1-M3) and a Caledonian stage (M4) have been recognized (Table 6.1 and Fig.6.1B) within the migmatitic complex enveloping the Egersund anorthositic complex and the Bjerkreim-Sokndal lopolith (Duchesne et al., 1985).

The precise relationships between the magmatic, metamorphic and tectonic events in this area are not established, although several deformation phases have been distinguished (Hermans et al., 1975; Huijsmans et al., 1981). The earliest phase of isoclinal folding, D1, is presumed to be coeval with migmatization during M1. Basic intrusions, post-dating this migmatization, are deformed by the main phases of deformation (D2-D3). These deformation phases affected the basal parts of the Bjerkreim-Sokndal lopolith (Fig.6.1A), which was intruded during low-pressure granulite facies M2 metamorphism (Pasteels et al., 1979; Wielens et al., 1981). Huijsmans et al.(1981) have suggested that a long period of intense ductile deformation (D2) was coeval with the high temperature metamorphic (M2) event, the behaviour becoming more brittle (D3) at the intermediate temperatures of M3.

Jansen et al. (1985) succesfully used several geothermobarometers in combination with isograd-mapping (pigeonite-in, osumulite-in, hyperstene-in, and biotite-in isogrades, see Fig.6.1A) and age determinations to unravel the poly-metamorphic evolution of this area.

139
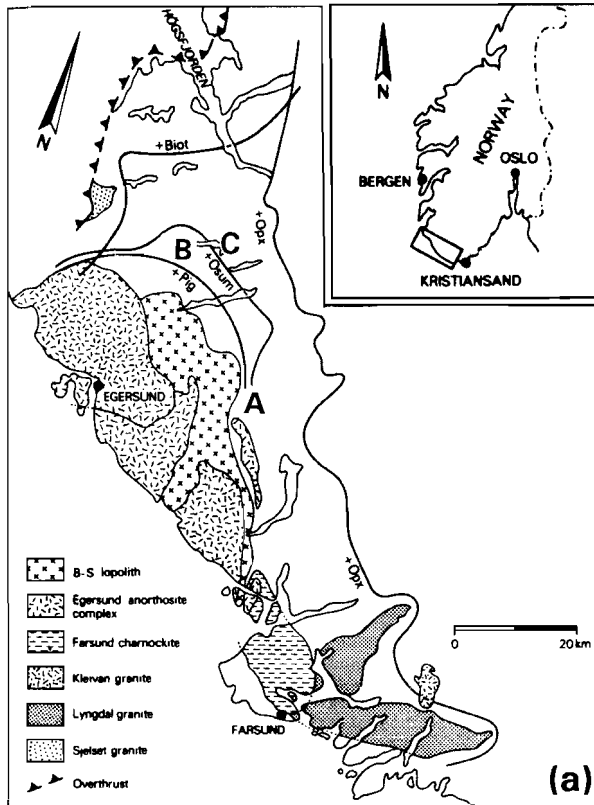
Figure.6.1

a) Isograd map of Rogaland, SW Norway (after Jansen et al. 1985).
Location of rocks used by Swanenberg (1980) and Kerkhof et al. (1991)
for fluid inclusion measurements are indicated by A (Drangsdalen), B
(Austrumdalsvatnet), and C (Faurefjell metasediments). The pigeonite-in,
osumulite-in, hyperstene-in, and biotite-in isograds are indicated with
+Pig, +Osum, +Opx, +Biot, respectively. b) Estimated P-T conditions
for each of the metamorphic events (after Bol, 1990) described in Table
6.1. The supposed uplift path 1 (solid-line) is used for the fluid
calculations in rocks within the pigeonite-in isograd with a maximum
temperature of 1292 K. Path 2 (dashed-line) indicates a typical P-T
development for rocks near the orthopyroxene-in isograd with a maximum
temperature of 1023 K during M2. Both paths are proposed to have equal
pressures during M2 at different peak temperatures. Equal denudation
rates result in a simultaneous comparable pressure development.

140

(b)
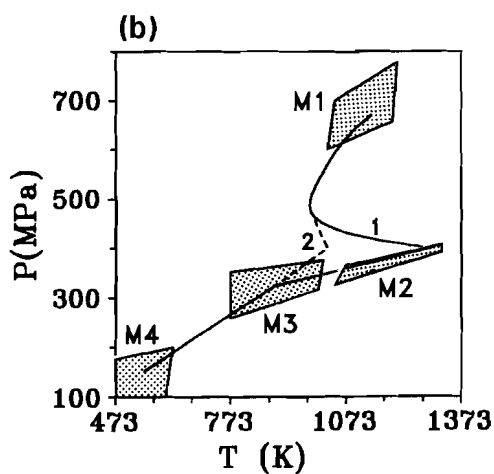
Figure.6.1 (Continued)

	metamorphic grade	age (Ma)	setting
M1	upper amphibolite to granulite	1200	regional metamorphism
M2	granulite (high T, intermediate P)	1050	thermal overprint, induced by intrusion of leuconoritic phase of lopolith
M3	medium grade	970 - 870	retrograde metamorphism during slow, nearly isobaric cooling
M4	prehnite-pumpellyite to greenschist	400	Caledonian orogeny, overthrusting

Table 6.1
Metamorphic grade, age and setting of metamorphism recorded in
Rogaland, SW Norway (after Hermans et al., 1975; Tobi et al., 1985;
Jansen et al., 1985).

Coexisting magnetite-ulvospinel and hematite-ilmenite solid solutions (eq.6.8) were applied as a geothermometer and oxygen barometer for the M2 and M3 events (Duchesne, 1970). A best fit through the data (Fig.10 in Jansen et al., 1985) within a T-f(O_2) diagram coincide with the 60% ulvospinel line, which is used to indicate the oxygen fugacity of the rock at temperatures between 500 and 1500 K (Fig.6.2). This is somewhat more reduced than the QFM buffer, which is also shown in Fig.6.2. Resetting of this geothermometer at low P-T conditions, as argued by Frost & Chacko (1989), results in underestimations of the peak-metamorphic conditions, but does not, however, influence our fluid calculations.
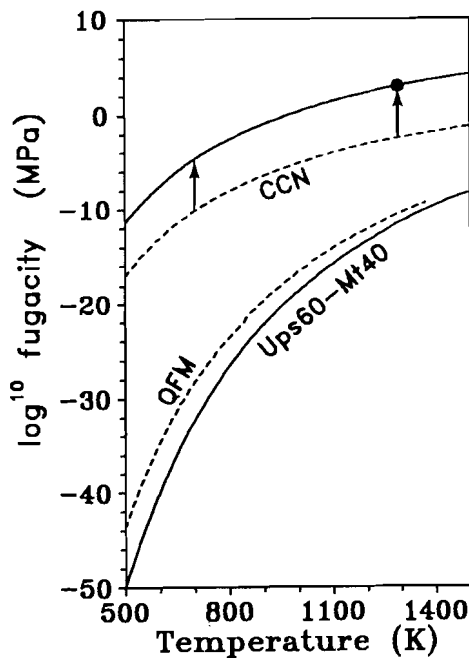
Figure 6.2

Temperature-log$_{10}$ (fugacity) diagram for calculated nitrogen and oxygen fugacities (in MPa). The chromium-carlsbergite buffer (CCN) - dashed line - is shifted + 5.5 log$_{10}$ units (solid line) to obtain the nitrogen fugacity of pure N_2 fi.s at near-peak M2 conditions (black spot). Coexisting Fe-Ti oxides (Ups60Mt40) - solid line - defines the oxygen fugacity. The quartz-fayalite-magnetite buffer (QFM) - dashed line - indicates the relatively reduced nature of the Ups60Mt40 buffer.

142

The P-T paths (**1** and **2** in Fig.6.1B), which are used as a basis for calculation of fluid compositions and molar volumes, are assumed to be representative of these rocks by Bol (1990).

There is no data concerning the natural N_2-buffering in rocks of Rogaland available; a few ammonium analyses reveal up to 55 ppm in biotite of metasedimentary rocks. The dot in Fig.6.2 indicates the nitrogen fugacity (1021 MPa) in pure N_2 fi.s at peak M2 conditions. The calculated nitrogen fugacity from the chromium-carlsbergite buffer (eq.6.16) is shifted 5.5 log_{10} units (CCN + 5.5) to obtain the same fugacity (Fig.6.2).

A fluid inclusion study of the rocks in this area was undertaken by Swanenberg (1980) who used microthermometry (Table 6.2A) and gas chromatography (Table 6.2B) to obtain density and compositional data. His measurements are recalculated to mole fractions and molar volumes of single fi.s. He optically identified six types of fi.s, of which only the carbonic, the biphase H_2O-CO_2, the CH_4-rich and the N_2-rich fi.s are considered here. In general, aqueous fi.s have lower molar volumes than gaseous fi.s. Within a zone of about 10 km around the Bjerkreim-Sokndal lopolith, the average volume percent of H_2O in fi.s seems to be significantly lower (47 vol%) than in the lower-grade metamorphic areas (72 vol%) further away from the contact. Swanenberg (1980) believed that the carbonic fi.s represented the dominant fluid phase present during peak granulite metamorphism (M2), but their density measurements only partly reflect this condition. A N_2-rich fluid must have been trapped in an 'early-secondary' stage, following emplacement of the carbonic fluids. Low-density carbonic fi.s result from partial decrepitation or fluid deficiency (Swanenberg, 1980; Bol, 1990) during peak M2 metamorphic conditions. High-density carbonic and N_2 fi.s (Table 6.2A) strongly suggest a post entrapment re-equilibration of pre-existing fi.s to high-densities during retrograde near-isobaric cooling. An early origin (M1) for high- density CO_2-rich fluids is thought unlikely, as the host minerals may be expected to have recrystallized during the extremely high temperatures of the M2 stage. Mixing of a late stage aqueous fluid, with fluid from decrepitated fi.s resulted in cluster-like arrangements of carbonic and H_2O-CO_2 fi.s or H_2O-N_2 fi.s (Swanenberg, 1980).

fluid inclusion type	volume% H₂O at room T	non-aqueous phase composition (mol%)	density (g/cm³)	molar volume (cm³/mol)	special remarks
Carbonic fi.s	0	CO_2 52 - 100 N_2 48 - 0	Dr = 0.89 Fa = 1.03 - 1.07 range = 0.70 - 1.23	Dr = 49 Fa = 41-43 range = 36-63	Critical homogenization of CO_2 phase at 236 K, (additional N_2 up to 48 mol%). In graphite bearing rocks additional CH_4.
N_2-rich fi.s	0 - 80	k. N_2 10 - 96 CO_2 90 - 4 l. N_2 96 - 100 CO_2 4 - 0 m. N_2 80 - 100 CH_4 20 - 0	l. Dr > 0.78 range = 0.53 - 0.63	l.⊕ Dr < 36 range = 44-52 l.' Dr < 20 range = 22-26	Maximally 55 vol% solid CO_2 at 103 K in fi.s k.
CH_4-rich fi.s	k. 0 - 30	k. CH_4 100	k. 0.03 - 0.04	k.⊕ 400-533 k.' 54-56	fi.s (k.) have well developed negative crystal shape.
	l. 0	l. CH_4 100	l. 0.20 - 0.25	l. 64-80	
CO_2-H_2O fi.s	k. 60 - 90	k. CO_2 100	k. 0.3 - 0.69	l.' 19-26	CO_2 gas phase is occasionally contaminated with N_2. Fi.s (l.) in clusterlike configuration or in trails have positive correlation between T_h of the CO_2 phases and vol% H_2O, end originated from an unmixed fluid.
	l. 0 - 90	l. CO_2 100	l. 0.6 - 0.9	k.' 19-40	

= molar volume with maximum amount of H_2O
@ = molar volume with minimum amount of H_2O

Table 6.2A

Compositions, densities (g/cm³) and molar volume (V_M, cm³/mol) of four types of fi.s deduced from microthermometrical data, identified by Swanenberg (1980). Density and molar volume is occasionally specified for several locations (Dr = Dransdalen, Fa = Faurefjell metasediments indicated with A and B in Fig.6.1A, respectively).

144

location	A (Drangsdalen)		B (Asheim/Snøsvatnet/Nedrabø)	C (Austrumdalsvatnet)	
rock type	amphibole leuconorite		Faurefjell metasediment	Graphite bearing granetiferous migmatite	
Gas-chromatography (Swanenberg 1980)					
CO_2	45.8		28.6 - 83.3	1.0 - 8.7	
CH_4	-		0.1 - 0.4	44.8 - 48.7	
N_2	54.2		16.4 - 71.4	42.6 - 54.6	
Raman-Spectrometry (Kerkhof et al. 1991)					
sample	191 (H3 type)	191 (H1 type)	250	306	311
CO_2	89 - 94	0 - 1	58 - 100	0 - 62	1 - 32
CH_4	0 - 3	1 - 2	-	29 - 100	7 - 92
N_2	5 - 7	97 - 98	0 - 42	0 - 10	5 - 91
H_2O	+	-	+/-	+/-	+/-
graphite	-	-	-	+	+
V_M	45-75	50-90	45-55	54-75	48-60

Table 6.2B

Composition (mol%) and molar volume (V_M, cm^3/mol) of gaseous fi.s from
3 locations in Rogaland (**A, B,** and **C** in Fig.6.1A), for two analytical
techniques: bulk gas-chromatography, giving no information on H_2O
(Swanenberg, 1980) and Raman-spectrometry on individual fi.s, larger 10
μm diameter (Kerkhof et al., 1990). Sample numbers used by Kerkhof et
al. (1990) are indicated. Sample 191 is divided in H1 and H3 fi.s.

145

Raman spectrometry on gaseous fi.s from the area (Table 6.2B) were undertaken by Kerkhof et al. (1991). This confirmed the presence of N_2 and CH_4 in most quartz samples obtained from the metasediments enveloping the Bjerkheim-Sokndal lopolith and the Egersund anorthosite complex. Three compositional groups of gaseous non-aqueous fi.s were recognised, 1) CO_2-N_2 mixtures with 0-3 mol% CH_4, 2) CO_2-CH_4 mixtures with <10 mol% N_2, and 3) N_2-CH_4 mixtures with <10 mol% CO_2. The first group (CO_2-N_2-rich) of fi.s with molar volume between 50 and 55 cm^3/mol, found in the Faurefjell metasediments (Table 6.2B), are assumed by Kerkhof et al. (1991) to be the first generation. Several post-entrapment re-equilibration mechanisms have been used to explain the composition and molar volume changes. Diminution of the inclusion volume and partial decrepitation during post-entrapment isobaric cooling may explain higher (up to 90 cm^3/mol) and lower molar volumes (down to 45 cm^3/mol) of the CO_2-N_2-rich and CO_2 fi.s (Kerkhof et al., 1991). They propose late-stage H_2 diffusion into fi.s, as demonstrated experimentally in quartz by Hall et al. (1989), resulting in the formation of CH_4. CO_2 then reacts with CH_4 to form the more stable graphite and H_2O phases. Thus, the composition and density of fi.s is controlled by H_2 diffusion through the crystal. Therefore, a mineral assemblage buffering the H_2 fugacity may well be controlling the fluid density and composition in apparently isolated and closed fi.s.

6.5 FLUID EVOLUTION CALCULATION

6.5.1 COH-system

Calculations of fluid character are confined to the COH-system due to the probably limited occurrence of nitrogen in fluids, micas, and feldspars. Rocks within the pigeonite-in isograd surrounding the Bjerkheim-Sokndal lopolith and the Egersund anorthosite complex (Fig.6.1A) have suffered three metamorphic stages, M1, M2 and M3. P-T path 1 (Fig.6.1B) is used to calculate fluid compositions and molar volumes. Stable fluid compositions

146

and graphite boundaries shift for the differing conditions of M1, M2 and M3, as illustrated in Fig.6.3A-C at 1138 K and 669 MPa, 1292 K and 400 MPa, 887 K and 323 MPa respectively. At M1 conditions (Fig.6.3A), a CO_2-rich fluid is in equilibrium with graphite, which may precipitate from the fluid on to grain boundaries or within cracks. At M2 conditions (Fig.6.3B), the activity of carbon in the fluid is < 1, and graphite is not stable. Any graphite accessible to the circulating buffered fluid will react totally to form CO_2 and CO. At M3 conditions (Fig.6.3C), the fluid is rich in CH_4 and once again in equilibrium with graphite.
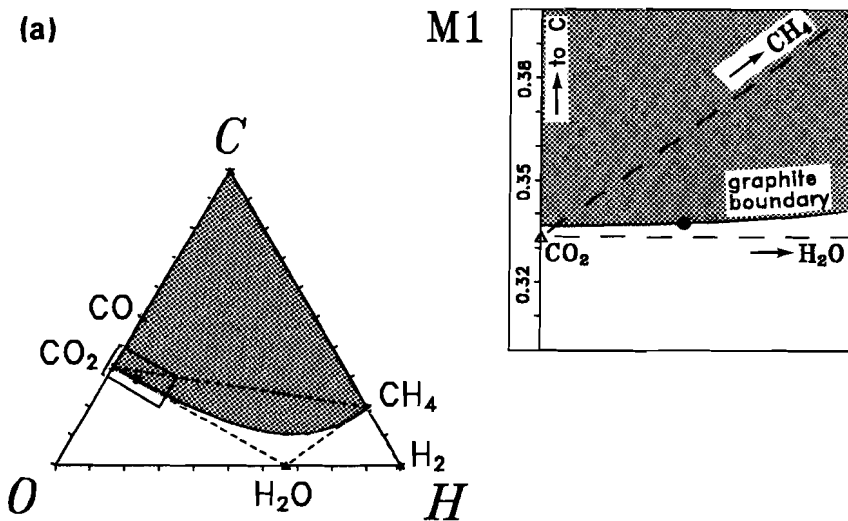
Figure 6.3

COH diagrams for the M1 (a), M2 (b) and M3 (c) metamorphic events. The graphite boundary is indicated with a curved solid line. Stable fluid compositions do not occur in the shaded area. The small rectangles within the COH triangular diagrams (left) are enlarged to square diagrams (right) of which the vertical axis is stretched to emphasize the position of the graphite boundary with respect to the CO_2-CH_4 tie line. The black spot represents the calculated fluid compositions for each metamorphic phase.
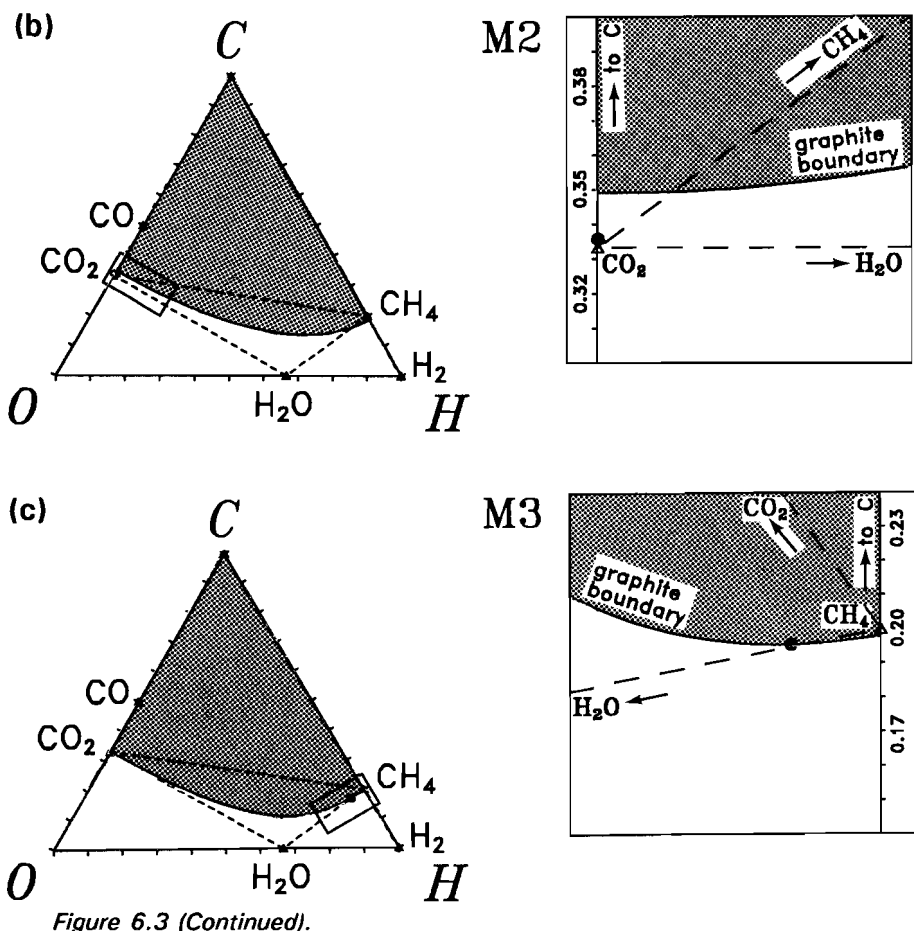
Figure 6.3 (Continued).

The COH-diagrams (Fig.6.3) present fluid compositions at fixed P-T conditions, and do not show the fluid evolution. Furthermore, the exact composition of the fluid cannot be deduced from these diagrams. The proposed retrograde metamorphic P-T paths (Fig.6.1B) indicate a continuous decrease in pressure with time. Therefore, we have chosen a pressure versus fluid composition plot (Fig.6.4) to present the fluid evolution. During M1 the fluid varies in composition from a CO_2-rich fluid at 669 MPa to a H_2O-rich fluid with minor and equal amounts of CO_2 and CH_4 at the lower-pressure boundary of this metamorphic stage at 614 MPa. H_2O remains the major fluid

component between M1 and M2, with minor amount of CH_4. Increasing
temperatures during M2 led once again to a CO_2-rich fluid. At peak
metamorphic conditions during M2, between 427 and 359 Mpa, graphite is
no longer stable (the carbon activity is <1). The fluid composition is CO_2-rich
with minor amounts of CO (not represented in Fig.6.4), whereas the mole
fractions of CH_4 and H_2O are zero. During M3 the fluid evolved from a H_2O-
rich fluid with equal minor amounts of CH_4 and CO_2 at 345 MPa to a CH_4-rich
fluid at 266 MPa. Finally, at M4 conditions, the fluid remains CH_4-rich.
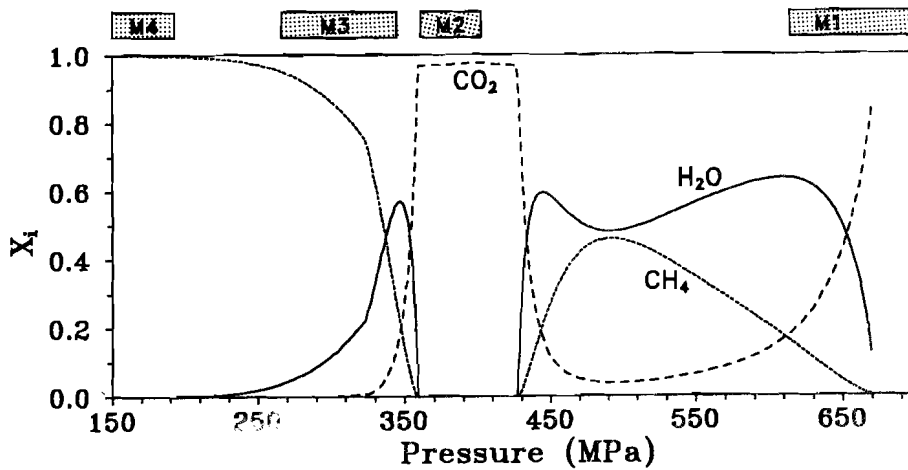
Figure 6.4

*P-X$_i$ (mole fraction) diagram for the gas-species H_2O (solid line), CH_4
(stippled line), and CO_2 (dashed line). P-T conditions of path 1 (Fig.6.1B)
are used to calculate the fluid composition. Metamorphic events are
expressed as M1 (614-700 MPa), M2 (361-402 MPa), M3 (266-345
MPa) and M4 (150-193 MPa).*

6.5.2 COHN-system

Calculations of fluid character were also undertaken for the expanded COHN system. This system has been described from Rogaland by Swanenberg (1980). He describes N_2-rich fi.s postdating the CO_2 rich fi.s at near-peak M2 conditions. As mentioned above, the nitrogen fugacity is calculated at 5.5 log_{10} units (Fig.6.2) above the chromium-carlsbergite buffer (CCN + 5.5). Fig.6.5 is a diagram of pressure versus fluid composition for the COHN system for the same metamorphic P-T path (path 1 in Fig.6.1B) as used for COH-calculations. Additionally, the fluid molar volume and the temperature versus pressure are represented in Fig.6.5. The mole fractions of H_2O, CO_2 and CH_4 in equilibrium with graphite do not significantly change, compared to the COH system in Fig.6.4. Between the M1 and M2 events, H_2O remains the predominant gas species in the fluid. The greatest concentrations of 64.1 and 59.8 mol% occur at 610.0 and 443.1 MPa respectively. The H_2O-rich fluid has a relatively low molar volume, between 32.5 and 37.1 cm^3/mol. CH_4 is the second most abundant gas species, varying between 15.2 and 45.9 mol% along this pressure trajectory. Sometime before the M2 event, CO_2 becomes the most abundant gas species and the molar volume increases drastically over a relative short pressure interval to 50.5 cm^3/mol. If the CO_2 fraction were to reach a maximum of 95.0 mol% at 426.9 MPa, graphite would become unstable. As pressure decreases, the CO_2 fraction decreases and the N_2 fraction of the fluid increases. At 400.0 MPa (peak M2 metamorphic conditions) the fluid is made up entirely of nitrogen, and has a molar volume of 53.1 cm^3/mol. Towards the lower pressure boundary of M2 at 378.6 MPa, CO_2 increases, and it again reaches a maximum of 95.1 mol% at 358.6 MPa with a peak value for molar volume of 54.0 cm^3/mol. At lower pressures the fluid is, again, in equilibrium with graphite. Between M2 and M3, H_2O increases to a maximum of 57.1 mol%, while the molar volume decreases drastically to 41.4 cm^3/mol. During and after M3, CH_4 becomes the dominant gas species in the fluid, while the molar volume increases continuously towards 54.8 cm^3/mol at 150 MPa.
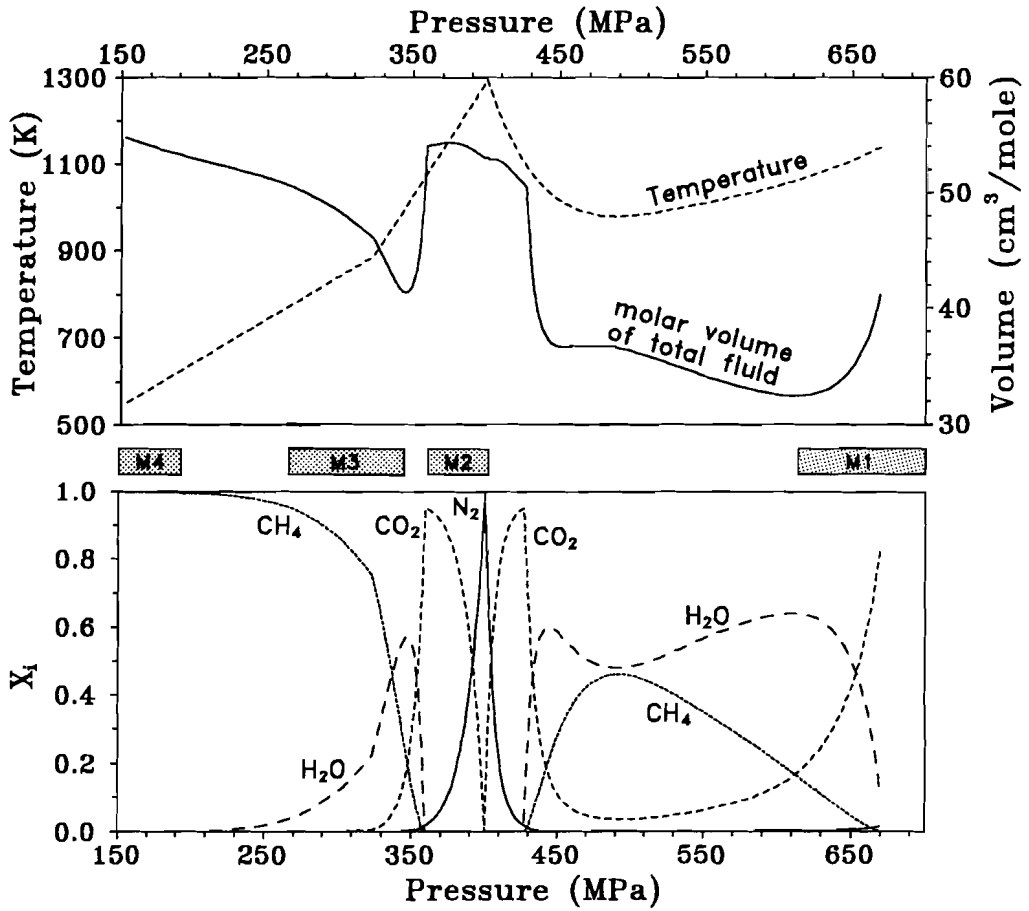
Figure 6.5

Composite P-X_i (molefraction of individual gas-species) and combined P-T
and P-V_M (molar volume) diagram. The main gas-species are N_2 (solid
line), CH_4 (stippled line), CO_2 (short-dashed line) and H_2O (long-dashed
line). The P-T conditions used for fluid calculations correspond to
Fig.6.1B. The CCN buffer and the Ups60Mt40 buffer (Fig.6.2) are used
as nitrogen and oxygen buffer, respectively (see text). The metamorphic
events are expressed as M1 (614-700 MPa), M2 (361-402 MPa), M3
(266-345 MPa) and M4 (150-193 MPa).

To summarise, the most important features established from Fig.6.5 are 1) the instability of graphite in fluids at peak metamorphic conditions (M2); 2) the occurrence of a H_2O-rich fluid between M1 and M2; 3) the relatively low molar volumes of these H_2O-rich fluids; 4) the absence of CH_4-N_2 fluids; 5) a N_2-rich fluid only coexists with CO_2 during M2; and 6) a CH_4-rich fluid develops after M3.

In addition, the fluid evolution has been calculated for rocks near to the hyperstene-in isograd (path 2 in Fig.6.1B), with lower M2 temperatures than path 1 (Fig.6.6). Below 323 MPa and above 478 MPa the fluid evolutions for both paths are similar. The increase in temperature between 323 and 478 MPa results in the fluid remaining H_2O-rich (48.8 - 57.7 mol%), which is then stable with graphite at all conditions. In this path CH_4 and CO_2 are the second (19.5 - 44.5 mol%) and third (4.0 - 18.0 mol%) most abundant gas species, respectively (Fig.6.6). Nitrogen remains a minor component (0.1 - 2.1 mol%).

Figure 6.6
P-X$_i$ (mole fraction) diagram for the gas species N_2 (solid line), CH_4 (stippled line), CO_2 (short-dashed line) and H_2O (long-dashed line), when P-T path 2 (Fig.6.1B) is used for the calculations. The metamorphic events are expressed as M1 (614-700 MPa), M3 (266-375 MPa) and M4 (150-193 MPa).

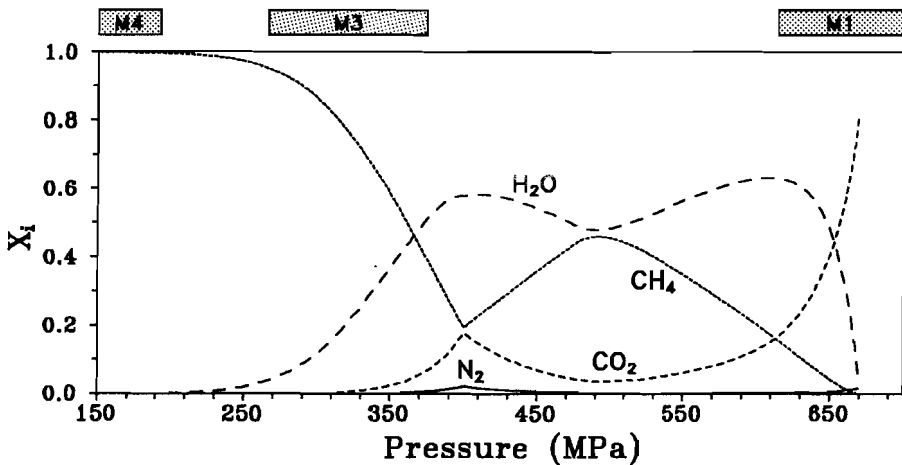In order to illustrate the similarity between our calculated fluid evolutions and those observed in natural fi.s (Swanenberg, 1980; Kerkhof et al., 1991), the patterns shown in Figs.6.4 & 6.5 may be redrawn in a CO_2-CH_4-N_2 diagram (Fig.6.7). The solid symbols represent graphite-bearing fi.s and the open symbols graphite-absent fi.s. As previously mentioned, nitrogen may not be available in the rock system. Therefore, fluid compositions are proposed to occur between two end-values of the nitrogen buffer, zero (Fig.6.4) and CCN + 5.5 (Fig.6.5). Fluid compositions representative of the M1 and M3 event are shown by the shaded areas (Fig.6.7), near the CO_2-CH_4 tie line. The relative amount of N_2 in calculated CO_2-CH_4-rich fluids decreases towards the CH_4 apex. CO_2-N_2-rich fluids of M2 are restricted to the tie line between the pure phases and they do not contain graphite. Fig.6.7 indicates that compositions in the central area and CH_4-N_2-rich fluids do not correspond to any calculated values. The calculated fluid compositions, which are stable in the presence of graphite, correspond to the most frequently observed graphite-bearing fi.s. The calculated molar volumes and the compositional evolution are represented in Fig.6.8. The solid and open arrows in Fig.6.8A indicate schematically the fluid development during M1, and in the period between M1 and M2, respectively. The solid arrow in Fig.6.8B shows the compositional evolution of the fluid from M2 to M3. Corresponding molar volumes along both solid arrows are indicated. Although the fluid compositions from M1 are identical to fluids occurring between M2 and M3, the molar volumes of these fluids differ. Observed molar volumes of natural fi.s (Table 6.2B) by Kerkhof et al. (1991) are grouped with nearly equal values in Fig.6.8C. Values at the CO_2-N_2 tie line and in the CH_4 edge, marked in rectangles correspond to calculated molar volumes.
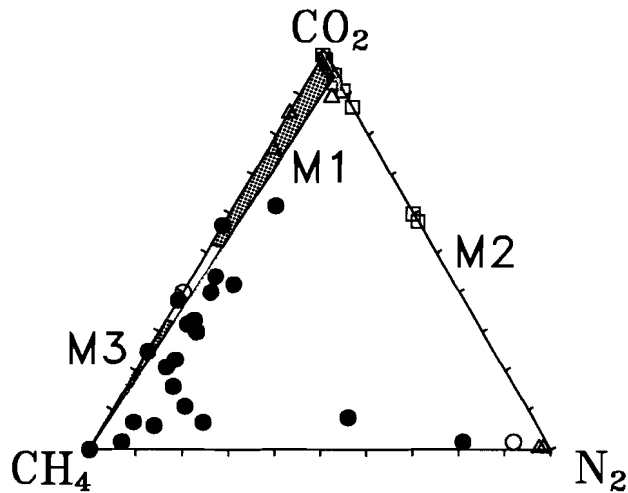
Figure 6.7

*CO_2-CH_4-N_2 composition diagram for M2 (CO_2-N_2 tie line) and M1, M3 (shaded areas) events. Calculated fluid compositions along the CO_2-N_2 tie line (M2) are not in equilibrium with graphite. All other calculated fluid compositions (M1, M3) are stable in the presence of graphite. Data from Kerkhof et al. (1991) are indicated with triangles (location **A** : Drangsdalen and Mydland), squares (location **B** : Faurefjell metasediments) and dots (location **C** : Austrumdalsvatnet). Solid and open symbols represent fi.s with graphite and without graphite, respectively.*

M1→M2

CO_2

(a)

42
36
34
33
32.5

CH_4 N_2

M2→M3

CO_2

54
54.4
45
43
54
42
41.5
53.5
41.4
53.2
(b)
41.5
46—55
53

CH_4 N_2

CO_2

[4]—[54]
75

[46]
60
[50]
56
[45]
(c)
70
75
60
50
[50]
55   55   60 90 [50]
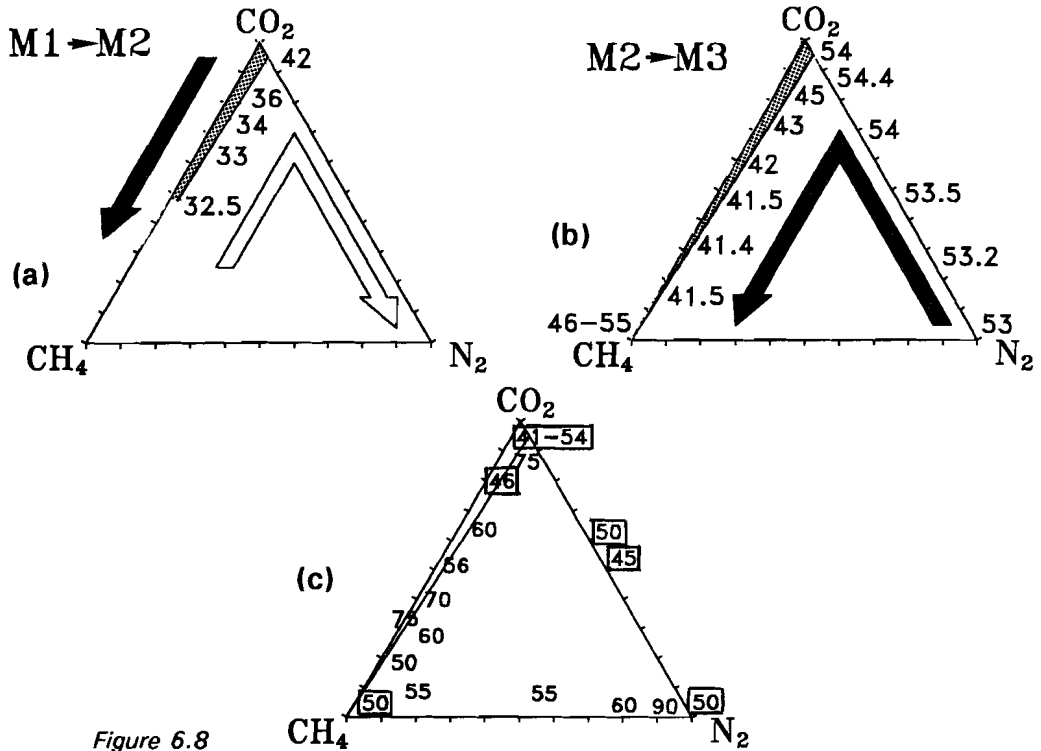
CH_4 N_2

Figure 6.8

*CO_2-CH_4-N_2 composition diagrams with projected molar volumes
(cm³/mol). The calculated compositional evolution is schematically
indicated with : a) M1-M2, solid arrow during cooling of M1 and an open
arrow for prograde changes from M1 to M2; b) M2-M3, solid arrow for
the post M2 peak metamorphic episode towards M3 and M4. The shaded
areas represent all possible compositions during the indicated fluid
evolution; c) Measured values by Kerkhof et al. (1991). Values which
correspond to calculated molar volumes are marked with rectangles.*

6.6 DISCUSSION

The assumptions of our calculations may lead to artefacts. Some measured
natural fi.s (Table 6.2) fall outside the calculated range of fluid compositions
and molar volumes (Figs.6.7 & 6.8C). Discrepancies are evident for CH_4-N_2-
rich natural fi.s and in the absence of H_2O from CO_2-CH_4-rich fi.s with high

molar volumes. Therefore the assumptions must be scrutinized to test their validity.

Periods of deformation are likely to cause brittle strain in mineral grains, and consequently, cracking and crack-healing processes are highly active during these periods. Therefore, we assume crack-healing to occur continuously during the long period of intense deformation (D2-D3), coeval with metamorphism M2-M3.

The possibility that fi.s trapped before peak metamorphic conditions of M2 are preserved, must not be excluded (Samson & Williams-Jones, 1991). The recognition of M1 metamorphic mineral assemblages suggest that fi.s formed during this metamorphic phase may be preserved. Swanenberg (1980) recognized CO_2 rich fi.s with very low molar volumes (36 cm^3/mol, Table 6.2A). These fi.s must have formed from the calculated low molar volume CO_2-rich fluids of 35.6-42.1 cm^3/mol during M1 (Figs.6.5 & 6.8A).

Wilmart et al.(1991) describe CO_2-N_2 fi.s with minor amounts of CH_4 in the Bjerkreim-Sokndal lopolith (Fig.6.1A), which corresponds with our calculated compositions for the enveloping metasediments of near-peak M2 temperatures. The calculated oxygen fugacity in the lopolith (Duchesne, 1970; Wilmart et al., 1991) is approximately 1.5 log_{10} units higher than the enveloping metasediments (Jansen et al., 1985). This fluid in the lopolith would remain CO_2-N_2-rich during M3 according our calculations. The absence of CH_4-rich fi.s, which only occur at very low P-T conditions after M3, may result from scarcity of cracking and crack-healing during this late stage of metamorphism and deformation. Based upon the occurrence of graphite in host minerals and in CO_2-rich fi.s, Wilmart et al.(1991) concluded the fluid system was closed between peak-metamorphic conditions and 523 K, 200-300 MPa. Our calculated fluids fall within this range of conditions.

Iso-fugacities of oxygen and nitrogen are projected in a CO_2-CH_4-N_2 diagram for M1 conditions (1138 K and 669 MPa, Fig.6.9A) to indicate the fluid composition at the defined oxidation and nitrodation states. The oxygen fugacity, calculated with coexisting Fe-Ti oxides (eq.6.8), is $10^{-14.84}$ MPa, restricting the original fluid composition to the CO_2 apex of the diagram. Change in fluid compositions due to variation in oxygen and nitrogen

fugacities can be immediately deduced from Fig.6.9A.

(a)

(b)
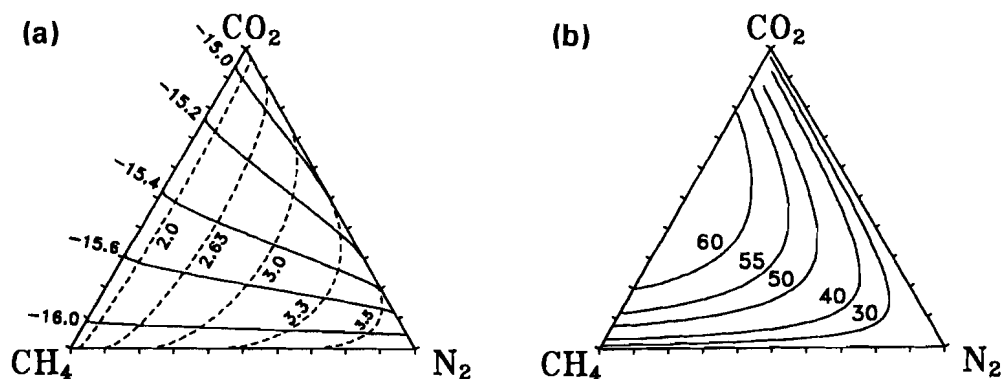
Figure 6.9

CO_2-CH_4-N_2 diagrams for fluid compositions in equilibrium with graphite at M1 conditions. a) iso-fugacities lines (in MPa) of oxygen (solid lines) and nitrogen (dashed lines), values are given in log_{10} units; b) H_2O isopleths (mol%), illustrates that the total amount of CO_2, CH_4 and N_2 may be a minor part of the fluid.

Highly variable mineral assemblages on a millimeter-scale indicate local equilibrium domains for M2 assemblages, suggesting a local oxygen fugacity control (Bol, 1990). Therefore, the oxidation state of the rock may deviate from that of the oxygen buffer used (eq.6.8). Recalculated fluid compositions, using an oxygen buffer one log_{10} unit lower than the previously mentioned buffer (eq.6.8) are shown in Fig.6.10A. Fluids richer in CH_4 are only produced during M1 and M3, while intermediate ternary compositions, which are not observed in natural fi.s (Fig.6.7), occur during M2. The calculations do not result in CH_4-N_2-rich fluids, therefore, more reduced mineral buffers cannot clarify the existence of CH_4-N_2-rich fi.s.

Dubessy et al.(1989) calculated fluids in the COHNS system. They used V-X properties of fi.s measured at room conditions to estimate and to characterize the fluid at high P-T. This method differs from ours in which mineral equilibria are used to define oxygen and nitrogen fugacities at high P-T. Their method is only valid if fi.s do not change in composition and density as a result of external factors. Dubessy et al.(1989) advocated the formation

157

of N_2-rich fluid from NH_4^+-bearing minerals. It was proposed that the hydrogen derived from ammonium reacted to form CH_4 which then became the main carbon-bearing species. Therefore, the simultaneous occurrence of N_2 and CH_4 in fi.s is assumed to be a stable fluid mixture. Our calculations indicate that CH_4-N_2-rich fluids may only occur at reducing conditions which are improbable ($f_{O_2} < 10^{-18}$ MPa in Fig.6.9A) compared to the calculated oxygen fugacities from mineral assemblages in metasediments of Rogaland.

A trail of N_2-rich fi.s, formed at peak M2 conditions may be intersected by new cracks at a later stage, in the presence of a CH_4-rich fluid. Crack-healing during this late stage would result in a new trail with CH_4-rich fi.s. Near the intersection mixing of the two fluids may occur, producing CH_4-N_2 fi.s. Swanenberg (1980) described the presence of such mixed H_2O-CO_2 inclusions at intersections of trails of H_2O-rich and CO_2-rich fi.s.

Fluid deficient conditions have been proposed for several granulitic terranes. Lamb & Valley (1985) calculated a fluid pressure in the COH system of 100 MPa for a lithostatic pressure of 700 MPa, using an O_2 and a H_2O buffer and proposed a vapour absent metamorphism. In order to model such circumstances here, fluid compositions and molar volumes have been calculated for an arbitrarily chosen fluid pressure of one-half the lithostatic pressure (Fig.6.10B). Surprisingly, the compositions are identical to the originally calculated values (Fig.6.7). M2 conditions remain on the CO_2-N_2 tie line, but the upper boundary of M3 shifts towards the CO_2 apex and is responsible for the main part of CO_2-CH_4-rich fi.s. The high molar volumes calculated (Fig.6.10B) correspond to some observed natural fi.s. (Table 6.2 and Fig.6.8C).

The enigmatic CO_2-N_2 rich graphite-absent fi.s from high grade metasediments are thermodynamically stable at high temperature according our calculations. The calculated graphite-absent compositions during M2, which lie along the CO_2-N_2 tie line, are also found in natural fi.s (Fig.6.7). Furthermore, the calculated molar volumes, varying between 51.9 and 54.4 cm^3/mol, correspond to the measured values in natural fi.s (Fig.6.8C). The absence of graphite in fi.s does not imply graphite was absent in the rock during entrapment.

158
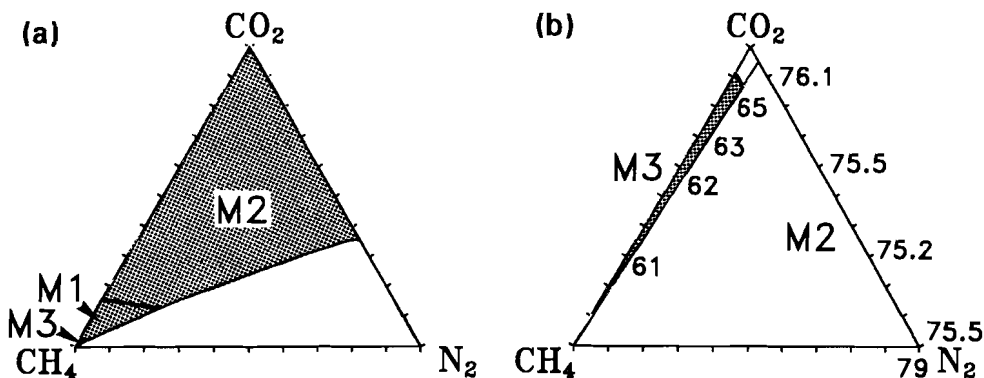
Figure 6.10

a) Calculated fluid composition for a mineral buffer with a O_2 fugacity one log_{10} unit lower than for coexisting Fe-Ti oxides (eq.6.8). Compositions in equilibrium with graphite during M2 (shaded area) in this case cover a larger part of the diagram than in Fig.6.7. Both M1 and M3 are restricted to the CH_4 corner of the diagram; b) Compositions and molar volumes (cm^3/mol) for an arbitrarily chosen P_{fluid} = ½ $P_{lithostatic}$. The shaded area covers all M3 compositions which are richer in CO_2 compared to Fig.6.7. M2 fluids which are not in equilibrium with graphite are positioned at the CO_2-N_2 tie line.

A disadvantage of CO_2-CH_4-N_2 diagrams is that they do not represent complete fluid compositions. These three components may account for only a minor fraction of the fluid. Water isopleths of 30, 40, 50, 55 and 60 mol% are projected in Fig.6.9B for M1 conditions, and demonstrates that H_2O is the major component for most fluids within the diagram. The calculated H_2O-rich fi.s are positioned between CO_2 and CH_4 with minor amounts of N_2 (Fig.6.7), coinciding with the gaseous CO_2-CH_4-rich metastable fluids in natural fi.s (Kerkhof et al., 1991).

Swanenberg (1980) did not identify H_2O-rich fi.s pre-dating CO_2- and N_2-rich fi.s, although H_2O rich fluids occur in our calculations between M1 and M2 (Fig.6.5). Such fi.s may have re-equilibrated completely because the presence of H_2O facilitates solution-precipitation and cracking mechanisms. Swanenberg (1980) assumed a H_2O-rich fluid during the M3 and M4 cycles

following the CO_2 and N_2 rich fluid phases, this is supported by our calculations.

H$_2$O may be extracted from fi.s after entrapment. Hollister (1988, 1990) argued for preferential leakage of H_2O from natural H_2O-CO_2-rich fi.s, and Bakker & Jansen (1989, chapter 2, and chapter 3) have experimentally demonstrated this process. The effect of this process on the fluid composition in inclusions is clearly illustrated in COHN diagrams (Fig.6.11). Point X in Fig.6.11A represents the hypothetical original composition of an inclusion. Leakage of H_2O is indicated by the line XY (Fig.6.11A). The composition is shifted towards Y into the shaded area, where only metastable fluids exist. Chemical stability is then accomplished by precipitation of graphite, indicated by the line YZ in Fig.6.11A, resulting from the reaction (eq.6.17) :

$$CO_2 \; + \; CH_4 \; \rightarrow \; 2H_2O \; + \; 2C \qquad (6.17)$$
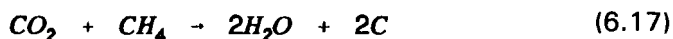
This reaction was experimentally established in fi.s by Kerkhof et al. (1991), the reaction being activated by energy from the Raman laser beam. Equilibrium is then reached for point Z at the graphite boundary (Fig.6.11A), which is richer in CH_4 at more reduced conditions. If preferential H_2O leakage and graphite precipitation occur simultaneously, fluid compositions will shift along the graphite boundary from X to Z towards more CH_4-rich compositions. H_2O leakage would lead to inclusion compositions richer in CO_2 if the initial composition X is positioned at the graphite boundary left of the H_2O-carbon tie line (large-dashed line in Fig.6.11A). Preferential H_2O leakage from fi.s with low mole percent N_2 is indicated in Fig.6.11B. As in Fig.6.11A, H_2O leakage is schematically illustrated with a composition change from X to Y into the shaded area of metastable fluid compositions. Precipitation of graphite, towards stable fluid composition at the graphite boundary, is indicated by the line YZ (Fig.6.11B). The composition of fi.s is relatively enriched in N_2. In the most extreme case, an inclusion with the composition H_2O, CO_2, CH_4 and N_2 of 63, 16, 16 and 2 mol% respectively (for 612.7 MPa and 1064 K in Fig.6.5) may contain only N_2 and solid graphite after leakage of all the H_2O. CO_2 and CH_4 available in equal amounts, may then react completely to H_2O and graphite.
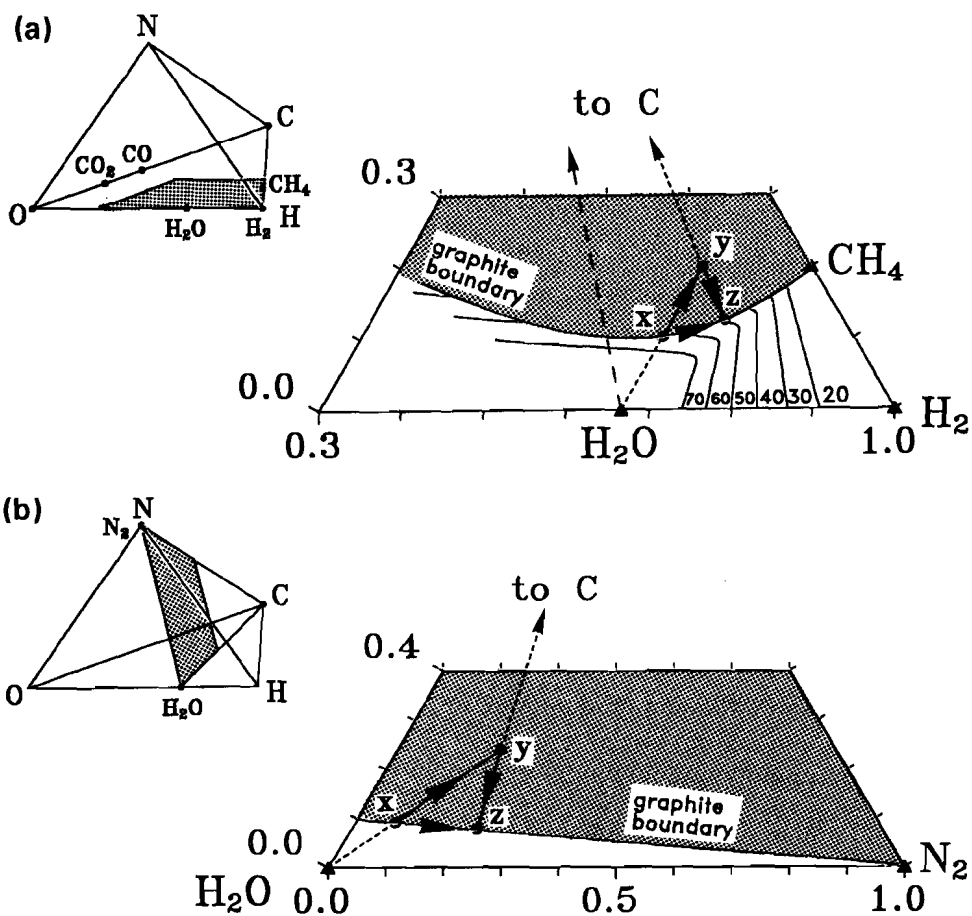
Figure 6.11

Two sections of COHN quadrangle for M1 conditions : a) part of COH diagram; b) part of C-N-H$_2$O diagram. The pure gas-species are indicated with small triangles. The shaded areas in both diagrams represent metastable fluid compositions, the stable compositions are limited by the graphite boundary. The initial fluid composition X at the graphite boundary is arbitrarily chosen. Due to preferential H$_2$O leakage it shifts towards a metastable fluid Y. Composition Y shift to a stable fluid Z if graphite precipitates from the fluid (eq.6.17). If both processes occur simultaneously, the fluid composition X in fact moves along the graphite boundary to Z.

161

CH_4-N_2-rich fluids may develop by preferential H_2O leakage. The arrows in Fig.6.12 indicate the compositional changes for CH_4-rich fi.s in a CO_2-CH_4-N_2 diagram after preferential H_2O leakage and precipitation of graphite (trajectory XZ in Figs.6.11A & B). CH_4 was found by Kerkhof et al. (1991) to be the dominant fluid in inclusions from migmatites (Table 6.2B). Depending on the initial composition and the amount of leakage, several observed natural CH_4-N_2-rich fi.s (Fig.6.7) might be representative of such compositional changes. If no gas-reactions occur in the fi.s after H_2O leakage, a metastable gas assemblage may then remain (trajectory XY in Figs.6.11A & B), corresponding to the observed high molar volumes of natural CO_2-CH_4-rich fi.s. Their position in the CO_2-CH_4-N_2 diagram would not change. Graphite detected in natural fi.s, which have mole-ratio CO_2/CH_4 < 0.6 (Kerkhof et al., 1991) may have precipitated after the entrapment, implying preferential H_2O leakage.
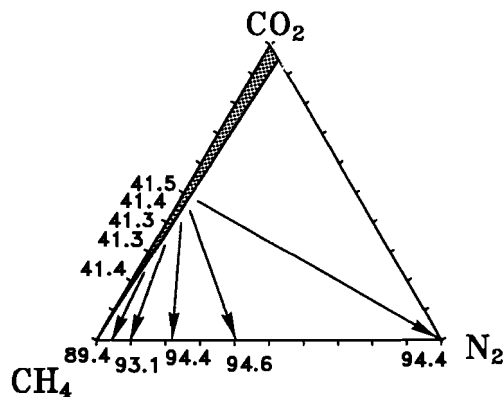
Figure 6.12

CO$_2$-CH$_4$-N$_2$ composition diagrams. The shaded area indicate all calculated fluid compositions, identical to Fig.7. The arrows show changes for stable fluids with small amounts of N$_2$ caused by preferential H$_2$O leakage and precipitation of graphite (eq.6.17). Increased molar volumes (cm^3/mol) are indicated with numbers.

Kerkhof et al. (1991) proposed CH_4 to be the fluid generation following the CO_2-N_2 rich fluids. They assumed the post-entrapment formation of CH_4 in

162

CO_2-N_2 rich fi.s by H_2 diffusion into fi.s, but did not exclude the possibility that CH_4 could be a product of retrograde cooling. Our calculations suggest that this must have been preceded by a H_2O-rich fluid (Fig.6.5). The QFM buffer chosen by Kerkhof et al. (1991) to calculate equal CO_2/CH_4 ratios is too oxidizing and, therefore, not realistic for the metamorphic rocks of Rogaland. Our calculations indicate the presence of a CH_4-rich fluid with minor amounts of H_2O occurring at the end of M3 and lower pressures for rocks within the pigeonite-in isograd.

The fluid evolution of rocks between the pigeonite-in isograd and the orthopyroxene-in isograd (Fig.6.1A) is assumed to vary between the calculated evolutions at high peak-M2 temperatures (Fig.6.5) and low peak-M2 temperatures (Fig.6.6). The CO_2-N_2-rich fi.s from location B (Fig.6.1A and Faurefjell metasediments in Table 6.2B), near the pigeonite-in isograd, correspond to the calculated fluid composition and molar volume at peak M2 conditions (Fig.6.5 & 6.8C). The composition of CO_2-N_2-rich fi.s from location A (Fig.6.1A and Drangsdalen in Table 6.2B), near the pigeonite-in isograd, are similar to calculated compositions (Fig.6.5). However, several measurements of molar volume of nearly pure N_2 and CO_2 fi.s are too high, indicating possible post-entrapment re-equilibration through volume adjustments. Fi.s from location C (Fig.6.1A and Austrumdalsvatnet in Table 6.2B) are CH_4-N_2-rich and CH_4-CO_2-rich. Graphite is present, and H_2O is occasionally absent in these fi.s. These rocks are located further from the intrusive complex, and nearer to the orthopyroxene-in isograd (Fig.6.1A). Therefore, the natural fluid must resemble the calculated fluid in Fig.6.6, in which H_2O is the most abundant and CH_4 the second most abundant gas species. The high mole fraction of H_2O would cause fi.s easily to re-equilibrate by preferential leakage of H_2O, and possible volume adjustments. A metastable gas mixture remains which has more than 50 mol% CH_4, or this gas mixture reacts to more stable CH_4-N_2-rich compositions which implies precipitation of graphite in fi.s.

6.7 CONCLUSIONS

Information about mineral assemblages, timing of metamorphic or magmatic events, deformation phases and oxidation/nitrodation state in metamorphic rock can be used to calculate fluid evolutions with corresponding compositions and molar volumes.

Although scarse thermodynamic information is available for natural nitrogen bearing minerals, the chromium-carlsbergite buffer (eq.6.16) can be successfully used to indicate the N_2 fugacity of the rock, analogous the method for O_2 fugacity described by Holloway (1981).

Natural fi.s recorded in Rogaland (Swanenberg, 1980; Kerkhof et al., 1991) correspond partly with calculated compositions and molar volumes of fluids based on a P-T path, oxygen and nitrogen buffer, as exemplified by 1) the absence of graphite in CO_2-N_2-rich fi.s, 2) the absence of intermediate ternary compositions, 3) high density CO_2-rich fi.s (36-42 cm^3/mol), 4) CO_2-CH_4-rich fi.s with minor amounts of N_2 (up to 5 mol%) during M2-M3.

The existence of CH_4-N_2-rich fi.s can be explained by preferential H_2O leakage - the remnant unstable composition subsequently reacting to a stable CH_4-N_2-rich fluid - or mixing of intersecting trails of N_2-rich and CH_4-rich fi.s, and not, however, by introducing more reduced fluids into the system, or by assuming fluid deficient conditions.

High molar volume CO_2-CH_4-rich fi.s with low mole fractions of H_2O are unstable between M2-M3 conditions and must have resulted from preferential H_2O leakage.

Post entrapment alteration of fi.s, which is proposed by Kerkhof et al. (1991) to explain their measured gaseous fluids, must have affected mainly H_2O-rich fi.s.

Fig. 13.
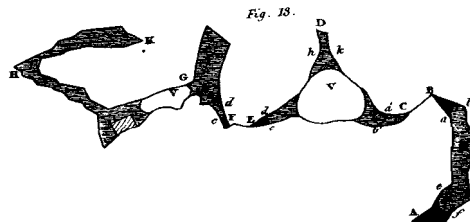
Chapter 7

CONCLUDING REMARKS

Returning to the question: "Can fi.s change in density and composition?", postulated in **Chapter 1**, experimental and theoretical considerations offer convincing positive answers with applications to fluid inclusions studies of natural metamorphic quartz lenses.

7.1 EXPERIMENTS

Preferential non-decrepitative H_2O leakage occurred for experimentally re-equilibrated synthetic CO_2-H_2O fluid inclusions in Brazilian quartz. During hydrostatic re-equilibration experiments, the inclusions were submitted to internal overpressure and underpressure at high temperatures, in order to simulate the effect of uplift and burial on fluid inclusions in natural metamorphic rock. The remaining fluid inclusions were relatively enriched in CO_2 and were reduced in density, which was registered through volumetric estimations and homogenization temperature measurements. Several overpressurized inclusions decrepitated during experimentation. A wide range of inclusion compositions and densities were generated from one type of synthetic CO_2-H_2O fluid inclusion, with initially an uniform composition and density, as a result of local variations in degree of recrystallization.

7.2 LEAKAGE MODEL

Bulk diffusion of H_2O through quartz can not be responsible for the amount of leakage involved. The diffusion coefficient is too small to have a noticeable effect on the density and composition of re-equilibrated inclusions.

Dislocations are able to account for the observed preferential H_2O leakage, by selective H_2O diffusion through dislocations which are connected to an original CO_2-H_2O fluid inclusions. The questions remain: "How much H_2O can a dislocation subtract from a fluid inclusion?" and "Why is CO_2 not measurable leaking through dislocations?". A few mobile dislocations in the crystal are able to generate new dislocations at inclusions, and each dislocation carry away a certain amount of H_2O from the fluid inclusion. The creation of many localized dislocations at fixed positions around fluid inclusions is another adequate way to remove H_2O from fluid inclusions during plastic deformation. Absorption calculations on small pores in quartz indicate that a homogeneous gas mixture of CO_2 and H_2O may separate in a H_2O-rich phase at the quartz surface or in small pores, and in a CO_2-rich phase in the bulk fluid. Information about the physical and chemical behaviour of CO_2 in dislocations, which may be regarded as small pores, is scarce.

After the re-equilibration experiments, quartz have a larger amount and variety of dislocations and planar defects around both overpressurized and underpressurized fluid inclusion, than the initially synthesized fluid inclusions. Small bubbles, fixed at dislocation lines and planar defects around re-equilibrated inclusions, are proposed to be the result of recovery in strained crystals. The small bubbles may grow to optically visible "implosion halos" for underpressurized fluid inclusions, by selective diffusion of H_2O, silicon, and oxygen along dislocations, which may account for noticeable preferential H_2O leakage.

# 7.3 IMPLICATIONS FOR NATURAL FLUID INCLUSIONS IN METAMORPHIC ROCK

Post-entrapment preferential H_2O leakage of aqueous inclusion in natural rock finally result in metastable low density CO_2-CH_4-rich inclusions and gaseous CH_4-N_2-rich inclusions indicating circumstances which are too reducing. Calculated non-aqueous fluids in inclusions (eg. high density CO_2, and CO_2-N_2 mixtures) are confirmed by the recorded non-aqueous fluid inclusions from granulites in Rogaland (SW Norway). However, the recorded CH_4-N_2-rich and the CO_2-CH_4-rich inclusions are thermodynamically forbidden for the entire cooling path. The fluid composition and density calculations are based on the physical data of the well documented metamorphism of Rogaland, including geothermometry and geobarometry. The oxidation state and the nitrodation state during metamorphism, as it is fixed by mineral assemblages in rocks, is a tool to estimate the composition of a coeval circulating fluid, which might additionally be trapped in crystals. Quenched mineral reactions involving oxygen or nitrogen during metamorphism may expose the oxidation state and nitrodation state of the rock.

Preferential H_2O leakage from thermodynamically stable CO_2-H_2O-rich fluid inclusions is a highly active process during metamorphism, and declares inclusion densities and H_2O mole fractions which are too low. The microstructure around fluid inclusions in natural vein quartz from Naxos (Greece) was inspected with TEM, and compared to experimentally re-equilibrated Brazilian quartz, which have leaked preferentially H_2O. The experimentally healed cracks show similar defect structures, which indicate that compareble recrystallization processes must have affected Naxotian quartz lenses, and consequently H_2O leakage must have occurred.

Metamorphic conditions obtained by isochore extrapolation are not realistic if the amount of deformation and recrystallization of the rock is unknown. For future studies on fluid inclusions in metamorphic quartz lenses, the effect of deformation on aqueous inclusions can not be ignored. The calculated fluid from mineral assemblages and the TEM investigations, may clearly indicate that fluid inclusions may have leaked preferentially H_2O.

Therefore, gaseous fluid inclusions have not necessarily always been gaseous, but might have contained high quantities of H_2O.

The supposed trend that granulites and mantle rocks contain more CO_2 than H_2O in fluid inclusions may partly be caused by the fact that before exposure, these deep rocks have usually suffered more intensive recrystallization during uplift than shallow rocks.

Fig. 13.
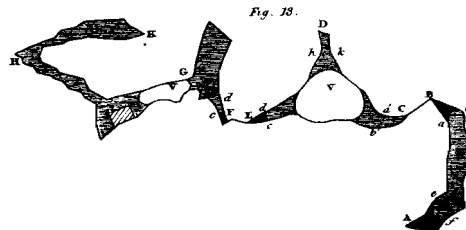
The end

REFERENCES

Aines , R.D., Kirby, S.H. & Rossman, G.R. (1984) Hydrogen speciation in synthetic quartz. *Physics and Chemistry of Minerals,* **11,** 204-212.

Anderson, G.M. & Burnham, C.W. (1965) The solubility of quartz in supercritical water. *American Journal of Science,* **263,** 494-511.

Andriessen P.A.M. (1978) Isotopic age relations within the polymetamorphic complex of the island of Naxos (Cyclades, Greece). *PhD.Thesis, Verh.ZWO -Laboratorium voor isotopen-geologie,* Amsterdam, 71 p.

Andriessen, P.A.M., Boelrijk, N.A.I.M., Herbeda, E.H., Priem, H.N.A., Verdurmen, E.A.Th. & Verschuren, R.H. (1979) Dating events of metamorphism and granitic magmatism in the Alpine Orogen at Naxos (Cyclades, Greece). *Contributions to Mineralogy and Petrology,* **69,** 215 -225.

Arrhenius, G. (1950) Carbon and nitrogen in subaquatic sediments. *Geochimica et Cosmochimica Acta,* **1,** 15-21.

Baker J., Bickle M.J., Buick I.S., Holland T.J.B. & Matthews A. (1989) Isopotic and petrological evidence for the infiltration of waterrich fluids during the Miocene M2 metamorphism on Naxos, Greece. *Geochimica et Cosmochimica Acta,* **53,** 2037-2050.

Bakker R.J. & Jansen J.B.H. (1989) Experimental evidence for leakage of H_2O from CO_2-H_2O rich fluid inclusion. *Terra Abstracts, EUG V Strasbourg,* **1,** 320.

Bakker, R.J. & Jansen, J.B.H. (1990) Preferential water leakage from fluid inclusions by means of mobile dislocations. *Nature,* **345,** 58-60.

Bakker, R.J. & Jansen, J.B.H. (1991a) Stability of CO_2-CH_4-N_2 rich fluid inclusions (abstr.). *Plinius, ECROFI V,* **5,** 11-13.

Bakker, R.J. & Jansen, J.B.H. (1991b) Experimental post-entrapment water loss from synthetic CO_2-H_2O inclusions in natural quartz. *Geochimica et Cosmochimica Acta,* **55,** 2215-2230.

Balderman M.A. (1974) The effect of strainrate and temperature on the yield point of hydrolytically weakened synthetic quartz. *Journal of Geophysical Research,* **79,** 1647-1652.

Barin, I. & Knacke, O. (1973) *Thermochemical Properties of Inorganic Substances,* Springer-Verlag, Berlin.

Bastoul, A., Pironon, J. & Cuney, M. (1991) Nitrogen geochemistry in metamorphic fluids and minerals from a Raman and micro FT-IR study. The example of the Central Jebilets, Morocco (abstr.). *Plinius, ECROFI XI,* **5,** 16.

Belonoshko, A.B. (1989) The thermodynamics of the aqueous carbon dioxide fluid within pores. *Geochimica et Cosmochimica Acta,* **53,** 2581-2590.

Belonoshko A. & Saxena S.K. (1991a) A molecular dynamics study of pressure-volume-temperature properties of super-critical fluids: 1.H_2O. *Geochimica et Cosmochimica Acta,* **55,** 381-387.

Belonoshko A. & Saxena S.K. (1991b) A molecular dynamics study of pressure-volume-temperature properties of super-critical fluids: 2.CO_2, CH_4, CO, O_2, and H_2. *Geochimica et Cosmochimica Acta,* **55,** 3191-3208.

Berman, R.G. (1988) Internally-Consistent Thermodynamic Data for Minerals in the System Na_2O-K_2O-CaO-MgO-FeO-Fe_2O_3-Al_2O_3-SiO_2-TiO_2-H_2O-CO_2. *Journal of Petrology,* **29,** 445-522.

Berman R.G. & Brown T.H. (1985) Heat capacity of minerals in the system Na_2O-K_2O-CaO-MgO-FeO-Fe_2O_3-Al_2O_3-SiO_2-TiO_2-H_2O-CO_2 : representation, estimation, and high temperature extrapolation. *Contribution to Mineralogy and Petrology,* **89,** 168-183.

Berthelot M. (1879) *Essai de méchanique chimique fondée sur la thermochimie.* (ed. Dunod) Paris.

Blacic J.D. (1975) Plastic deformation mechanisms in quartz: effect of water. *Tectonophysics,* **27,** 271-294.

Blacic J.D. (1981) Water diffusion in quartz at high pressure: tectonic implications. *Geophysical Research Letters,* **8,** 721-723.

Bodnar, R.J. & Bethke, P.M. (1984) Systematics of stretching of fluid inclusions I: Fluorite and sphalerite at 1 atmosphere confining pressure. *Economic Geology,* **79,** 141-161.

Bol, L.C.G.M. (1990) Geochemistry of high-temperature granulitic supracrustals from Rogaland, SW Norway. Ph.D.thesis, *Geologica Ultraiectina,* **66,** 1-137.

Bos, A., Duit, W., V.d.Eerden, A.M.J. & Jansen, J.B.H. (1988) Nitrogen storage in biotite : An experimental study of the ammonium and potassium partitioning. between 1M-phlogopite and vapour at 2kb. *Geochimica et Cosmochimica Acta,* **52,** 1275-1283.

Bos, A. (1990) Hydrothermal element distributions at high temperatures. Ph.D.thesis, *Geologica Ultraiectina,* **69,** 1-99.

Bouillier, A.-M., Michot, G., Pecher, A. & Barres, O. (1989) Diffusion and/or plastic deformation around fluid inclusions in synthetic quartz: new investigations. In: *Fluid movements - Element Transport and Composition of the Deep Crust* (ed. D.Bridgewater); *NATO ASI Series,* **C 281,** pp.345-360, Kluwer Academics Publishers.

Boyle R. (1662) A defence of the doctrine touching the spring and weight of the air. In: *New experiments physio-mechanicall, touching the spring of air and its effects, (made, for the most part, in a new pneumatical engine).* 1 -107, Oxford, Hall.

Boyle R. (1672) *An essay about the origine and virtues of gems,* pp.185, London, William Godbid.

Brace, W.F. & Walsh, J.B. (1962) Some direct measurements of the surface energy of quartz and orthoclase. *American Mineralogist,* **47,** 1111-1122.

Breislak S. (1818) Institutions géologiques (french translation by P.J.L. Campas) vol.1, Milan.

Brewster D. (1823) On the existence of two new fluids in the cavities of minerals, which are immiscible, and possess remarkable physical proporties. *Transactions Royal Society of Edinburgh,* **10,** 1-14.

Brewster, D. (1835) Observations relative to the structure and origin of the diamond. *Transactions Geological Society of London,* **3,** 455-459.

Brewster, D. (1848) On the phenomenon of luminous rings in calcareous spar and beryl, as produced by cavities containing the two new fluids. *Philosophical Magazine,* series 3, **33,** 489-493.

Brewster, D. (1861) On the pressure cavities in topaz, beryl, and diamond, and their bearing on geological theories. *Transactions Royal Society of Edinburgh,* **23,** 39-44.

Brok S.W.J. den & Spiers C.J. (1991) Experimental evidence for water weakening of quartzite by microcracking plus solution-precipitation creep. *Journal of the Geological Society of London Bulletin,* **148,** 541-540.

Brunner, G.O. von, Wondratschek, H. & Laves, F.Z. (1961) Ultrarotuntersuchungen über den Einbau von H in naturlichen Quartz. *Zeitschrift für Electrochemie* **65,** 735-750.

Buddington, A.F. & Lindsey, D.H. (1964) Iron-Titanium oxide minerals and synthetic equivalents. *Journal of Petrology* **5,** 310-357.

Buick, I.S. (1991) The late alpine evolution of an extensional shear zone, Naxos, Greece. *Journal of the Geological Society of London,* **148,** 93-103.

Buick, I.S & Holland,T.J.B. (1989) The P-T-t path associated with crustal extension, Naxos, Cyclades, Greece, In: *Evolution of Metamorphic Belts* (eds. J.S.Daly, R.A.Cliff, and B.W.D.Yardley), *Geological Society of London, Special Publications,* **43,** 365-369.

Buick, I.S. & Holland, T.J.B. (1991) The nature and distribution of fluids during amphibolite facies metamorphism, Naxos (Greece). *Journal of Metamorphic Geology,* **9,** 301-314.

Burke E.A.J. and Lustenhouwer W.J. (1987) The application of a multichannel laser raman microprobe (Microdil-28) to the analysis of fluid inclusions. *Chemical Geology,* **61,** 11-17.

Carnahan, N.F. & Starling, K.E. (1972) Intermolecular repulsions and the equation of state for fluids. *American Institute for Chemical Engineering,* **18,** 1184-1189.

Carstens, H. (1968) The lineage structure of quartz crystals. *Contributions to Mineralogy and Petrology,* **18,** 295-304.

Carstens, H. (1969) Arrays of dislocations associated with healed fractures in natural quartz. *Norges Geologiske Undersøkelse,* **258,** 367-369.

Carter, N.L., Kronenberg, A.K., Ross, J.V. & Wiltschko, D.V. (1990) Control of fluids on deformation of rocks. In: *Deformation mechanisms, rheology and tectonics* (eds. R.J.Knipe & E.H.Rutter) *Geological Society Special Publications,* **54,** 1-13.

Christoforakis, M. & Franck, E.U. (1986) An equation of state for binary fluid mixtures to high temperatures and high pressures. *Berichte der Bunsengesellschaft für Physikalische Chemie* **90**, 780-789.

Davy H. (1822) On the state of water and aeriform matter in cavities found in crystals. *Philosophical Transactions Royal Society of London*, 367-376.

Debye P. (1912) Zur Theorie der spezifischen Warmen. *Annalen der Physik*, **39**, 789-839.

Dennis, P.F. (1981) Effect of variations in oxygen and water fugacities on the point defect chemistry of quartz (abstract). *Journal of Structural Geology*, **3**, 335.

Dennis, P.F. (1984) Oxygen self-diffusion in quartz under hydrothermal conditions. *Journal of Geophysical Research*, **89**, 4047-4057.

De Santis R., Breedveld G.J.F. & Prausnitz J.M. (1974) Thermodynamic properties of aqueous gas mixtures at advanced pressures. *Industrial and Engineering Chemistry, Process Design and Development*, **13**, 374-377.

Deuchar J. (1822) Observations on the occasional appearance of water in the cavities of regular crystals; and on the porous nature of quartz, and other crystalline substances, as the probable cause of that occurance. *Philosophical Magazine, Series 1*, **60**, 310-314.

Dhamelincourt, P., Bény, J.M., Dubessy, J. & Poty, B. (1979) Analyse d'inclusion fluides à la microsonde MOLE à affet Raman. *Bulletin de Minéralogie*, **107**, 155-168.

Dodds W.S., Stutzman L.F. and Sollami B.J. (1956) Carbon dioxide solubility in water. *Industrial and Engineering Chemistry*, **1**, 92-95.

Dolomieu, D. (1792) l'Huile de Pétrole dans le Crystal de roche et les Fluides élastique tirés du Quartz, *Journal de Physique*, **40**, 318-319.

Doria, A., Boiron, M.C. & Noronha, F. (1991) Metamorphic fluids in quartz veins and their surroundings. An example of an Au-district of Northern Portugal (abstr.). *Plinius, ECROFI XI*, **5**, 60.

Doukhan, J.C. & Trepied, L. (1985) Plastic deformation of quartz single crystals. *Bulletin de Mineralogie*, **108**, 97-123.

Duan, Z., Møller, N. & Weare, J.H. (1992a) An equation of state for the CH_4 -CO_2-H_2O system: I. Pure systems from 0 to 1000°C and 0 to 8000 bar. *Geochimica et Cosmochimica Acta*, **56**, 2605-2617.

Duan, Z. Møller, N., Weare, J.H. (1992b) An equation of state for the CH_4 -CO_2-H_2O system: II. Mixtures from 50 to 1000°C and 0 to 1000 bar. *Geochimica et Cosmochimica Acta,* **56,** 2619-2631.

Dubessy, J. & Ramboz, C. (1986) The history of organic nitrogen from early diagenesis to amphibolite facies: mineralogical, chemical, mechanical and isotopic consequences.(extended abstr.) *V^{th} International Symposium on Water-Rock Interaction.* Reykjavik, Iceland, 1771-1774.

Dubessy, J., Poty, B. & Ramboz, C. (1989) Advances in C-O-H-N-S fluid geochemistry based on micro-Raman spectrometric analysis of fluid inclusions. *European Journal of Mineralogy,* **1,** 517-534.

Duchesne, J.C. (1970) Iron-Titanite Oxide Minerals in the Bjerkrem-Sogndal Massif, South-western Norway. *Journal of Petrology,* **13,** 57-81.

Duchesne, J.C., Maquil, R. & Demaiffe, D. (1985) The Rogaland anorthosites: facts and speculations. In: *The Deep Proterozoic Crust in the North Atlantic Provinces* (eds. A.C.Tobi and J.L.R.Touret); *NATO ASI Series* **C 158,** pp.449-476, Reidel.

Duit, W., Jansen, J.H.B., Van Breemen, A. & Bos, A. (1986) Ammonium micas in metamorphic rocks as exemplified by Dome de l'Agout (France). *American Journal of Science,* **286,** 702-732.

Edgar A.D. (1973) *Experimental petrology, basic principles and techniques.* pp.217, Oxford University Press.

Einstein A. (1907) Die Plancksche Theorie der Strahlung und die Theorie der spezifischen Warmen. *Annalen der Physik,* **22,** 180-190.

Erikson, G. (1975) Thermodynamic Studies of high Temperature Equilibria. *Chemica Scripta,* **8,** 100-103.

Eugster, H.P. & Skippen, G.B. (1967) Igneous and metamorphic reactions involving gas equilibria. In: *Researches in Geochemistry* (ed. P.H.Abelson) 2, pp 492-520.

Fei Y. and Saxena S.K. (1986) A thermochemical data base for phase equilibria in the system Fe-Mg-Si-O at high pressure and temperature. *Physics and Chemistry of Minerals,* **13,** 311-324.

Fei Y. and Saxena S.K. (1987) An equation for heat capacity of solids. *Geochimica et Cosmochima Acta,* **51,** 251-254.

174

Ferguson H.G. (1914) Lode deposits of the Alleghany district, California. *U.S. Geological Survey, Bulletin,* **580-I,** 161.

Ferry, J.M. (1979) A map of chemical potential differences within an outcrop. *American Mineralogist,* **64,** 966-985.

Ferry, J.M. & Burt, D.M. (1982) Characterization of metamorphic fluid composition through mineral equilibria. In: *Characterization of metamorphism through mineral equilibria* (ed. J.M.Ferry); *Reviews in Mineralogy* **10,** 207-262.

Fisher, J.R. (1976) The volumetric properties of H_2O - a graphical portrayal. *Journal of Research U.S. Geological Survey,* **4,** 189-193.

Fletcher R.C. and Hofmann A.W. (1974) Simple models of diffusion and combined diffusion-infiltration metasomatism. In: *Geochemical transport and kinetics* (eds. A.W.Hofmann, B.J.Giletti, H.S.jr.Yoder and R.A.Yund), pp. 243-259. Carnegie Inst.Washington Pub.**643,** Washington D.C.

Flowers G.C. (1979) Correction of Holloway's (1977) adaption of the modified Redlich-Kwong equation of state for calculation of the fugacities of molecular species in supercritical fluids of geological interest. *Contributions to Mineralogy and Petrology,* **69,** 315-318.

French B.M. (1966) Some geological implications of equilibrium between graphite and a C-H-O gas phase at high temperatures and pressures. *Reviews of Geophysics,* **4,** 223-253.

Frondel, C (1962) Silica minerals. In: *The system of mineralogy of James Dwight Dana and Edward Salisbury Dana, Yale University 1837-1892,* Vol.III, pp.334, New York, Wiley.

Frost, B.R. & Chacko, T. (1989) The granulite uncertainty principle: limitations on thermometry in granulites. *Journal of Geology,* **97,** 435-450.

Gerretsen J., Paterson M.S. & McLaren A.C. (1989) The uptake and solibility of water in quartz at elevated pressure and temperature. *Physics and Chemistry of Minerals,* **16,** 334-342.

Gibbs J.W. (1876) On the equilibrium of heterogeneous substances. *Transactions of the Connecticut Academy,* **3,** 108-248.

Gilette, B.J. & Yund, R.A. (1984) Oxygen diffusion in quartz. *Journal of Geophysical Research,* **89,** 4039-4046.

Goltrant, O., Cordier, P. & Doukhan, J.-P. (1991) Planar deformation features in shocked quartz: a transmission electron microscopy investigation. *Earth and Planetary Science Letters,* **106**, 103-115.

Gratier J.P. (1982) Approche experimental et naturalle de la deformation des roches par dissolution-cristallisation, avec transfert de matiere. *Bulletin de Mineralogie,* **105**, 291-300.

Gratier J.P. & Jenatton L. (1984) Deformation by solution-deposition, and re-equilibration of crystals depending on temperature, internal pressure and stress. *Journal of Structural Geology,* **6**, 189-200.

Greenwood, H.J. (1975) Buffering of pore fluids by metamorphic reactions. *American Journal of Science,* **275**, 573-593.

Griggs D.T. (1967) Hydrolitic weakening of quartz and other silicates. *Geophysical Journal of the Royal Astronomic Society,* **14**, 19-31.

Griggs, D.T. (1974) A Model of hydrolytic weakening in quartz. *Journal of Geophysical Research,* **79**, 1653-1661.

Griggs, D.T. & Blacic, J.D. (1965) Quartz: anomalous weakness in synthetic crystals. *Science,* **147**, 292-295.

Guilhaumou, N., Dhamelincourt, P., Touray, J-C. & Touret, J. (1981) Etude des inclusions fluides du systeme N_2-CO_2 de dolomites et de quartz de Tunesie septentrionale. Donnees de la microcryoscopie et de l'analyse a la microsonde a effet Raman. *Geochimica et Cosmochimica Acta,* **45**, 657-673.

Haas J.L.jr & Fisher J.R. (1976) Simultaneous evaluation and correlation of thermodynamic data. *American Journal of Science,* **276**, 525-545.

Haggarty, S.E. (1976) Opaque mineral oxides in terrestrial igneous rocks. In: *Oxide Minerals* (ed. D.Rumble III), *Reviews in Mineralogy* **3**, Hg101-Hg175.

Hagon, J.P., Stoneham, A.M. & Jaros, M. (1987) Transport processes in silicon oxidation II: Wet oxidation. *Philosophical Magazine,* **B55**, 225-235.

Halbach H. and Chatterjee N.D. (1982) An emperical Redlich-Kwong type equation of state for water to 1000°C and 200 Kbar. *Contributions to Mineralogy and Petrology,* **79**, 337-345.

Hall, D.L., Sterner, S.M. & Bodnar, R.J. (1989) Experimental evidence for hydrogen diffusion into fluid inclusions in quartz (abstr.) *Geological Society of America Abstracts with Programs.* **21**, A358.

Hallam, M. & Eugster, H.P. (1976) Ammonium silicate stability relations. *Contributions to Mineralogy and Petrology,* **57,** 227-224.

Hansen, E.C., Newton, R.C. & Janardhan, A.S. (1984) Fluid inclusions in rocks from the amphibolite-facies gneiss to charnokite progression in southern Karnataka, India: direct evidence concerning the fluids of granulite metamorphism. *Journal of Metamorphic Geology,* **2,** 249-264.

Heggie, M. (1992) A molecular water pump in quartz dislocations. *Nature,* **355,** 337-339.

Heggie, M. & Nylén, M. (1984) Dislocation core structures in *σ* quartz from a valence force potential. *Philosophical Magazine B,* **50,** 543-555.

Heggie, M. & Jones, R. (1987) Density functional analysis of the hydrolysis of Si-O bonds in disiloxane: Application to hydrolytic weakening in quartz. *Philosophical Magazine Letters,* **55,** 47-51.

Heilig M. & Franck E.U. (1989) Calculation of thermodynamic properties of binary fluid mixtures to high temperatures and high pressure. *Berichte der Bunsengesellschaft für Physikalische Chemie,* **93,** 898-905.

Heinisch H.L., Sines, Jr., G., Goodman, J.W. & Kirby, S.H. (1975) Elastic stresses and self-energies of dislocations of arbitrary orientation in anisotropic media: olivine, orthopyroxene, calcite, and quartz. *Journal of Geophysical Research,* **80,** 1885-1896.

Helgeson H.C., Delany J.M., Nesbitt H.W. & Bird D.K. (1978) Summary and critique of the thermodynamic properties of rock-forming minerals. *American Journal of Science,* **278,** 1-221.

Hermans, G.A.E.M., Tobi, A.C., Poorter, R.P.E. & Maijer, C. (1975) The high -grade metamorphic Precambrian of the Sirdal-Orsdal Area, Rogaland/Vest -Agder, South-west Norway. *Norges Geologiske Undersøkelse,* **318,** 51-74.

Hickman S.H. & Evans B. (1987) Influence of geometry upon crack healing rate in calcite. *Physics and Chemistry of Minerals,* **15,** 91-102.

Hirschfelder J.O., Curtis C.F. & Bird R.B. (1967) *Molecular Theory of Gases and Liquids.* pp.1249, New York, Wiley.

Hirth, J.P. & Lothe, J. (1968) *Theory of Dislocations.* pp.780, McGraw-Hill.

Hobbs B.E. (1968) Recrystallization of single crystals of quartz. *Tectonophysics,* **6,** 353-401.

Hobbs, B.E. (1984) The hydrolytic weakening effect in quartz. In: *Point Defects in Minerals*, (ed. R.N.Schock) *Geophysical Monograph*, **31**, 151 -170, Washington, DC: American Geophysical Union.

Holdaway, H.J. (1971) Stability of andalusite and the aluminum silicate phase diagram. *American Journal of Science*, **271**, 97-131.

Hollister, L.S. (1988) On the origin of CO_2-rich fluid inclusions in migmatites. *Journal of Metamorphic Geology*, **6**, 467-474.

Hollister, L.S.(1989) Enrichment of CO_2 in fluid inclusions in quartz by removal of H_2O during crystal plastic deformation (abstr.). *Geological Society of America Abstracts with Programs*, **21**, A357.

Hollister, L.S. (1990) Enrichment of CO_2 in fluid inclusions in quartz by removal of H_2O during crystal-plastic deformation. *Journal of Structural Geology*, **12**, 895-901.

Holloway, J.R. (1977) Fugacity and activity of molecular species in supercritical fluids. In *Thermodynamics in Geology* (ed. D.G.Fraser), pp.161 -182. Reidel.

Holloway, J.R. (1981) Compositions and volumes of supercritical fluids in the earth's crust. In: *Short course in F.I.: applications to petrology* (eds. L.S.Hollister & M.L.Crawford), 13-38.

Holloway, J.R. & Reese, R.L. (1974) The generation of N_2-CO_2-H_2O fluids for use in hydrothermal experimentation 1. Experimental method and equilibrium calculations in the C-O-H-N system. *American Mineralogist*, **59**, 587-597.

Holness, M.B., Fein, J. & Graham, C.M. (1992) The effect of pressure on solid-dihedral angles in the system H_2O-CO_2-NaCl-Quartz (abstr.). *Terra Abstracts, IVth International Symposium Experimental Mineralogy, Petrology and Geochemistry*, **4**, 21.

Honma, H. & Itihara, Y. (1981) Distribution of ammonium in minerals of metamorphic and granitic rocks. *Geochimica et Cosmochimica Acta*, **45**, 983-988.

Hosieni K.R., Howald R.A. and Scanlon M.W. (1985) Thermodynamics of the lambda transition and the equation of state of quartz. *American Mineralogist*, **70**, 782-793.

178

Huijsmans, J.P.P., Kabel, A.B.E.T. & Steenstra, S.E. (1981) On the structure of a high-grade metamorphic Precambrian terrain in Rogaland, south Norway. *Norsk Geologisk Tidsskrift,* **61,** 183-192.

Jacobs G.K. & Kerrick D.M. (1981) Methane : an equation of state with application to the ternary system H_2O-CO_2-CH_4. *Geochimica et Cosmochimica Acta,* **45,** 607-614.

JANAF Thermochemical Tables. Natl.Stand.Ref.Data Ser., Natl.Bur.Stand. (1971).

Jansen J.B.H. & Schuiling, R.D. (1976) Metamorphism on Naxos, Petrology and thermal gradients. *American Journal of Science,* **276,** 1225-1253.

Jansen J.B.H., Andriessen P.A.M., Maijer C. & Schuiling R.D. (1977) Changing conditions of Alpine regional metamorphism on Naxos, with special reference to the Al-silicate phase diagram. In: *Metamorphism on Naxos* (J.B.H.Jansen) PhD Thesis, chapt.7, 1-20, State University Utrecht.

Jansen J.B.H., Van der Kraats A.H., Van der Rijst H. & Schuiling R.D. (1978) Metamorphism of siliceous dolomites at Naxos, Greece. *Contributions to Mineralogy and Petrology,* **67,** 279-288.

Jansen, J.B.H., Blok, R.J.P., Bos, A. & Scheelings, M. (1985) Geothermometry and geobarometry in Rogaland and preliminary results from the Bamble Area, S.Norway. In: *The Deep Proterozoic Crust in the North Atlantic Provinces* (eds. A.C.Tobi and J.L.R.Touret); *NATO ASI Series,* **C 158,** pp.499-516. Reidel.

Jansen J.B.H., Van der Rijst H., Rye R.O., Andriesen P.A.M. & Rye D.M. (1989) High integrated fluid rock ratios during metamorphism at Naxos: evidence from carbon isotopes of calcite in schist and fluid inclusions. *Contributions to Mineralogy and Petrology,* **103,** 123-126.

Kamerlingh Onnes H. (1901) Expression of the equation of state of gases and liquids by means of series. *Communications from the Physical Laboratory at the University of Leiden,* no.71, pp.25.

Kats, A. (1962) Hydrogen in alpha quartz. *Philips Research Reports,* **17,** 133 -195, 201-279.

Keating, P.N. (1966) Effect of invariance requirements on the elastic strain energy of crystals with application to the diamond structure. *Physical Review,* **145,** 635.

Kekulawala, K.R.S.S., Paterson, M.S. & Boland, J.N. (1981) An experimental study on the role of water in quartz deformation. In: *Mechanical Behaviour of Crustal Rocks* (eds. N.L.Carter et al.) *Geophysical Monograph Series,* **24,** 49-60, AGU, Washington, D.C.

Kennedy G.C. (1950) "Pneumatolysis" and liquid inclusion method of geologic thermometry. *Economic Geology,* **45,** 533-547.

Kerkhof, A.M. van den (1988) The system CO_2-CH_4-N_2 in fluid inclusions. *PhD Thesis, Univ.Amsterdam,* pp 206, Free University Press, Amsterdam.

Kerkhof, A.M. van den, Touret, J.L.R., Maijer, C. & Jansen, J.B.H. (1991) Retrograde methane-dominated fluid inclusions from high-temperature granulites of Rogaland, southwestern Norway. *Geochimica et Cosmochimica Acta,* **55,** 2533-2544.

Kerrick, D.M. & Jacobs, G.K. (1981) A modified Redlich-Kwong equation for H_2O, CO_2, and H_2O-CO_2 mixtures at elevated pressures and temperatures. *American Journal of Science,* **281,** 735-767.

Kerrich R. (1976) Some effects of tectonic recrystallisation on fluid inclusions in vein quartz. *Contributions to Mineralogy and Petrology,* **59,** 195-202.

Kieffer S.W. (1979) Thermodynamics and lattice vibrations of minerals: 1. Mineral heat capacities and their relationships to simple lattice vibrational models. *Reviews of Geophysics and Space Physics,* **17,** 1-19.

Kirby, S.H. & Green, H.W. (1980) Dunite xenoliths from Hualalai volcano: evidence for mantle diapiric flow beneath the island Hawaii. *American Journal of Science,* **280,** 550-575.

Kreulen R.(1977) CO_2-rich fluids during regional metamorphism on Naxos, a study on fluid inclusions and stable isotopes. *PhD Thesis, Univ.Utrecht,* pp 85.

Kreulen, R. (1980) CO_2-rich fluids during regional metamorphism on Naxos (Greece): carbon isotopes and fluid inclusions. *American Journal of Science,* **280,** 745-771.

Kronenberg, A.K., Kirby, S.H., Aines, R.D. & Rossman, G.R. (1986) Solubility and diffusional uptake of hydrogen in quartz at high water pressures:implications for hydrolitic weakening. *Journal of Geophysical Research,* **91,** 12723-12744.

Lamb, W.M. & Valley, J.W. (1985) C-O-H fluid calculations and granulite genesis. In: *The Deep Proterozoic Crust in the North Atlantic Provinces* (eds. A.C.Tobi and J.L.R.Touret); *NATO ASI Series* **C 158**, pp.119-131. Reidel.

Larson, L.T., Miller, J.D., Nadeau, J.E. & Roedder, E. (1973) Two sources of error inlow temperature inclusion homogenization determination, and corrections on published temperatures for the East Tennessee and Laisvall deposits. *Economic Geology,* **68**, 113-116.

Lämmlein, G. (1929) Sekundäre Flüssigkeiteinschlüsse in Mineralien. *Zeitschrift für Krystallographie und Mineralogie,* **71**, 237-256.

Lee, B.I. & Kessler, M.G. (1975) A generalized thermodynamic correlation based on three-parameter corresponding states. *AIChE Journal,* **21**, 510-527.

Lemmlein, G.G. (1952) Migration of a liquid inclusion in a crystal toward a source of heat. *Akademija Nauk SSSR, Dokl.,* **85**, 325-328.

Lemmlein, G.G. (1956) Formation of fluid inclusions in minerals and their use in geological thermometry. *Geochemistry,* **7**, 630-642.

Lister G.S., Banga G. & Feenstra A. (1984) Metamorphic core complexes of Cordilleran type in the Cyclades, Aegean Sea, Greece. *Geology,* **12**, 221-225.

Maier C.G. & Kelley K.K. (1932) An equation for the representation of high temperature heat content data. *Journal of the American Chemical Society,* **54**, 3242-3246.

Maijer, C. & Padget P. (eds.) (1987) The geology of the southernmost Norway: An excursion guide.*Norges Geologiske Undersøkelse Special Publication,* **1**.

Martin III R.J. (1972) Time-dependent crack growth in quartz and its application to creep of rocks. *Journal of Geophysical Research,* **77**, 1406-1419.

McLaren, A.C. (1991) *Transmission electron microscopy of minerals and rocks.* Cambridge topics in mineral physics and chemistry, **2**, pp.387, Cambridge University Press.

McLaren, A.C. & Phakey, P.P (1965) A transmission electron microscope study of amethyst and citrine. *Australian Journal of Physics,* **18**, 135-141.

McLaren, A.C. & Phakey, P.P. (1966) Transmission electron microscope study of bubbles and dislocations in amethyst and citrine quartz. *Australian Journal of Physics,* **19,** 19-24.

McLaren, A.C. & Phakey, P.P. (1969) Diffraction contrast from Dauphiné twin boundaries in quartz. *Physica Status Solidi,* **31,** 723-737.

McLaren, A.C., Retchford, J.A., Griggs, D.T. & Christie, J.M. (1967) Transmision electron microscope study of Brazil twins and dislocations experimentally produced in natural quartz. *Physica Status Solidi,* **19,** 631 -644.

McLaren, A.C., Cook, R.F., Hyde, S.T. & Tobin, R.C. (1983) The mechanisms of the formation and growth of water bubbles and associated dislocation loops in synthetic quartz. *Physics and Chemistry of Minerals,* **9,** 79-94.

McLaren, A.C., Fitzgerald, J.D. & Gerretsen, J. (1989) Dislocation nucleation and multiplication in synthetic quartz: relevance to water weakening. *Physics and Chemistry of Minerals,* **14,** 281-292.

Mie G. (1903) Zur kinetischen Theorie der einatomigen Körper. *Annalen der Physik,* **11,** 657-697.

Nicol W. (1828) Observations on the fluid contained in crystallized minerals. *Edinburgh New Philosophical Journal,* **5,** 94-96.

Nicolas, A. & Poirier, J.P. (1976) *Crystalline plasticity and solid state flow in metamorphic rocks.* pp.444, Wiley Interscience, London.

Nicols F.A. & Mullins W.W. (1965) Morphological changes of a surface of revolution due to capillarity-induced surface diffusion. *Journal of Applied Physics,* **36,** 1826-1835.

Nordstrom D.K. & Munoz J.L. (1985) *Geochemical thermodynamics.* pp.477, The Benjamin/ Cummings Publishing Co.

Nuttall,R.H.D. & Weil, J.A. (1980) Two hydrogenic trapped-hole species in a -quartz. *Solid State Communications,* **33,** 99-102.

Oonk H.A.J. (1981) *Phase Theory, the thermodynamics of heterogeneous equilibria.* pp.269, Elsevier Scientific Publishing Company.

Papanikolaou D.J.(1986) Tectonic evolution of the Cycladic Blueschist Belt (Aegean sea, Greece). In: *Chemical transport in metasomatic processes* (ed. H.C.Helgeson), *NATO ASI Cyclades, Greece Series,* **C 218,** pp.429-450, Riedel, Dordrecht.

Parks, G.A. (1984) Surface and interfacial free energies of quartz. *Journal of Geophysical Research,* **89,** 3997-4008.

Pasteels, P., Demaiffe, D. & Michot, J. (1979) U-Pb and Rb-Sr geochronology of the eastern part of the south Rogaland igneous complex, S.Norway. *Lithos,* **12,** 199-208.

Paterson, M.S. (1986) The thermodynamics of water in quartz. *Physics and Chemistry of Minerals,* **13,** 245-255.

Paterson, M.S. & Kekulawala, K.R.S.S. (1979) The role of water in quartz deformation. *Bulletin de Mineralogie,* **102,** 92-98.

Pécher A. (1981) Experimental decrepitation and re-equilibration of fluid inclusions in synthetic quartz. *Tectonophysics,* **78,** 567-583.

Pécher, A. (1984) Chronologie et ré-équilibrage des inclusions fluides: quelques limites a lear utilisation en mivrothermométrie. In: *Thermométrie et barométrie géologiques,* (ed. M.Lagache), Soc.Francaise de Mineralogie et de Cristallographie, **2,** 463-485.

Pécher A. & Bouillier A. (1984) Evolution a pression et temperature elevees d'inclusion fluides dans un quartz synthetic. *Bulletin de Mineralogie,* **107,** 139-153.

Pitzer K.S. (1939) Corresponding states for perfect liquids. *Journal of Chemical Physics,* **7,** 583.

Poirier, J-P. (1985) *Creep of crystals.* pp.260, Cambridge University Press, United Kingdom.

Prausnitz J.M., Lichtenthaler R.N. and de Azevedo E.G. (1986) *Molecular thermodynamics of fluid-phase equilibria.* pp.600, Prentice Hall Inc.

Raoult, F.M. (1888) The general law of the vapor-pressure of solvents. *Comptes Rendus,* **104,** 1430.

Redlich O. & Kwong J.N.S. (1949) On the thermodynamics of solutions: V. an equation of state, fugacities of gaseous solutions. *Chemical Reviews,* **44,** 233-244.

Rice, J.M. & Ferry, J.M. (1982) Buffering, infiltration, and the control of intensive variables during metamorphism. In *Characterization of metamorphism through mineral equilibria* (ed. J.M.Ferry); *Reviews in Mineralogy,* **10,** pp 207-262.

Rye, R.O., Schuiling, R.D., Rye,D.M. & Jansen, J.B.H. (1976) Carbon, hydrogen, and oxygen isotope studies of the regional metamorphic complex at Naxos, Greece. *Geochimica et Cosmochimica Acta,* **40,** 1031-1049.

Robie, R.A., Hemingway, B.S. & Fisher, J.R. (1978) Thermodynamical properties of minerals and related substances at 298.15 K and 1 bar (10^5Pascals) pressure and at higher temperatures. *United States Geological Survey Bulletin,* **1452,** 1-455.

Roedder E. (1984) Fluid inclusions. Mineralogical Society of America, Reviews in Mineralogy, **12,** 644 p.

Roedder E. & Skinner B.J. (1968) Experimental evidence that fluid inclusions do not leak. *Economical Geology,* **63,** 715-730.

Samson, I.M. & Williams-Jones, A.E. (1981) C-O-H-N-salt fluids associated with contact metamorphism, McGerrigle Mountains, Quebec: A Raman spectroscopic study. *Geochimica et Cosmochimica Acta,* **55,** 169-177.

Sauter, P.C.C. (1983) Metamorphism of siliceous dolomites in the high grade Precambrium of Rogaland, SW Norway. Ph.D. Thesis, *Geologica Ultaiectina,* **32,** 1-143.

Saxena, S.K. (1989a) Oxidation state of the mantle. *Geochimica et Cosmochimica Acta,* **53,** 89-95.

Saxena S.K. (1989b) Assessment of bulk modulus, thermal expansion and heat capacity of minerals. *Geochimica et Cosmochimica Acta,* **53,** 785-789.

Saxena, S.K. & Erikson, G. (1983) Theoretical Computation of Mineral Assemblages in Pyrolite and Lherzolite. *Journal of Petrology,* **24,** 538-555.

Saxena, S.K. & Fei, Y. (1987a) Fluids at crustal pressure and temperatures. *Contributions to Mineralogy and Petrology,* **95,** 370-375.

Saxena, S.K. & Fei, Y. (1987b) High pressure and high temperature fluid fugacities. *Geochimica et Cosmochimica Acta,* **51,** 783-791.

Shelton K.L. & Orville P.M. (1980) Formation of synthetic fluid inclusions in natural quartz. *American Mineralogist,* **65,** 1233-1236.

Skippen, G.B. & Marshall D.D. (1991) The metamorphism of granulites and devolatilization of the lithosphere. *Canadian Mineralogist,* **29,** 693-705.

Smith F.G. (1953) Historical development of inclusion thermometry. *University of Toronto Press,* Toronto, Canada, pp.149.

Smith D.L. & Evans B. (1984) Diffusional crack healing in quartz. *Journal of Geophysical Research,* **89,** B6, 4125-4135.

Sorby H.C. (1858) On the microscopic structure of crystals, indicating the origin of minerals and rocks. *Journal Geological Society of London,* **14,** part 1, 453-500.

Spear, F.S., Ferry, J.M. & Rumble III, D. (1982) Analytical formulation of phase equilibria : the Gibbs' method. In *Characterization of metamorphism through mineral equilibria* (ed. J.M.Ferry); *Reviews in Mineralogy,* **10,** pp. 207-262.

Spencer, K.J. & Lindsey, D.H. (1981) A solution model for coexisting iron -titanium oxides. *American Mineralogist,* **66,** 1189-1201.

Spiers, C.J., Schutjens, P.M.T.M., Brzesowsky, R.H., Peach, C.J., Liezenberg, J.L. & Zwart, H.J. (1990) Experimental determination of constitutive parameters governing creep of rock salt by pressure solution. In: *Deformation mechanisms, rheology and tectonics* (eds. R.J.Knipe & E.H.Rutter) *Geological Society Special Publications,* **54,** 215-227.

Spycher N.F. and Reed M.H. (1988) Fugacity coefficient of H_2, CO_2, CH_4, H_2O and of H_2O-CO_2-CH_4 mixtures: a virial equation treatment for moderate pressure and temperatures applicable to calculations of hydrothermal boiling. *Geochimica et Cosmochimica Acta,* **52,** 739-749.

Stephenson T.E. (1952) Sources of error in the decrepitation method of study of liquid inclusions. *Economic Geology,* **47,** 743-750.

Sterner, S.M. & Bodnar, R.J. (1984) Synthetic fluid inclusions in natural quartz 1: Compositional types synthesized and applications to experimental geochemistry. *Geochimica et Cosmochimica Acta,* **48,** 2659-2668.

Sterner, S.M. & Bodnar, R.J. (1989) Synthetic fluid inclusions -VII: Re -equilibration of fluid inclusions in quartz during laboratory-simulated metamorphic burial and uplift. *Journal of Metamorphic Geology,* **7,** 243 -260.

Sterner, S.M. & Bodnar, R.J. (1991) Synthetic fluid inclusions X: Determination of P-V-T-X properties in the CO_2-H_2O system to 6 kbar and 700°C. *American Journal of Science,* **291,** 1-54.

Stevenson, F.J. (1962) Chemical state of the nitrogen in rocks. *Geochimica et Cosmochimica Acta,* **26,** 797-809.

Swanenberg H.E.C. (1980) Fluid inclusions in high-grade metamorphic rocks from S.W.Norway. Ph.D.Thesis, *Geologica Ultraiectina,* **25,** 1-147.

Takenouchi S. & Kennedy G.C. (1964) The binary system H_2O-CO_2 at high temperatures and pressures. *American Journal of Science,* **262,** 1055 -1074.

Thompson, A.B. (1975) Mineral reactions in a calc-mica schist from Gassetts, Vermont, USA. *Contributions to Mineralogy and Petrology,* **53,** 105-127.

Thompson, J.B. & Thompson, A.B. (1976) A model system for mineral assemblages in pelitic schists. *Contributions to Mineralogy and Petrology,* **58,** 243-277.

Tobi, A.C., Hermans, G.A.E.M., Maijer, C. & Jansen, J.B.H. (1985) Metamorphic zoning in the high-grade proterozoic of Rogaland-Vest Adger, SW Norway. In: *The Deep Proterozoic Crust in the North Atlantic Provinces* (eds. A.C.Tobi and J.L.R.Touret); *NATO ASI Series* **C 158,** pp.477-497. Reidel.

Tödheide, K. & Franck, E.U. (1963) Das Zweiphasengebiet und die kritische Kurve im System Kohlendioxid-Wasser bis zu Drucken von 3500 bar. *Zeitschrift für Physikalische Chemie Neue Folge,* **37,** 387-401.

Touret, J. (1982) An empirical phase diagram for a part of the N_2-CO_2 system at low temperatures. *Chemical Geology,* **37,** 49-58.

Touret J.R.L. & Bottinga Y. (1979) equation d'etat pour le CO_2; application aux inclusion carboniques. *Bulletin de Mineralogie,* **102,** 577-583.

Ulmer, G.C., Grandstaff, D.E., Weiss, D., Moats, M.A., Buntin, T.J., Gold, D.P., Hatton, C.S., Kadik, A., Koseluk, R.A. & Rosenhauer, M. (1987) The mantle redox state: An unfinished story? *Geological Society of America Special Paper,* **215,** 5-23.

Urai, J.L., Schuiling, R.D. & Jansen J.B.H. (1990) Alpine deformation on Naxos (Greece). In: *Deformation Mechanisms, Rheology and Tectonics,* (eds. R.J.Knipe & E.H.Rutter), *Geological Society Special Publication,* **54,** 509-522.

Ursell H.D. (1927) The evaluation of Gibbs' phase-integral for imperfect gases. *Proceedings of the Cambridge Philosophical Society,* **23,** 685-697.

Valley, J.W., Bohlen, S.R., Essene, E.J. & Lamb, W. (1990) Metamorphism in Adirondacks: II. The role of fluids. *Journal of Petrology,* **31,** 555-596.

Van Hise C.R. (1890) Pre-Cambrian of the Black Hills. *Geological Society of America,* **1,** 216-218.

Voncken, J.H.L., Konings, R.J.M., Jansen, J.B.H. & Woensdrecht, C.F. (1988) Hydrothermally grown buddingtonite, an anhydrous ammonium feldspar ($NH_4AlSi_3O_8$). *Physics and Chemistry of Minerals,* **15,** 323-328.

Waals J.D. van der (1873) Over de continuiteit van den gas- en vloeistoftoestand. PhD-thesis, Leiden, Sijthof, pp.184.

Waldram J.R. (1991) *The theory of thermodynamics.* pp.336, Cambridge University Press.

Wanamakers, B.J. & Evans, B. (1985) Experimental diffusional crack healing in olivine. In: *Point defects in minerals,* (ed. R.Schock), *Geophysical Monograph,* **31,** American Geophysical Union, Washington DC, 194-210.

Wanamakers, B.J. & Evans, B. (1989) Mechanical re-equilibration of fluid inclusions in San Carlos olivine by power-law creep. *Contributions to Mineralogy and Petrology,* **102,** 102-111.

Ward J.C. (1875) On the granitic, granitoid, and associated metamorphic rocks of the Lake-District. Part 1, Ibid., 568-598.

Watson E.B. & Brenan J.M. (1987) Fluids in the lithosphere, 1.Experimentally determined wetting characteristics of CO_2-H_2O fluids and their application for fluid transport, host-rock physical properties, and fluid inclusion formation. *Earth Planetary Science Letters,* **85,** 497-515.

Weast R.C. (ed.) (1975) *Handbook of Chemistry and Physics.* Table: Physical constants of inorganic components, B 84, CRC Press.

Wielens, J.B.W., Andriessen, P.A.M., Boelrijk, N.A.I.M., Hebeda, E.H., Priem, H.N.A., Verdurmen, E.A. & Verschure, R.H. (1981) Isotope geochronology in the high-grade metamorphic Precambrium of southwestern Norway: New data and reinterpretations. *Norges Geologiske Undersøkelse,* **359,** 1-30.

Wilkins, R.W.T., Hladky, G., Gratier, J.P. & Jenatton, L. (1992) Some relationships between cracks and fluid inclusions (abstr.). *Pacrofi IV,* 89.

Wilkins, R.W.T. & Barkas J.P. (1979) Fluid inclusions, deformation and recrystallization in granite tectonites. *Contributions to Mineralogy and Petrology,* **65,** 293-299.

Wilmart, E., Clocchiatti, R., Duchesne, J.C. & Touret, J.L.R. (1991) Fluid inclusions in charnockites from the Bjerkreim-Sokndal massif (Rogaland, southwestern Norway): fluid origin and in situ evolution. *Contributions to Mineralogy and Petrology,* **108,** 453-462.

Wintsch, R.P. & Dunning, J. (1985) The effect of dislocation density on the aqueous solubility of quartz and some geological implications: a theoretical approach. *Journal of Geophysical Research,* **90,** 3649-3657.

Wolff E. (1845) Chemisch-Mineralogische Notizen 3 : über den Glühverlust des Quarzes und des Feldspaths. *Journal für praktische Chemie,* **34,** 237 p.

Yardley B.W.D. & Bottrell S.M. (1988) Immiscible fluids in metamorphism: implications of two phase flow for reaction history. *Geology,* **16,** 199-202.

Yund, R.A., Smith, B.M. & Tullis, J. (1981) Dislocation-assisted diffusion of oxygen in albite. *Physics and Chemistry of Minerals,* **7,** 185-189.

Zirkel F. (1873) *Die microskopische Beschaffenheit der Mineralien und Gesteine.* pp.39-85, and 149-150, Engelman, Leipzig.

CURRICULUM VITAE

Ronald J. Bakker werd geboren op 1 december 1962 te Groningen. In juni 1981 behaalde hij het diploma Atheneum-B aan de Lorentz Scholengemeenschap te Arnhem. In september van dat jaar begon hij met de studie Geologie aan de Rijksuniversiteit te Utrecht. In april 1984 werd het kandidaats examen G3 afgelegd. In januari 1988 werd het doctoraal examen met als hoofdvak Structurele Geologie en groot bijvak Petrologie afgelegd. In de periode van februari 1988 tot febuari 1992 was hij in dienst van de Nederlandse Organisatie voor Wetenschappelijk Onderzoek en werkzaam bij de vakgroep Geochemie als onderzoeker in opleiding. Van februari 1992 tot heden werd dit proefschrift afgerond vanuit een uitkeringsgerechtigde positie.